Fast Switchable Ultrastrong Coupling Between Superconducting Artificial Atoms and Electromagnetic Fields

by

Jiahao Shi

A thesis
presented to the University of Waterloo
in fulfillment of the
thesis requirement for the degree of
Master of Science
in
Physics

Waterloo, Ontario, Canada, 2019

I hereby declare that I am the sole author of this thesis. This is a true copy of the thesis, including any required final revisions, as accepted by my examiners.

I understand that my thesis may be made electronically available to the public.

Abstract

This thesis consists of two parts: the main part is a theoretical investigation of the ultrastrong coupling regime for atom-light coupling in superconducting circuits, and the second part is concerned with the development of a new high coherence flux qubit design.

The spin-boson model describes the interaction between a quantum two-level system and a continuum of bosonic modes. When the interaction strength becomes comparable to the system frequency, the system enters the ultrastrong coupling (USC) regime, where the rotating wave approximation breaks and the system dynamics need to be described nonperturbatively. Recently, the ultrastrong coupling has been achieved on a device consisting of a superconducting flux qubit coupled to an electromagnetic continuum, with the coupling strength being verified in experiments by the standard transmission method [1]. The first project in this thesis aims to measure the dynamics of the spin-boson model in a direct and controllable way when the coupling strength is in the USC regime. We propose three experiments to measure the coherence of the two-level system including the relaxation and dephasing, and the the renormalized tunneling frequencies in the ultrastrong coupling regime. The controllable measurements are realized with a fast-switchable ultrastrong coupling system consisting of a two-loop flux qubit galvanically coupled to an open transmission line, flux bias and driving lines, and readout circuits. The design and model of the full device are presented. We demonstrate that the three proposed experiments can be well implemented based on the simulations of qubit properties and coupling strengths.

The second part of the thesis presents work on the design of a new type of capacitively shunted flux qubit. This work is motivated by improving qubit coherence time and anharmonicity, which is essential for speeding up qubit gates and enhancing the capability of quantum computing. It was demonstrated that adding shunting pads to flux qubits can drastically improve the coherence time and the reliability of qubit fabrication, but the CSFQ was shown with moderate anharmonicities [2]. In this project, we present the a new design of CSFQ and its circuit model, which contains three Josephson junctions and three shunting pads. In experiments, the qubit spectroscopy matches well with the circuit model, which takes into account all the capacitances between the qubit and other circuits. The qubit is found to have both large anharmonicity $\mathcal{A} = \omega_{12} - \omega_{01} = 2\pi \times 3.69$ GHz, and high coherence with $T_1 = 40 \pm 5$ μs. We also present experiments on the multilevel quantum control and multilevel relaxation measurement. We perform qutrit state tomography to reconstruct the full density matrix with the tomography fidelity reaching 99.2%. We are able to extract the time-dependent state populations for the relaxation process of a qutrit, and extract the exact transition rates between the three levels.

Acknowledgements

First and foremost, I would like to thank my supervisor Adrian Lupascu for his guidance through out my entire graduate studies. His enthusiasm and devotion to the research have been encouraging me. I am grateful for his patient assistance, all the inspiring discussions and sincere advice on my career.

Then, I would like to thank all the SQD group members for their support. I am very grateful to Muhammet Ali Yurtalan for all his help in fabrication and experiments. I want to thank Ali, Xi Dai, Salil Bedkihal and Michal Kononenko for their comments on this thesis.

I am thankful to the Quantum NanoFab team for their assistance in nanofabrication.

I am grateful to all my friends who have been supporting me for the three years in Waterloo. I want to thank my parents and my grandma for their generous support through all the years.

Dedication

This is dedicated to the ones I love.

Table of Contents

List of Tables

List of Figures

Chapter 1

Introduction

Light-matter interaction is broadly relevant for our understanding of our physical worlds and plays an important role in phenomena including plants converting sunlight into energy through photosynthesis, bulbs emitting light and solar cells absorbing light to generate electricity. Fundamentally, it is important to understand the quantum processes of light-matter interaction for basic systems. In this context, the spin boson model, consisting of a two-level system coupled to a collection of bosonic modes, describes the main features of the interaction of atoms/molecules with the electromagnetic field. Early research in this area focused on simplified systems where neutral atoms were treated as qubits and they were put inside electromagnetic cavities, such that atoms were coupled to only one or a few light modes. This field of research is called the cavity electrodynamics (QED). By applying the rotating-wave approximation (RWA), systems are described by the Janynes-Cummings Hamiltonian [3], which can be exactly solved. In these systems, coupling strengths between atoms and light can reach the strong coupling regime [4, 5], where interaction strengths are stronger than the qubit and photon losses, which enables exchanges of energy quanta between qubits and light. This phenomenon is called vacuum Rabi oscillation [6].

Circuit QED is a new area of research concerned with the study of the interaction of artificial atoms, such as superconducting qubits. Compared to individual atoms, superconducting qubits can be fully controlled, and the coupling strengths in these systems are much stronger than the coupling between atoms and light. In superconducting circuits, strong coupling between qubits and coplanar waveguide resonators were observed [7, 8]. These strong coupling systems are widely used for quantum state readout [9]. Efforts were made to keep increasing the coupling strength, and the so-called ultrastrong coupling (USC) regime was first reached in [10]. The USC regime is defined as the coupling strength reaches 10% or more of the bare qubit frequency. With such strong coupling strengths, the

RWA breaks and incoherent interactions due to the counter rotating terms are observed [8, 10, 11].

When considering qubits coupled to continuum of bosonic modes, the interaction becomes complicated. In these systems, qubit relaxation depends on not only the coupling to a single light mode, but also the spectral density of the continuum [12]. Strong coupling of a superconducting qubit to a one-dimentional (1D) open transmission line was first observed almost a decade ago [13]. Recently, the ultrastrong coupling was first realized on a system consisting of a superconducting flux qubit coupled to a 1D open transmission line [1].

1.1 Ultrastrong coupling in superconducting circuits

In the ultrastrong coupling regime, understanding the dynamics of the spin-boson model [12] requires sophisticated theoretical techniques, including the quasi-adiabadic propagator path integral [14], the matrix product states [15] and the dynamical polaron ansatz [16], which give predictions on qubit relaxation rates. The transition frequencies of superconducting qubits are approximately in the range of 1 to 20 GHz, so the qubit relaxation time is extremely short and only in the order of several nanoseconds or smaller, which makes the relaxation measurement difficult to realize. Although the USC regime has already been achieved, but it was only verified by the standard transmission measurement [1], where the authors fit the transmission spectrum with an approximate model to extract the relevant rates. The motivation of this project is to directly measure the qubit relaxation in the time domain to find the relaxation rates, when the coupling strength is in the USC regime. To achieve this, we develop a superconducting system consisting of a flux qubit with fast switchable coupling to electromagnetic continuum. Apart from the relaxation, we also aim to measure the qubit dephasing in the USC regime. In spin-boson model, the qubit frequencies are expected to be renormalized due to large correlations between qubits and baths. The qubit transition frequencies are predicted to decrease with stronger coupling strengths. This phenomenon hasn't been directly observed in experiments when the coupling strength reaches the USC regime. With our controllable system, we aim to measure the renormalized qubit frequencies in the USC regime.

Apart from the experiments on the spin-boson model, another motivation comes from the potential application of the fast switchable USC system in the field of relativistic quantum information. Ref. [17] proposes an experiment to study the dynamics of entanglement between two qubits. This work predicts the existent of a light core that divide the space time into two regions, with the entanglement due to correlated fluctuations of vacuum

in the spacelike region and the entanglement due to exchange of photons in the timelike region. The position of light core is determined by the traveling speed of photons. The proposed experiment is based on a system consisting of two qubit coupled to an open transmission line, and it requires full or partial tomography of qubit states without affecting the qubit-transmission line dynamics to measure the entanglement, which can be realized with the circuits presented in this thesis by fast switching off the coupling and then performing measurements on qubits. They show that the entanglement increases with the coupling strength, so our USC system is perfect for the experiment.

1.2 Design of superconducting qubits

Qubits are building blocks to quantum computers, just like what bits are to classical computers. Therefore, improving the quality of individual qubits is the very first step towards building a large-scale quantum computer. A key factor that limits qubit performance is its coherence time: if a qubit is left to interact with the environment, eventually its state gets mixed with the environment and is said to decohere, and the information stored inside is lost. Thus, a longer coherence time implies that more computation steps can be performed on a qubit before decoherence occurs, which is crucial for future applications which requires running long computations with many steps.

Flux qubits are sensitive to the flux noise and insensitive to the charge noise, because they are designed with large ratio of the Josephson energy to the charging energy E_J/E_c, such that the fluctuation of charging energy that is induced by the charge noise can only have small influence on the qubit Hamiltonian. The coherence of flux qubits had not been improved greatly over the years and the relaxation time T_1 was in the range of 6 to 20 μs [18, 19], while the T_1 of transmons can reach about 100 μs. In 2016, a special design of flux qubits, called the capacitively shunted flux qubits (CSFQ), was systematically researched [2], and it was found that the T_1 of CSFQ was largely improved and exceeded 40 μs. In [2], the α junction of the flux qubit is shunted with two large capacitive pads, which redistributes the electric field from the junction area, where there is a dielectric layer, to the large shunting pads, so the dielectric loss is reduced and the ratio of E_J/E_c is further increased. Thus, the CSFQ is even more insensitive to the charge noise, and the coherence is improved. Besides, using large shunting pads to dominate the junction capacitance make the qubit more reproducible. However, as a consequence of adding large shunting pads, the anharmonicity, which is defined as the frequency difference between 1-2 and 0-1 transitions, is reduced from several GHz for a typical flux qubit to only about 0.8 GHz. Similar moderate anharmonicity has also been observed for transmons, which are a type

of charge qubits with large capacitive shunting pads, but large anharmonicity is beneficial for performing more accurate selective qubit control and obtain faster qubit gates.

1.3 Outline of thesis

There are two projects presented in this thesis. Chapter 2 to 4 describes the main project on fast switchable ultrastrong coupling between superconducting flux qubits and electromagnetic continuum.

In Chapter 2, basic superconducting circuit elements are introduced. The circuit models and quantization processes of Josephson junctions as key components of superconducting qubits, and two types of flux qubits—the RF-SQUIDs and persistent current qubits are presented. Next, open transmission lines which are modeled as continuum baths, are introduced.

Chapter 3 introduces theories and circuit models on the strong coupling between qubits and electromagnetic continuum. First, the spin-boson model, including the Hamiltonian, decoherence model and adiabatic renormalization of qubits are introduced. Then, we introduce a system consisting of a superconducting flux qubit coupled to an open transmission line, whose coupling strength can reach the USC regime. We apply the decoherence model of the spin-boson model to this circuit, and then estimate the qubit decoherence rates.

In Chapter 4, the main results of this work are presented. First, we propose three experiments on measuring the qubit relaxation, dephasing and adiabatic renormalization in controllable ways. The detailed experiment steps and pulse sequences are given. Then, we present the circuit design and model of our device. We demonstrate the proposed experiments can be implemented on the device based on the simulations of qubit frequencies and coupling strengths. At last, we present the design and model of qubit control and readout circuits.

In Chapter 5, the second project on capacitively shunted flux qubit is presented. We first introduce the circuit design and model of the flux qubit with three shunting pads. Then, the fabrication steps of the device is introduced. Afterwards, we present the experiment results on qubit spectroscopy and qubit coherence. Finally, we discuss the experiments and analysis on multilevel systems, including qutrit tomography and multilevel relaxation.

Chapter 2

Introduction to superconducting circuits

In this chapter, several basic elements of the superconducting circuits are introduced. In Section 2.1, we discuss the Josephson junction, which is a key component of superconducting qubits. In Section 2.2, we present two types of superconducting flux qubits—the radio-frequency superconducting quantum interference device (RF-SQUID) and the persistent current qubit (PCQ). The quantization process and their quantum properties are presented. In Section 2.3, we analyze the open transmission line semi-classically and then treat it quantum mechanically.

2.1 Josephson junction

In superconductors, electrons form Cooper pairs and travel without any dissipation of energy, so superconductors do not have resistance. In 1962, Brian David Josephson predicted that Cooper pairs could tunnel through a junction, which consisting of two superconductors coupled by a weak link, in a dissipationless way [20]. The weak link can be an insulating layer, a piece of normal metal or the same superconductor with smaller sizes. This phenomenon was first proved by Philip Warren Anderson and J. M. Rowell [21]. Such junctions were therefore named after Brian David Josephson, namely Josephson junctions.

Figure 2.1 shows the structure of a type of Josephson junction and its circuit model. Cooper pairs in the superconductor can be described by a macroscopic wave function $\psi = |\psi|e^{i\varphi}$ according to the BCS theory [22], with φ the superconducting phase and

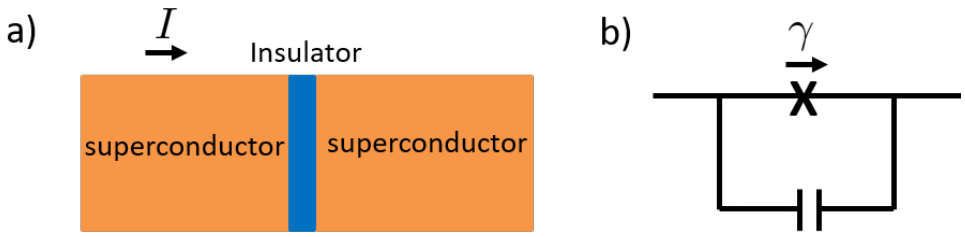

Figure 2.1: a) Diagram of the structure of a Josephson junction, consisting of two superconductors and an insulator in between. I is the current flowing through the junction. b) Circuit model of a Josephson junction. The junction is represented by the cross and the capacitance of the junction is represented by the shunting capacitor. γ is the phase across the junction.

$|\psi|$ is related to the population of electrons that form cooper pairs. In the Josephson junction, the phase difference between two superconductors contributes to the junction phase $\gamma = \varphi_1 - \varphi_2$. Part of the electrons in the superconductor form cooper pairs and tunnel through the junction, form the tunneling current I_J. Another part of the electrons accumulate at the capacitor due to the voltage drop across the junction, and the number of the accumulated electrons varies with the voltage, which forms the current in the branch of capacitor I_{cap}. The tunneling current I_J is related to the junction phase by the first Josephson relation

$$I_J = I_c \sin\gamma. \tag{2.1}$$

I_c is the critical current, which is defined as the maximum current allowed flowing through the junction without breaking the superconductivity. The voltage across the junction is explained by the second Josephson relation as

$$V = \frac{\Phi_0}{2\pi}\frac{d\gamma}{dt}, \tag{2.2}$$

where $\Phi_0 = \frac{h}{2e}$ is the flux quantum. The capacitor current is related to the voltage by

$$I_{\text{cap}} = C\dot{V} = \varphi_0 C\ddot{\gamma}. \tag{2.3}$$

It is found that the Josephson junction can be treated like a non-linear inductor with the Josephson inductance

$$L_J = \frac{V}{\dot{I}} = \frac{\Phi_0}{2\pi I_c \cos\gamma}, \tag{2.4}$$

where Eq 2.1 and 2.2 are used.

Next, we are going to show the quantization process of a Josephson junction. The electric energy of the junction is stored in the capacitor as

$$T = \frac{1}{2} C \varphi_0^2 \dot{\gamma}^2, \tag{2.5}$$

where C is the shunting capacitance and $\varphi_0 = \frac{\Phi_0}{2\pi}$ is the reduced flux quantum. The potential energy is written as

$$U = -\varphi_0 I_c \cos\gamma, \tag{2.6}$$

so the Lagrangian of the system is

$$\mathcal{L} = T - U = \frac{1}{2} C \varphi_0^2 \dot{\gamma}^2 + \varphi_0 I_c \cos\gamma. \tag{2.7}$$

The Euler Lagrange equation $\frac{d}{dt}\frac{\partial \mathcal{L}}{\partial \dot{\gamma}} = \frac{\partial \mathcal{L}}{\partial \gamma}$ is confirmed to hold, which justifies the Lagrangian. The conjugate momentum of γ is

$$p = \frac{\partial \mathcal{L}}{\partial \dot{\gamma}} = C \varphi_0^2 \dot{\gamma}. \tag{2.8}$$

Then, following the Legendre transformation $H = \dot{\gamma} p - \mathcal{L}$, the Hamiltonian is found as

$$H = \frac{p^2}{2C\varphi_0^2} - \varphi_0 I_c \cos\gamma. \tag{2.9}$$

To describe the system quantum mechanically, we need to replace the classical conjugate variables p and γ with quantum operators $\hat{p}$ and $\hat{\gamma}$. The commutation relation between these two operators is

$$[\hat{\gamma}, \hat{p}] = i\hbar. \tag{2.10}$$

The Hamiltonian becomes

$$\hat{H} = \frac{E_c}{h^2} \hat{p}^2 - E_J \cos\hat{\gamma}, \tag{2.11}$$

where $E_c = \frac{(2e)^2}{2c}$ and $E_J = \varphi_0 I_c$ are known as the charging energy and Josephson energy. We can find that the Hamiltonian of the Josephson junction is in a similar form to that of a quantum harmonic oscillator, which is

$$\hat{H} = \frac{\hat{p}^2}{2m} + \frac{1}{2} k \hat{x}^2. \tag{2.12}$$

However, the potential energy of the Josephson junction is in a cosine form instead of a parabola, because it is contributed by the non-linear Josephson inductance. As a result, unlike the quantum harmonic oscillator, the energy levels of the Josephson junction are anharmonic, which means the differences between adjacent energy levels are not the same. This makes the Josephson junction a key element in superconducting quantum devices.

2.2 Superconducting flux qubit

Superconducting qubits are based on Josephson junctions. Typical superconducting qubits includes phase qubits [23], charge qubits [24], flux qubits [25] and transmons [26]. They have distinct circuit structures and origins, and they work in different regimes, which are distinguished by the ratio E_J/E_C. The ratio is a factor affecting the qubit decoherence since it determines the qubit sensitivity to the fluctuations of charges or fluxes. In this thesis, we focus on the flux qubit since it is used in the main project discussed in Chapter 4. The flux qubit is featured with a loop, thus the magnetic flux in the loop is critical for the qubit. In this section, we will discuss about two types of flux qubits, the RF-SQUID and the persistent current qubit, in detail.

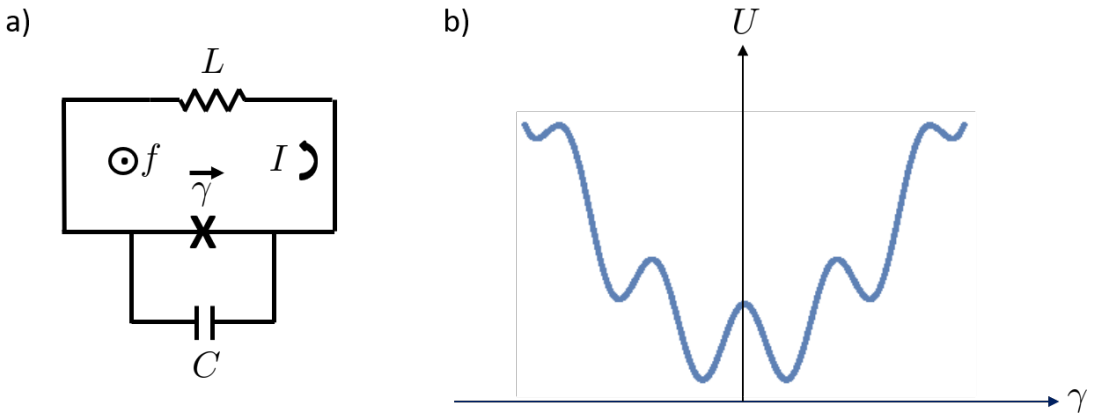

Figure 2.2: a) The circuit model of a RF-SQUID. L is the self inductance of the loop, I is the circulating current, C is the junction capacitance and $f = \Phi/\Phi_0$ is the external flux in unit of Φ_0; b) Diagram of the potential energy versus the junction phase of a RF-SQUID.

2.2.1 RF-SQUID

The flux qubit has a simple structure, consisting of a superconducting loop interrupted by one or more Josephson junctions. One initial flux qubit is called the RF-SQUID, which only contains one junction, but have a large-size superconducting loop. The circuit model of a RF-SQUID is shown in Fig 2.2a. The phase relation in the circuit is

$$\gamma + \frac{LI}{\varphi_0} = -2\pi f, \tag{2.13}$$

where $L = L_g + L_k$, with L_g the self-inductance of the loop and L_k the kinetic inductance resulted by the energy of motion of cooper pairs, and the I is the circulating current given by

$$I = I_c \sin\gamma + \varphi_0 C\ddot{\gamma} \tag{2.14}$$

The electric and potential energies of the circuit are

$$\begin{aligned} T &= \frac{1}{2}\varphi_0^2 C\dot{\gamma}^2 \\ U &= -\varphi_0 I_c \cos\gamma + \frac{\varphi_0^2}{2L}(\gamma + 2\pi f)^2 . \end{aligned} \tag{2.15}$$

Following the same quantization procedure for the Josephson junction, the Hamiltonian of the RF-SQUID is found as

$$H = \frac{p^2}{2\varphi_0^2 C} - \varphi_0 I_c \cos\gamma + \frac{\varphi_0^2}{2L}(\gamma + 2\pi f)^2 , \tag{2.16}$$

where p is the conjugate momentum of the junction phase γ. The potential energy is composed of a cosine like Josephson term and a parabola like inductive term, so the shape of the potential diagram depends on the screening factor $\beta = LI_c/\varphi_0$. When β is large, the Josephson term contributes substantially, and there are many local minimums in the potential. When the imposed flux in the SQUID equals to a half plus an integer $f = \frac{1}{2} + n$, there exist two potential minimums, which form a double well potential, as shown in Fig 2.2b. Due to the tunneling between the wells, the eigenstates of the Hamiltonian are superpositions of the degenerate states in two wells. The energy levels of the eigenstates are anharmonic, so the transitions between various energy levels can be controlled by the frequency selection. Through a two-level approximation, the RF-SQUID is considered as a qubit constituted by the two lowest eigenstates.

Since the screening factor $\beta = LI_c/\varphi_0$ need be large to have deep potential minima, the superconducting loop should have a very large size, such that the self inductance L is big enough. However, the large-size loop makes the qubit very sensitive to flux fluctuations and make qubit coherence worse. The persistent current qubit, which is going to be introduced in the next subsection, was proposed to solve this problem [25].

2.2.2 Persistent current qubit

A persistent current qubit contains at least three Josephson junctions. Fig 2.3 shows the circuit model of a qubit with three junctions, where junction 1 and 3 are of the same

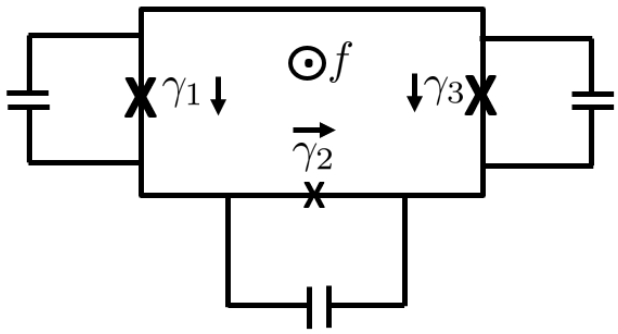

Figure 2.3: The circuit model of a persistent current qubit containing three Josephson junctions in a loop. γ_i is the junction phase and f represents the external flux in the loop.

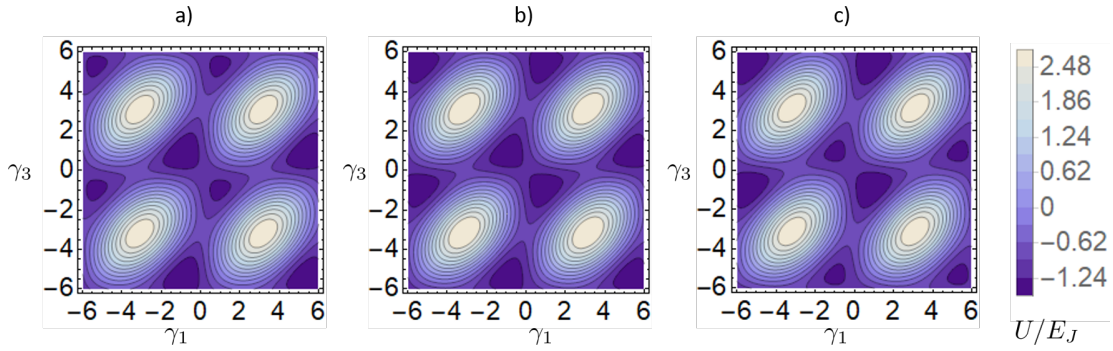

Figure 2.4: Contour plots of the potential energy of a persistent current qubit versus two phases γ_1 and γ_3 when the external flux a) $f = 0.48$, b) $f = 0.5$ and c) $f = 0.52$. The potential energy is in unit of E_J.

size and junction 2 have a smaller size. The size ratio of junction 2 to junction 1 is α. Comparing to the rf-SQUID, the qubit loop of the persistent current qubit is much smaller, since the large Josephson inductances of junction 2 and 3 contribute to the loop inductance. Neglecting the loop self inductance, the phase relation is

$$\gamma_1 + \gamma_2 - \gamma_3 = -2\pi f. \tag{2.17}$$

γ_1 and γ_3 are chosen as the degrees of freedom. Following a similar quantization process as the RF-SQUID, the Hamiltonian of the qubit is found to be

$$H = \frac{\hbar^2}{2} E_c p^T C^{-1} p + U, \tag{2.18}$$

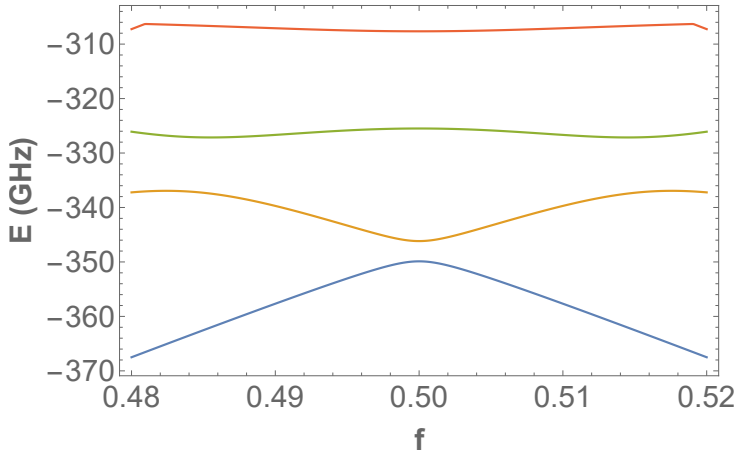

Figure 2.5: The lowest four energy levels of a persistent current qubit with $E_J/E_c = 13.4$ versus the external flux.

where p represents the conjugate momenta of the junction phases

$$p = \begin{pmatrix} p1 \\ p3 \end{pmatrix}, \tag{2.19}$$

and C is a matrix of ratios of junction sizes

$$C = \begin{pmatrix} 1+\alpha & \alpha \\ \alpha & 1+\alpha \end{pmatrix}. \tag{2.20}$$

The potential energy of the circuit is the sum of the magnetic energies of all junctions

$$U = -E_J \left(\cos\gamma_1 + \alpha\cos\left(2\pi f + \gamma_1 - \gamma_3\right) + \cos\gamma_3\right). \tag{2.21}$$

Fig 2.4 shows the plot of the potential energy over two phases γ_1 and γ_3. There are two potential wells near the center of each plot. The states in two wells have different macroscopic properties corresponding to the currents in the qubit loop flowing in the clockwise and counterclockwise directions, so these two states are call the persistent current states. The current is persistent as the circuit is superconducting. These states are also called the flux states because the persistent currents flowing in opposite directions generate fluxes with opposite signs. When the external flux f approaches 0.5, the double well potential becomes symmetric and the barrier between two wells decreases, which allows the quantum tunneling, so the eigenstates of the qubit are superposition states of the two

flux states. When f is away from the symmetry point, the barrier increases and finally one of the potential well vanishes, so the qubit eigenstate is one of two flux states.

The qubit Hamiltonian in the basis of the flux states is

$$H = -\frac{\hbar\Delta}{2}\sigma_x - \frac{\hbar\epsilon}{2}\sigma_z, \tag{2.22}$$

where σ_x and σ_z are Pauli operators, and $\hbar\Delta$ is the minimum qubit gap. $\hbar\epsilon$ is the energy difference between two potential wells, which is related to the persistent current I_p and the external flux by

$$\hbar\epsilon = 2I_p\Phi_0\left(f - \frac{1}{2}\right). \tag{2.23}$$

Figure 2.5 plots the lowest several energy levels of a persistent current qubit. The energy structure shows very large anharmonicity, which makes it possible to approximate the flux qubit as a two-level system consisting of the lowest two energy eigenstates. The point, where the transition energy between the two energy levels reaches the minimum, is defined as the symmetry point. For a single-loop persistent current qubit, the symmetry point is at $f = 0.5$. The Hamiltonian in the energy eigenbasis is

$$H = -\frac{1}{2}\hbar\Omega\sigma_z, \tag{2.24}$$

where Ω is the qubit frequency given by

$$\Omega = \sqrt{\epsilon^2 + \Delta^2}. \tag{2.25}$$

The energy eigenstates are

$$|0\rangle = \cos\frac{\theta}{2}|l\rangle + \sin\frac{\theta}{2}|r\rangle \tag{2.26}$$

$$|1\rangle = \cos\frac{\theta}{2}|l\rangle - \sin\frac{\theta}{2}|r\rangle, \tag{2.27}$$

where $|l\rangle$ and $|r\rangle$ are the flux states in the left and right potential well.

2.3 Open transmission lines

A transmission line is waveguide for electromagnetic waves with high frequencies, such as microwaves. Typical types of transmission lines includes coaxial cables, planar lines, etc. Since many superconducting circuits are constructed on a wafer and hence they are two

dimensional circuits, the coplanar waveguide (CPW), as a type of planar lines, is widely used in superconducting devices. The structure of a CPW is shown in Fig 2.6. Microwaves move forward along the center line and return through the ground planes. Since the CPW has comparable lengths to the wavelengths of microwaves, it is modeled as distributed element, where the capacitance between the center line and ground planes, as well as the self inductance of center line are uniformly distributed. Figure 2.7 shows the distributed element model of the CPW, which is a chain of LC oscillators. Each element takes the length of Δx, so the inductance and capacitance per element is $l_0\Delta x$ and $c_0\Delta x$, with l_0 and c_0 the inductance and capacitance per unit length. Applying the Kirchhoff's laws to the nodes of an element, we obtain the voltage-current relations

$$V(x+dx,t) = V(x,t) - \frac{dI(x,t)}{dt} l_0 dx, \tag{2.28}$$

$$I(x+dx,t) = I(x,t) - \frac{dV(x,t)}{dt} c_0 dx, \tag{2.29}$$

Taking the limit $\Delta x \to 0$, we arrive at the telegraph equations of the transmission line

$$\frac{\partial V(x,t)}{\partial x} = -l_0 \frac{\partial I(x,t)}{\partial t} \tag{2.30}$$

$$\frac{\partial I(x,t)}{\partial x} = -c_0 \frac{\partial V(x,t)}{\partial t} \tag{2.31}$$

The voltages in the transmission line contains the right-moving and left-moving components such that

$$V(x,t) = V^{\rightarrow}(x,t) + V^{\leftarrow}(x,t), \tag{2.32}$$

$$I(x,t) = \frac{1}{Z} V^{\rightarrow}(x,t) - V^{\leftarrow}(x,t), \tag{2.33}$$

where $Z = \sqrt{l_0/c_0}$ is the characteristic impedance. Applying them to the telegraph equations, we have

$$v \frac{\partial V^{\rightarrow}(x,t)}{\partial x} = -\frac{\partial V^{\rightarrow}(x,t)}{\partial t}, \tag{2.34}$$

$$v \frac{\partial V^{\leftarrow}(x,t)}{\partial x} = \frac{\partial V^{\leftarrow}(x,t)}{\partial t}, \tag{2.35}$$

with $v = \frac{1}{\sqrt{l_0 c_0}}$ the phase velocity of the wave.

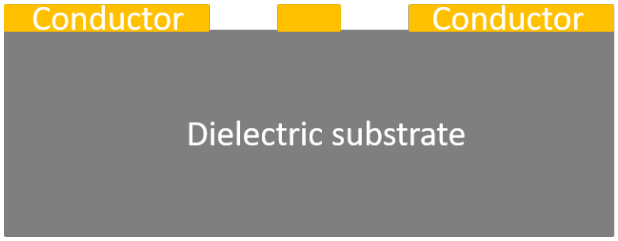

Figure 2.6: The diagram of the cross section of a coplanar waveguide. The CPW is on top of a dielectric substrate and it consists of a center conductor and two ground planes at two sides.

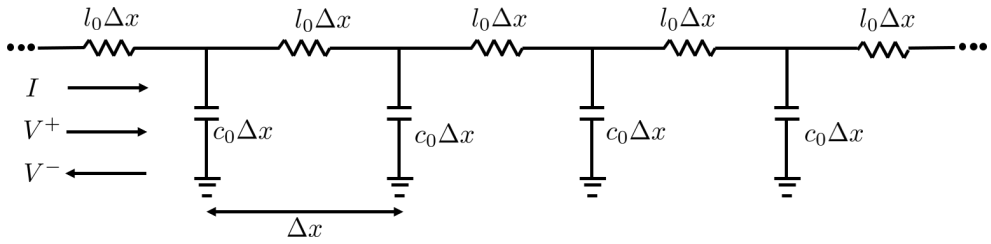

Figure 2.7: The distributed model of an open transmission, which is modeled as a infinite long chain of LC oscillators. l_0 and c_0 are the inductance and capacitance per unit length. Δx is the length of each element. I is the current in the open transmission line, and V^+ and V_- represent the right-moving and left-moving voltage respectively.

2.3.1 Quantization

In this section, we are going to show the quantization process of an infinite long transmission line, which is also called the open transmission line. The system energy contains the charging energies stored in the capacitors and the magnetic energies stored in the inductances. The Lagrangian of an open transmission line is written as

$$\mathcal{L}(x,t) = \int_0^\infty dx \left(\frac{c_0}{2} V^2(x,t) + \frac{l_0}{2} I^2(x,t) \right). \tag{2.36}$$

To express the Lagrangian in terms of the conjugate variables, the flux node variable is introduced and it is defined as the flux generated at position x

$$\Phi(x,t) = \int_{-\infty}^{t} V(x,t')dt'. \tag{2.37}$$

The voltage is written as the derivative of the flux node variable

$$V(x,t) = \frac{\partial \Phi(x,t)}{\partial t}. \tag{2.38}$$

Substituting this equation into Eq 2.30, we have the expression of the current

$$I(x,t) = -\frac{1}{l_0}\frac{\partial \Phi(x,t)}{\partial x}. \tag{2.39}$$

Then the Lagrangian in terms of the flux node variable is found as

$$\mathcal{L}(x,t) = \int_0^\infty dx \left(\frac{c_0}{2} \left(\partial_t \Phi(x,t)\right)^2 - \frac{1}{2l_0} \left(\partial_x \Phi(x,t)\right)^2 \right). \tag{2.40}$$

The canonical conjugate momentum of $\Phi(x,t)$ is the charge density

$$q(x,t) = \frac{\partial \mathcal{L}}{\partial \dot{\Phi}} = c_0 \dot{\Phi}(x,t). \tag{2.41}$$

Following the Legendre transformation, the Hamiltonian is found as

$$H = \int_0^\infty dx \left(\frac{1}{2c_0} q^2(x,t) + \frac{1}{2l_0} \left(\partial_x \Phi(x,t)\right)^2 \right). \tag{2.42}$$

The Lagragian is justified by the Euler-Lagrange equation $\frac{d}{dt}\frac{\partial \mathcal{L}}{\partial \dot{\Phi}} = \frac{\partial \mathcal{L}}{\partial \Phi}$, which gives

$$c_0 \ddot{\Phi}(x,t) - \frac{1}{l_0}\frac{\partial^2 \Phi(x,t)}{\partial t^2} = 0, \tag{2.43}$$

we can find that the general solution of the flux node variable is in the form of plane waves. Assuming the transmission line has a finite length L and imposing the periodic boundary condition on it, the flux field equals to the sum of k plane waves with different modes,

$$\Phi(x,t) = \frac{1}{N} \sum_k \left(c_k e^{i(kx - \omega_k t)} + c_k^* e^{-i(kx - \omega_k t)} \right). \tag{2.44}$$

The wavevector $k = 2\pi m/L$ gives the wavelength $\lambda_k = L/m$ and m is any integer. N is a normalization parameter, which will be determined later. c_k and c_k^* are amplitudes, and $\omega_k = kv = k/\sqrt{c_0 l_0}$ is the angular frequency of mode k. For the open transmission line, there are infinite number of modes. Substituting Eq 2.44 into Eq 2.42, the Hamiltonian becomes

$$H = \frac{L}{N^2} c_0 \sum_k 2\omega_k^2 |c_k|^2. \tag{2.45}$$

Taking the normalization parameter $N = \sqrt{Lc_0}$,

$$H = 2\sum_k \omega_k^2 |c_k|^2. \tag{2.46}$$

Defining the amplitude of mode k as $A_k(t) = A_k(0)e^{-i\omega_k t}$ and $A_k(0) = \sqrt{2}\omega_k c_k$, the Hamiltonian in terms of these variables is

$$H = \frac{1}{2}\sum_k \left(A_k(t)A_k^*(t) + A_k^*(t)A_k(t)\right). \tag{2.47}$$

The flux field turns into

$$\Phi(x,t) = \frac{1}{\sqrt{2Lc_0}}\sum_k \frac{1}{\omega_k}\left(A_k(0)e^{i(kx-\omega_k t)} + A_k^*(0)e^{-i(kx-\omega_k t)}\right). \tag{2.48}$$

Using Eq 2.41, the expression of the charge density is

$$q(x,t) = i\sqrt{\frac{c_0}{2L}}\sum_k \left(A_k(0)e^{i(kx-\omega_k t)} - A_k^*(0)e^{-i(kx-\omega_k t)}\right). \tag{2.49}$$

In experiments, the voltage can be easily controlled and measured, so it is interesting to write down its expression. Using Eq 2.38, we have

$$V(x,t) = i\frac{1}{\sqrt{2Lc_0}}\sum_k \left(A_k(0)e^{i(kx-\omega_k t)} - A_k^*(0)e^{-i(kx-\omega_k t)}\right) \tag{2.50}$$

Analogical to the position and momentum variables of a quantum harmonic oscillator, the flux and charge variables, $\Phi(x,t)$ and $q(x,t)$, are promoted to quantum operators, and they follow the commutation relation

$$\left[\hat{\Phi}(x,t), \hat{q}(x',t)\right] = i\hbar\delta(x-x'). \tag{2.51}$$

Then, we can see that the amplitude of each mode k follows

$$\left[\hat{A}_k, \hat{A}_{k'}^\dagger\right] = \hbar\omega_k\delta_{kk'}, \tag{2.52}$$

and it is related to the bosonic creation and annihilation operators as

$$\hat{A}_k = \sqrt{\hbar\omega_k}\hat{a}_k. \tag{2.53}$$

We obtain the quantized Hamiltonian

$$\hat{H} = \sum_k \hbar\omega_k(\hat{a}_k^\dagger \hat{a}_k + \frac{1}{2}), \tag{2.54}$$

so each mode k corresponds to a zero energy term $\frac{1}{2}\hbar\omega_k$ along with a harmonic oscillator, where

$$\begin{aligned} \hat{a}_k^\dagger|n_k\rangle &= \sqrt{n_k+1}|n_k+1\rangle \\ \hat{a_k}|n_k\rangle &= \sqrt{n_k}|n_k-1\rangle. \end{aligned} \tag{2.55}$$

$|n_k\rangle$ represents the photon number state with n_k photons stored in mode k. The voltage and flux operators expressed in terms of the creation and annihilation operators are

$$\hat{V}(x,t) = \frac{i}{\sqrt{2Lc_0}} \sum_k \sqrt{\hbar\omega_k} \left[\hat{a}_k e^{i(kx-\omega_k t)} - \hat{a}_k^\dagger e^{-i(kx-\omega_k t)}\right], \tag{2.56}$$

$$\hat{\Phi}(x,t) = \frac{1}{\sqrt{L}} \sum_k \sqrt{\frac{\hbar}{2c_0\omega_k}} \left(\hat{a}_k e^{i(kx-\omega_k t)} + \hat{a}_k^\dagger e^{-i(kx-\omega_k t)}\right). \tag{2.57}$$

Chapter 3

Strong coupling in superconducting circuits

In this chapter, we discuss how two-level systems interact with quantized electromagnetic fields, focusing on superconducting circuits. We first introduce a general model for light-matter interaction called the spin-boson model in Section 3.1. We then discuss the classification of the coupling regimes in Section 3.1.1, the rotating wave approximation in Section 3.1.2, decoherence in Section 3.1.3 and the adiabatic renormalization of the tunneling frequency in Section 3.1.4. In Section 3.2, we follow the quantization process introduced in the Appendix of [15] to quantize a flux qubit that is coupled to an open transmission line, and analyze the qubit decoherence.

3.1 Spin-boson model

The spin-boson model [12] is important in many branches of physics and chemistry. It has been extensively used in the field of the light-matter interaction. Generally, it describes the interaction between spins and bosonic baths, where spins denote two-level systems such as qubits, and the bosonic bath refers to an environment with bosonic particles, such as photons. In spin-boson model, the bath is described as a combination of harmonic oscillators, generating discrete or continuous modes depending on the number of harmonic oscillators. In superconducting circuits, the spin-boson model is widely applied to model the dynamics of superconducting qubits coupled to transmission line resonators, open transmission lines or other baths.

The typical spin-boson Hamiltonian of a qubit coupled to a bath of harmonic oscillators is written as

$$\hat{H}_{\mathrm{SB}} = \hat{H}_0 + \hat{H_{\mathrm{int}}} = \frac{\hbar\Delta}{2}\hat{\sigma}_z + \sum_k \omega_k \hat{a}_k^\dagger \hat{a}_k + (\sin\theta\hat{\sigma}_x + \cos\theta\hat{\sigma}_z)\sum_k g_k(\hat{a}_k^\dagger + \hat{a}_k), \tag{3.1}$$

where $\hat{H}_0$ is the sum of the first two terms on the RHS, which are the Hamiltonian of the qubit and the bath, and $\hat{H_{\mathrm{int}}}$ is the third term representing the interaction Hamiltonian. Δ is the qubit frequency, $\hat{\sigma}_x$ and $\hat{\sigma}_z$ are Pauli operators, ω_k, $\hat{a}_k$ and $\hat{a}_k^\dagger$ are mode frequency, annihilation and creation operators for the harmonic oscillator in mode k. The interaction is via σ_x and σ_z coupling, which corresponds to qubit relaxation and dephasing respectively. θ is determined by the qubit bias, and it controls the components of two types of coupling in the way that when the qubit is at the symmetry point, $\sin\theta = 1$, so σ_z couling vanishes and there is only σ_x coupling. As the qubit moves away from the symmetry point, σ_x coupling decreases, while σ_z coupling increases. g_k is a describing the interaction strength between the qubit and mode k.

The interaction between the qubit and the bath is characterized by the spectral density function

$$J(\omega) = \frac{2\pi}{\hbar^2}\sum_k g_k^2 \delta(\omega - \omega_k), \tag{3.2}$$

which relates the mode coupling strength to the mode frequency. Ohmic environment is commonly encountered in experiments. In this case, the spectral density is given by

$$J(\omega) = \frac{2\pi}{\hbar^2}\sum_k g_k^2 \delta(\omega - \omega_k) = \pi\omega\alpha_{\mathrm{SB}}. \tag{3.3}$$

α_{SB} is a dimensionless constant that determines coupling strength and the quantum phase of the spin-boson model [12, 27]. For $\alpha_{\mathrm{SB}} < 1/2$, the system is in the Markovian regime, where the dynamics is coherent. When α is larger than $\frac{1}{2}$, the quantum phase changes and the system dynamics becomes incoherent. For $1/2 < \alpha_{\mathrm{SB}} < 1$, the model is in the overdamped regime, and when $\alpha_{\mathrm{SB}} > 1$, the tunneling between two states of the two-level system is completely suppressed and the model enters into the localized regime.

3.1.1 Coupling strength

The coupling between a two-level system and the bath reaches the strong coupling regime when the interaction strength is stronger than qubit and photon loss. In this regime,

the rotating wave approximation (RWA) is frequently applied to describe the dynamics of a qubit coupled to a single mode harmonic oscillator. This approximation is discussed in detail in Section 3.1.2. As the coupling strength increase, diferent coupling regimes is characterized by the ratio Γ/Δ, where Γ and Δ are the relaxation rate and tunneling frequency of the two-level system. In the strong coupling regime, the qubit decay rate is much smaller than the qubit transition frequency $\Gamma/\Delta \ll 1$. When the relaxation rates increases and becomes comparable to the tunneling frequency or $\Gamma/\Delta \gtrsim 0.1$, it reaches the ultrastrong coupling (USC) regime. The rotating wave approximation breaks, but the Born-Markovian approximation still holds, and is used to analyze the qubit dynamics, which will be discussed in Section 3.1.3. When Γ approaches or exceeds the tunneling frequency $\Gamma/\Delta \sim 1$, the perturbative treatments breaks and it enters into the non-perturbative USC regime, where Born-Markov approximation breaks. Three methods, quasi-adiabadic propagator path integral[14], the matrix product states [15] and dynamical polaron ansatz [16], are proposed to analyze the dynamics in both USC and non-perturbaive USC regime without any perturbation approximation. The last one has been verified by the experiment results in [1].

3.1.2 Rotating wave approximation

We consider a model where a qubit is at the symmetry point and is coupled to a single harmonic oscillator. The interaction Hamiltonian in qubit energy basis may be written as

$$\hat{H}_{\text{int}} = g\hat{\sigma}_x(\hat{a}_k^\dagger + \hat{a}_k) = g(\hat{\sigma}_+ + \hat{\sigma}_-)(\hat{a}_k^\dagger + \hat{a}_k), \tag{3.4}$$

where $\hat{\sigma}_x = \hat{\sigma}_+ + \hat{\sigma}_-$, and $\hat{\sigma}_+ = |e\rangle\langle g|$ and $\hat{\sigma}_- = |g\rangle\langle e|$ are ladder operators of the qubit. To analyze the qubit dynamics, we write the interaction Hamiltonian in the interaction picture

$$H_{\text{int}}(t) = U(t)H_{\text{int}}U(t)^\dagger, \tag{3.5}$$

where $U(t)$ is a unitary transform operator and it is given as

$$\begin{aligned} U(t) &= e^{iH_0 t} \\ &= e^{i(\frac{\hbar\Delta}{2}\sigma_z + \hbar\omega a^\dagger a)t}, \end{aligned} \tag{3.6}$$

Substituting it to the interaction Hamiltonian, we have

$$\begin{aligned} H_{\text{int}}(t) &= g(\sigma_+ e^{i\Delta t} + \sigma_- e^{-i\Delta t})(a^\dagger e^{i\omega t} + a e^{-i\omega t}) \\ &= g(e^{i(\omega+\Delta)t}\sigma_+ a^\dagger + e^{-i(\omega-\Delta)t}\sigma_+ a + e^{i(\omega-\Delta)t}\sigma_- a^\dagger + e^{-i(\omega+\Delta)t}\sigma_+ a). \end{aligned} \tag{3.7}$$

When the detuning between the qubit and the mode frequency is very small $|\Delta - \omega| \to 0$, the terms $e^{i(\omega+\Delta)t}\sigma_+ a^\dagger$ and $e^{-i(\omega+\Delta)t}\sigma_+ a$ will oscillate at very fast rates compared to the other two terms due to $|\omega - \Delta| \ll \omega + \Delta$. Then, for any interaction that is slower than $|\omega - \Delta|$, the two fast oscillating terms can be eliminated since they will be averaged out in a short time. However, as the interaction strength increases and becomes comparable to the qubit frequency or the mode frequency, the two fast oscillating terms will not be averaged out quickly, so RWA is applicable in the strong coupling regime, but it breaks in the ultrastrong coupling regime.

Applying the RWA to a single-qubit and single-mode system, the system Hamiltonian becomes the famous Jaynes-Cummings Hamiltonian [3],

$$H_{\mathrm{JC}} = \frac{\hbar\Delta}{2}\sigma_z + \hbar\omega a_k^\dagger a_k + g(\sigma_+ a + \sigma_- a^\dagger), \tag{3.8}$$

which describes a coherence interaction with the qubit and photon excitations conserved. Two simple interaction processes are that the qubit relaxes from the excited state to the ground state by emitting a photon into the resonator, and the qubit absorbs a photon from the resonator to be excited from the ground state to the excited state.

3.1.3 Decoherence

The decoherence of a system arises from the interaction with the environment. There are two types of decoherence, namely the energy relaxation and the pure dephasing. The energy relaxation is a process where the system releases energy into the environment and decays into its equilibrium state. The pure dephasing does not involve any energy exchange, while it is a process where the phases of a quantum superposition state are affected by the environmental noise, causing the loss of the quantum information. In this section, we present the derivation of the Born-Markov master equation [27], from which the expression of the relaxation rate and the pure dephasing rate is calculated.

We start with a model with the Hamiltonian as

$$H = H_{\mathrm{sys}} + H_b + H_{\mathrm{int}}, \tag{3.9}$$

which is composed of the system Hamiltonian $H_{\mathrm{sys}} = \hbar\sum_i \omega_i |i\rangle\langle i|$, the bath Hamiltonian H_b and the interaction Hamiltonian H_{int}. We write the density matrix of the model ρ_0 in the interaction picture

$$\rho(t) = U(t)\rho_0 U^\dagger(t), \tag{3.10}$$

where $U(t) = e^{i(H_{\text{sys}}+H_b)t}$ is a unitary transformation and bring the system into the rotating frame. The time-evolution of the density matrix in the interaction picture is calculated with the Liouville von Neumann equation,

$$\dot{\rho} = -\frac{i}{\hbar}\left[H_{\text{int}}, \rho(t)\right]. \tag{3.11}$$

H_{int} is the interaction Hamiltonian in the interaction picture and is given by

$$\begin{aligned} H_{\text{int}} &= U(t) H_{\text{int}}^{S} U^{\dagger}(t) \\ &= A(t) f(t), \end{aligned} \tag{3.12}$$

with H_{int}^{S} denoting its expression in the Schrödinger picture, $A(t)$ the system operator, and $X(t)$ the bath operator. We formally integrate Eq 3.11 and obtain

$$\rho(t) = \rho(0) - i\int_0^t d\tau \left[H_{\text{int}}(\tau), \rho(\tau)\right]. \tag{3.13}$$

Then, it is inserted back into Eq 3.11 yielding

$$\dot{\rho}(t) = -i[H_{\text{int}}, \rho(0)] - \frac{1}{\hbar^2}\int_0^t d\tau \left[H_{\text{int}}(t), [H_{\text{int}}(\tau), \rho(\tau)]\right]. \tag{3.14}$$

Assuming that at $t = 0$, there is no correlation between the system and the bath, so $\rho(0) = \rho_{\text{sys}}(0) \otimes \rho_b(0)$. Then we trace over the bath degrees of freedom of the above equation and obtain the derivative of the density matrix that is only in the system degrees of freedom

$$\dot{\rho}_{\text{sys}}(t) = -\frac{1}{\hbar^2}\int_0^t d\tau \text{Tr}_b\{[H_{\text{int}}(t), [H_{\text{int}}(\tau), \rho(\tau)]]\} \tag{3.15}$$

We apply the Born approximation, which assumes the interaction is weak so that the bath eigenstates are not altered significantly and they are assumed to remain at their initial states through the whole interaction process. The density matrix is thus can be written as the tensor product of the system and the bath density matrix $\rho(t) = \rho_{\text{sys}}(t) \otimes \rho_b(0)$ for any time t. Plugging it into Eq 3.15, we have

$$\dot{\rho}_{\text{sys}}(t) = -\frac{1}{\hbar^2}\int_0^t d\tau \text{Tr}_b\{[H_{\text{int}}(t), [H_{\text{int}}(\tau), \rho_{\text{sys}}(\tau) \otimes \rho_b(0)]]\} \tag{3.16}$$

We take another approximation, the Markov approximation, which assumes the excitations of the bath caused by the system decay fast, wherein the time-correlations of the bath states are lost fast, so the time-evolution of the density matrix depends only on its current state

and we can replace $\rho_{\rm sys}(\tau) \to \rho_{\rm sys}(t)$. Expanding the commutators and apply the rotating wave approximation, we arrive at the Born-Markov master equation

$$\dot{\rho}(t) = \frac{1}{2\hbar^2} \sum_{jk} |A_{jk}|^2 S(\omega_{jk}) \left[2|k\rangle\langle j|\rho(t)|j\rangle\langle k| - \rho(t)|j\rangle\langle j| - |j\rangle\langle j|\rho(t)\right], \tag{3.17}$$

where $\omega_{jk} = \omega_j - \omega_k$, $A_{jk} = \langle j|A|k\rangle$ is the matrix element of the system operator, and $S(\omega_{jk})$ is the spectral density of the environment, which is defined as the Fourier transform of the time correlation of the environmental operator

$$S(\omega_{jk}) = \int_{-\infty}^{\infty} d\tau e^{i\omega\tau} \langle f(\tau) f(0)\rangle. \tag{3.18}$$

Energy relaxation

We consider the case of the spin-boson model, then $|j\rangle$ or $|k\rangle$ in Eq 3.17 represents the state 0 or 1. We consider the relaxation process, which corresponds to the σ_x coupling term in the spin-boson Hamiltonian, so the two states are set that $j \neq k$ and the master equation becomes

$$\begin{aligned} \dot{\rho}_{\rm sys}(t) =& \frac{\Gamma_{1\to 0}}{2} \left(2\sigma_- \rho_{\rm sys}(t)\sigma_+ - \sigma_+\sigma_-\rho_{\rm sys}(t) - \rho_{\rm sys}(t)\sigma_+\sigma_-\right) + \\ & \frac{\Gamma_{0\to 1}}{2} \left(2\sigma_+ \rho_{\rm sys}(t)\sigma_- - \sigma_-\sigma_+\rho_{\rm sys}(t) - \rho_{\rm sys}(t)\sigma_-\sigma_+\right), \end{aligned} \tag{3.19}$$

where $\Gamma_{1\to 0}$ and $\Gamma_{0\to 1}$ are the decay rate and the excitation rate of the system respectively and have the form

$$\Gamma_{1\to 0} = \frac{1}{\hbar^2} |A_{10}|^2 S(\omega_{10}), \tag{3.20}$$

$$\Gamma_{0\to 1} = \frac{1}{\hbar^2} |A_{10}|^2 S(\omega_{01}). \tag{3.21}$$

The sum of them is the relaxation rate $\Gamma_1 = \Gamma_{1\to 0} + \Gamma_{0\to 1}$. In the spin-boson model, the interaction Hamiltonian in the interaction picture is

$$\begin{aligned} H_{\rm int} &= U(t) H_{\rm int,S} U^\dagger(t) \\ &= \sin\theta \left(\sigma_+ e^{i\Delta t} + \sigma_- e^{-i\Delta t}\right) \sum_k g_k \left(a_k^\dagger e^{i\omega_k t} + a_k e^{-i\omega_k t}\right) \\ &= A(t) f(t), \end{aligned} \tag{3.22}$$

so the relaxation rate is calculated to be [1]

$$\Gamma_1 = \frac{1}{\hbar^2}\sin^2\theta \int_{-\infty}^{\infty} d\tau e^{-i\Delta\tau}\langle |f(\tau), f(0)|_+\rangle, \tag{3.23}$$

where $\langle |f(\tau), f(0)|_+\rangle$ denotes the symmetrized bath correlation function and is given by

$$\begin{aligned}\langle |f(\tau), f(0)|_+\rangle &= \mathrm{Tr}_b\{[(f(\tau)f(0) + f(0)f(\tau))\rho_b(0)]\} \\ &= \sum_k g_k^2 \left[(1+n_k)e^{i\omega_k\tau} + n_k e^{-i\omega_k\tau}\right],\end{aligned} \tag{3.24}$$

with n_k the average number of photons of mode k, and

$$n_k = \frac{1}{e^{\hbar\omega_k/k_BT} - 1}. \tag{3.25}$$

For simplicity, we assume the temperature is at zero, so $n_k = 0$. Plugging it into the expression of the relaxation rate Γ_1, we have

$$\Gamma_1 = \frac{1}{\hbar^2}\sin^2\theta \sum_k g_k^2 \int_{-\infty}^{\infty} d\tau e^{i(\omega_k - \Delta)\tau}. \tag{3.26}$$

The equation contains the Fourier transform of the delta function

$$\delta(\omega) = \frac{1}{2\pi}\int_{-\infty}^{\infty} d\tau e^{i\omega t}, \tag{3.27}$$

so the relaxation rate

$$\Gamma_1 = \frac{2\pi}{\hbar^2}\sin^2\theta \sum_k g_k^2 \delta(\Delta - \omega_k). \tag{3.28}$$

Comparing this expression with the spectral density function Eq 3.2, we find the relation between Γ_1 and α_{SB}

$$\Gamma_1 = \sin^2\theta J(\Delta) = \sin^2\theta \pi \alpha_{SB}\Delta. \tag{3.29}$$

This equation is obtained with the Born-Markov approximation and the rotating-wave approximation, which are valid when $\alpha \to 0$. However, it turns out that the estimated results of Γ/Δ using Eq 3.29 is very close to the measured values up to $\alpha < 0.5$ in [1], so this equation is valid ultil $\alpha < 0.5$ or $\Gamma_1/\Delta \sim 1.5$. It is also found that when $\alpha > 0.5$, this equation provides a lower bound for estimation of Γ_1/Δ compared to the exact solution solved with the polaron method [16]. The error of the estimation increases with the coupling strength.

Pure dephasing

We consider a qubit affected by some noise, which results in the fluctuations of qubit frequency, so in the rotating frame at z axis with the qubit frequency, the Hamiltonian may be written as

$$H = \frac{\hbar\epsilon(t)}{2}\sigma_z, \tag{3.30}$$

where $\epsilon(t)$ is a random small value with an average at 0. If we prepare a superposition state $a_0|0\rangle + a_1|1\rangle$, the phases of the state will change due to the noise and the state will become $a_0 e^{-i\phi(t)/2}|0\rangle + a_1 e^{i\phi(t)/2}|1\rangle$, where $\phi(t) = \int_0^t dt'\epsilon(t')$. If experiments are repeated, the resulted states becomes uncertain since they depend on the random phases $\phi(t)$. Thus, the information of the phases are lost and the decoherence happens to the system. Since the average of $\phi(t)$ is zero, the system does not lose any energy, and this type of decoherence is named as pure dephasing.

Due to the conservation of energy, transitions between qubit eigenstates are forbidden, so Eq 3.17 represents the dephasing process when $j = k$, and we have

$$\dot{\rho(t)} = \Gamma_\varphi \mathcal{D}[\sigma_z]\rho(t), \tag{3.31}$$

where the superoperator $\mathcal{D}[\sigma]\rho(t) = \sigma\rho(t)\sigma^\dagger - \frac{1}{2}\sigma^\dagger\sigma\rho(t) - \frac{1}{2}\rho(t)\sigma^\dagger\sigma$, and the dephasing rate is

$$\Gamma_\varphi = \frac{1}{2\hbar^2}\left(|A_{11} - A_{00}|^2\right) S(0). \tag{3.32}$$

3.1.4 Adiabatic renormalization

As introduced in Section 2.2.2, the flux-basis Hamiltonian of a flux qubit at the symmetry point is

$$\begin{aligned} H &= -\frac{\hbar\Delta}{2}\sigma_x \\ &= \frac{\hbar\Delta}{2}(|l\rangle\langle r| + |r\rangle\langle l|), \end{aligned} \tag{3.33}$$

where $|l\rangle$ and $|r\rangle$ are the flux states in the left and right wells. Δ is the qubit frequency and it is also the tunneling frequency between the symmetric potential wells when the qubit is not interacted with the environment. In the spin-boson model, the qubit is coupled to k harmonic oscillators and the spin-boson Hamiltonian in qubit flux basis is

$$H = -\frac{\hbar\Delta}{2}\sigma_x + \sum_k \hbar\omega_k a_k^\dagger a_k + \sigma_z \sum_k g_k(a_k^\dagger + a_k). \tag{3.34}$$

If considering the effect of the environment, the system states should be expressed as the dressed states due to the correlation with the environment $|Q\rangle \prod_k |n_{Q,k}\rangle$, which is composed of the qubit state $|Q\rangle = |l\rangle$ or $|r\rangle$ and the harmonic oscillator states for all modes. Each harmonic oscillator has two ground states $|0_{l,k}\rangle$ and $|0_{r,k}\rangle$, which corresponds to two qubit states and they are not orthogonal to each other. The transition frequency between the two dressed ground states is

$$\begin{aligned} \Delta' &= \langle r|l\rangle \prod_k \langle 0_{r,k}|0_{l,k}\rangle \\ &= \Delta \prod_k \langle 0_{r,k}|0_{l,k}\rangle, \end{aligned} \tag{3.35}$$

so the transition frequency is renormalized if there is correlation between the qubit and the environment. The resulted transition frequency is renormalized by the Franck-Condon factor [12, 28],

$$\Delta' = \Delta \exp\left(-\frac{1}{2}\sum_k \frac{g_k^2}{\omega_k^2}\right). \tag{3.36}$$

Taking the continuum limit, the renormalized transition frequency becomes

$$\Delta' = \Delta \exp\left(-\frac{1}{2}\int_0^\infty d\omega \frac{J(\omega)}{\omega^2}\right). \tag{3.37}$$

$J(\omega)$ is the spectral density function as in Eq 3.2. The integral is divergent at the low frequency limit when $J(\omega) \sim \omega^s$ with $s \leq 1$. To reduce the effect of low-frequency modes, the integral is modified as

$$\Delta_r = \Delta \exp\left(-\frac{1}{2}\mathcal{P}\int_0^\infty d\omega \frac{J(\omega)}{\omega^2 - \Delta_r^2}\right), \tag{3.38}$$

with $\mathcal{P}$ the Cauchy principal value of the integral. Since the coupling of qubit to the modes with frequencies that are much higher than the qubit frequency is small, an exponential cutoff is commonly taken for an Ohmic bath with the spectral density function [1]

$$J(\omega) = \omega e^{-\omega/\omega_c}. \tag{3.39}$$

The renormalized transition frequency

$$\Delta_r = \Delta_0 (\frac{\Delta_0}{\omega_c})^{\alpha_{\rm SB}/(1-\alpha_{\rm SB})}, \tag{3.40}$$

is observed in the experiment.

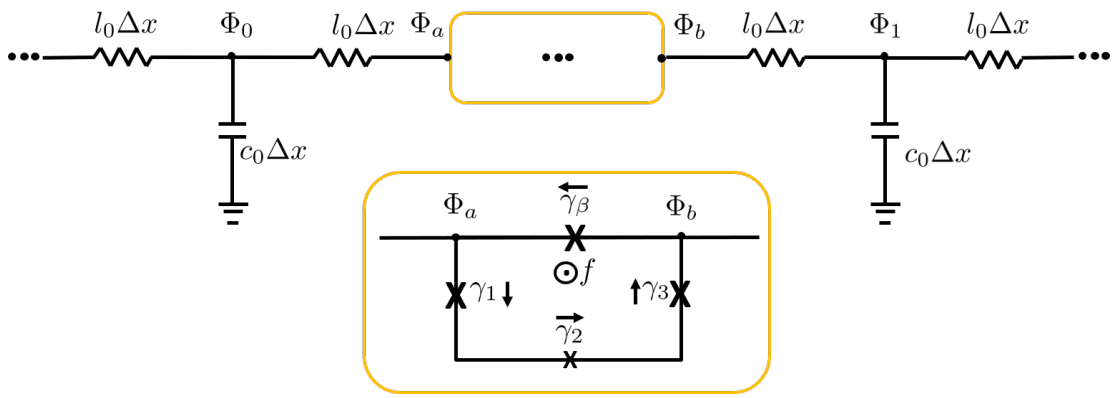

Figure 3.1: The lumped elements circuit model of a persistent current qubit galvanically connected to an open transmission line. The PCQ contains four junctions. Junction 1 and 3 have the same size, the area ratios of junction 2 and β to junction 1 are α and β respectively. The qubit shares the β junction with the transmission line. Φ_i is the flux node variable at the i_{th} node.

3.2 Circuit QED with flux qubits

In this section, we use a circuit quantization method, which was first introduced in [15], to a circuit QED system and present how spin-boson model is applied to analyze the system dynamics. The characteristic of quantization method is its versatility, since it can be implemented on any system consisting of a superconducting artificial atom embedded inside a transmission line. This is realized by analyzing the atom and the transmission line separately. Here, we focus on a special case where a persistent current qubit with four Josephson junctions is galvanically connected to an open transmission line. The lumped elements circuit model is shown in Fig 3.1. The transmission line is modeled as an infinite chain of LC oscillators. The system Hamiltonian consists of the qubit Hamiltonian and the transmission line part

$$H = \sum_{i}^{N} \frac{q_i^2}{2\Delta x c_0} + \sum_{i\neq 0} \frac{(\Phi_{i+1}-\Phi_i)^2}{2\Delta x l_0} + \frac{1}{l_0\Delta x}(\Phi_1-\Phi_b)^2 + \frac{1}{l_0\Delta x}(\Phi_a-\Phi_0)^2 + H_{\rm qb}, \quad (3.41)$$

where q_i is the charge on the $i_{\rm th}$ LC oscillator, Φ_i is the flux node variable as introduced in Section 2.3, $(\Phi_{i+1}-\Phi_i)$ is the flux on the $i_{\rm th}$ LC oscillator and $H_{\rm qb}$ is the qubit Hamiltonian. We convert Φ_a and Φ_b to new variables

$$\Phi_\pm = \Phi_b \pm \Phi_a, \quad (3.42)$$

since $\Phi_\pm$ are qubit variables. By doing the conversion

$$(\Phi_1 - \Phi_b)^2 + (\Phi_a - \Phi_0)^2 = \frac{1}{2}\left[(\Phi_1 - \Phi_b + \Phi_a - \Phi_0)^2 + (\Phi_1 - \Phi_b - \Phi_a + \Phi_0)^2\right], \tag{3.43}$$

the Hamiltonian becomes

$$\begin{aligned} H =& \Delta x \sum_i^N \left[\frac{(q_i/\Delta x)^2}{2c_0} + \frac{1}{2l_0}\left(\frac{\Phi_{i+1} - \Phi_i}{\Delta x}\right)^2\right] + \frac{1}{2l_0\Delta x}\left[(\Phi_1 + \Phi_0) - \Phi_+\right]^2 \\ &+ \frac{1}{l_0\Delta x}(\Phi_1 - \Phi_0)\Phi_- + \frac{1}{2l_0\Delta x}\Phi_-^2 + H_{\text{qb}}. \end{aligned} \tag{3.44}$$

Taking the limit $\Delta x \to 0$, we have $\Phi_1 + \Phi_0 = \Phi_a + \Phi_b$, so the third term is eliminated. Then we write the Hamiltonian in the integral form

$$H = \int_{-\infty}^{\infty}\left[\frac{q(x)^2}{2c_0} + \frac{\partial_x\Phi(x)^2}{2l_0} + \delta(x)\frac{1}{l_0}\partial_x\Phi(x)\Phi_-\right]dx + \frac{1}{2l_0\Delta x}\Phi_-^2 + H_{\text{qb}}, \tag{3.45}$$

where $q_x = q_i/\Delta x$ is the charge density and $\delta(x)$ is the Dirac delta. We can see that the first two terms in the integral has the same form as Eq 2.42, so they represent the Hamiltonian of an open transmission line. The third term is the product of the current in the transmission line and the flux $\Phi_- = \varphi_0\gamma_\beta$ that is generated by the β junction shared between the qubit and the transmission line. $\varphi_0 = \frac{\hbar}{2e}$ is the reduced flux quantum. The current in the transmission line is expressed as the current at $x = 0$, where the qubit is placed. Therefore the third term represents the interaction between the qubit and the transmission line and the interaction Hamiltonian is written as

$$H_{\text{int}} = \delta(x)\frac{1}{l_0}\partial_x\Phi(x)\varphi_0\gamma_\beta. \tag{3.46}$$

The fourth term in the Eq 3.45 is considered as a shift of the qubit potential, which causes a qubit renormalization. To estimate its magnitude, we simplify the expression by replacing the inductance term with $l_0\Delta x = Z_0/\omega$ and replacing the flux operator $\Phi_- = \varphi_0\gamma_\beta = \frac{\hbar}{2e}\gamma_\beta$. The renormalization term is of the order

$$H_{\text{renorm}} \sim \hbar\omega\frac{\hbar}{16Z_0e^2}\gamma_\beta^2. \tag{3.47}$$

Typical impedance Z_0 is in the range of 30 to 100 Ω, and the phase γ_β can be centered around $\pi/2$, so the magnitude of the term is

$$H_{\text{renorm}} \sim \hbar\omega(2.5 - 3.2)(\pi/2)^2. \tag{3.48}$$

The potential of the flux qubit is in the order of $U \sim E_J \cos\gamma$, with $E_J/\hbar \sim 250-800$ GHz. Assuming the frequency of transmission line is resonant with the qubit frequency, we have $\omega \sim 2\pi(1-10)$ GHz. Therefore, the renormalization term is negligible compared to the qubit potential, so it is deleted from the Hamiltonian. Overall, the system Hamiltonian is written as

$$\begin{aligned} H &= H_{\mathrm{TL}} + H_{\mathrm{qb}} + H_{\mathrm{int}} \\ &= \int_{-\infty}^{\infty} \left[\frac{q(x)^2}{2c_0} + \frac{\partial_x \Phi(x)^2}{2l_0} \right] dx + H_{qb} + \delta(x) \frac{1}{l_0} \partial_x \Phi(x) \varphi_0 \gamma_\beta. \end{aligned} \tag{3.49}$$

3.2.1 Relaxation rate

Next, we are going to estimate the coupling strength between the qubit and the transmission line. The interaction Hamiltonian contains a flux field variable $\Phi(x)$, which is the flux field in the transmission line. In Section 2.3, we have derived the expression of the quantized flux field under the condition that the transmission line has finite length L and the periodic boundary conditions are imposed. By substituting the solution Eq 2.57 into Eq 3.46, the interaction Hamiltonian becomes

$$H_{\mathrm{int}} = \frac{1}{l_0} \varphi_0 \gamma_\beta \sum_k \sqrt{\frac{\hbar}{2c_0 \omega_k L}} k \left(i a_k e^{i(kx - \omega_k t)} - i a_k^\dagger e^{-i(kx - \omega_k t)} \right). \tag{3.50}$$

Recall the spin-boson Hamiltonian describing the relaxation process (see Section 3.1),

$$\hat{H}_{\mathrm{SB}} = \hat{H}_0 + \hat{H_{\mathrm{int}}} = \frac{\hbar\Delta}{2} \hat{\sigma}_z + \sum_k \omega_k \hat{a}_k^\dagger \hat{a}_k + \sin\theta \hat{\sigma}_x \sum_k g_k (\hat{a}_k^\dagger + \hat{a}_k). \tag{3.51}$$

In the case of a flux qubit coupled to open transmission line, the qubit bias term is expressed as

$$\sin\theta = \frac{\Delta_s}{\Delta}, \tag{3.52}$$

with Δ the qubit transition frequency and Δ_s the transition frequency at the symmetry point. Comparing Eq 3.50 to the interaction Hamiltonian in Eq 3.51, the coupling strength to mode k is found to be

$$g_k = \frac{1}{l_0} \varphi_0 |\gamma_{\beta 10}| \frac{1}{\sqrt{L}} \sqrt{\frac{\hbar\omega_k}{2c_0 c^2}}, \tag{3.53}$$

where the dispersion relation $k = \omega_k/c$ is applied, $c = \frac{1}{\sqrt{l_0 c_0}}$ is the speed of light in the transmission line, $\gamma_{\beta 10} = \langle 1|\gamma_\beta|0\rangle$ is the matrix element of the phase operator γ_β.

The spectral density is

$$J(\omega) = 2\pi \sum_k (|g_k|/\hbar)^2 \delta(\omega - \omega_k) = 2\pi \sum_k \frac{\omega_k}{2l_0^2 L\hbar c_0 c^2} \varphi_0^2 |\gamma_{\beta 10}|^2 \delta(\omega - \omega_k). \tag{3.54}$$

Since the transmission line is an open transmission line, we convert the discrete modes to the continuous modes and use the density of states $\frac{L}{2\pi}$

$$J(\omega) = 2\int_{-\infty}^{\infty} d\omega_k \frac{\omega_k}{2\hbar_0 l_0^2 c^3} \varphi_0^2 |\gamma_{\beta 10}|^2 \delta(\omega - \omega_k) = \frac{\omega}{\hbar Z_0} \varphi_0^2 |\gamma_{\beta 10}|^2, \tag{3.55}$$

where $Z_0 = \sqrt{\frac{l_0}{c_0}}$ is the characteristic impedance of the transmission line. With Eq 3.29, we find

$$\frac{\Gamma_1}{\Delta} = \frac{\Delta_s^2}{\Delta^2} \frac{1}{2\pi} \frac{R_Q}{Z_0} |\gamma_{\beta 10}|^2, \tag{3.56}$$

with $R_Q = \frac{h}{(2e)^2} \approx 6.5\ \mathrm{k}\Omega$ the quantum resistance. This equation has the same validity as Eq 3.29, so it is correct up to $\alpha_{SB} < 0.5$, and becomes a lower bound for $\alpha > 0.5$. With Z_0 in the range of 30 to 100 Ω and the phase $|\gamma_{\beta 10}| \sim 1$, we can easily achieve $\frac{\Gamma_1}{\Delta} \sim 10$, which is in the non-perturbative USC regime. Considering this equation is a lower bond, the actual achievable coupling strength is even stronger.

3.2.2 Dephasing rate

Since the qubit sits at $x = 0$, it separates the transmission line into two semi-infinite parts. Recall Eq 2.32 and Eq 2.33, we find the voltage-current relation of the transmission line at the position of the qubit to be

$$V(0,t) = V^{\rightarrow}(0,t) + V^{\leftarrow}(0,t), \tag{3.57}$$

$$I(0,t) = \frac{1}{Z}(V^{\rightarrow}(0,t) - V^{\leftarrow}(0,t)). \tag{3.58}$$

Rearranging the equations, we have

$$V^{\rightarrow}(0,t) = V^{\leftarrow}(0,t) + ZI(0,t). \tag{3.59}$$

We assume the system is in an equilibrium state and the qubit does not emit any signal to the transmission line. If there is no left moving signal into the qubit $V^{\leftarrow} = 0$, we have $V^{\rightarrow} = ZI(0,t)$, thus the right semi-infinite transmission line can be treated as an resistor with resistance Z, and so is the left part of the transmission line.

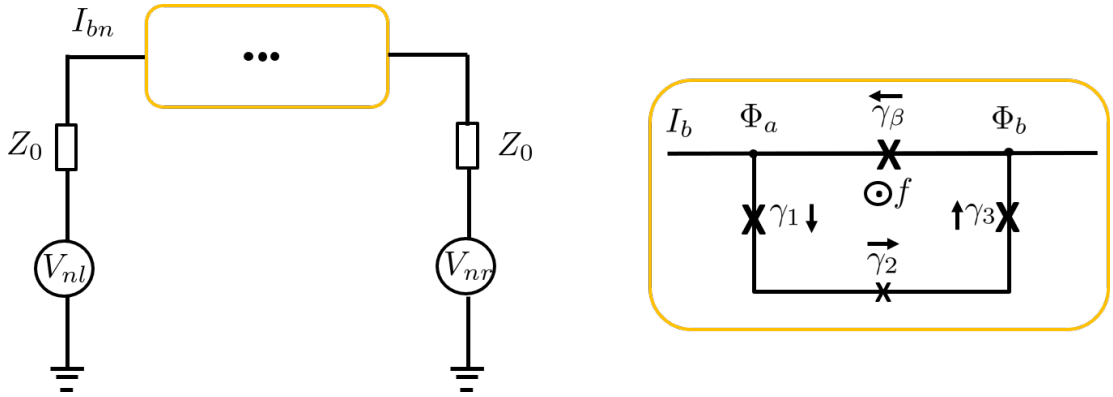

Figure 3.2: Circuit model of a qubit galvanically connected to an open transmission line. The two semi-infinite transmission lines are modeled as two resistors, with resistance euqaling to the characteristic impedance Z_0. V_{nl} and V_{nr} represents the voltage noises in the two transmission lines, and I_{bn} is the current noise. The qubit contains four junctions. Junction 1 and 3 have the same size, the area ratios of junction 2 and β to junction 1 are α and β respectively. The qubit shares the β junction with the transmission line. Φ_i is the flux node variable at the i_{th} node.

The simplified circuit model is shown in Fig 3.2. The quantum fluctuations of the bias current along with thermal fluctuations lead to the decoherence of the qubit. I_{bn} is used to denotes the noise of the current. It results in the fluctuations of the voltages across the two resistors by

$$I_{bn} = \frac{V_{nl} + V_{nr}}{2Z_0}. \tag{3.60}$$

We write the interaction Hamiltonian Eq 3.46 in a simplified form and considering the qubit bias

$$H_{\text{int}} = I_b \varphi_0 \gamma_\beta \cos\theta, \tag{3.61}$$

with $I_b \sim \delta \frac{1}{l_0} \partial_x \Phi(x)$ denoting the current in the transmission line, γ_β the phase across the shared β junction, and the qubit bias term $\cos\theta = \frac{\sqrt{\Delta^2 - \Delta_z^2}}{\Delta}$. We assign $f = I_b$ the bath operator, and $A = \cos\theta \varphi_0 \gamma_\beta$ the qubit operator. In Section 3.1.3, we have derived the expression of the pure dephasing of the spin-boson model, which is applicable here. The dephasing rate is given by Eq 3.32,

$$\Gamma_\varphi = \frac{1}{2\hbar^2} \left(|A_{11} - A_{00}|^2 \right) S_f(0), \tag{3.62}$$

where the matrix elements of the qubit operator is

$$|A_{11} - A_{00}| = \cos\theta\varphi_0|\langle 0|\gamma_\beta|0\rangle - \langle 1|\gamma_\beta|1\rangle| = \varphi_0|\gamma_{\beta 00} - \gamma_{\beta 11}|. \tag{3.63}$$

From Eq 3.18, we find the spectral density of the bath at zero frequency to be

$$S_f(0) = \int_{-\infty}^{\infty} d\tau \langle f(\tau) f(0)\rangle. \tag{3.64}$$

It is related to the current and voltage noises by

$$S_f(0) = S_{I_b}(0) = \frac{\varphi_0^2}{4Z_0^2}[S_{V_{nl}}(0) + S_{Vnr}(0)], \tag{3.65}$$

where Eq 3.60 is applied. The fluctuation-dissipation theorem [29] relates the voltage fluctuations and the impedance as

$$S_{V_n}(\omega) = \hbar\omega \mathrm{Re}[Z_t(\omega)] \left[\coth\frac{\hbar\omega}{2k_BT} + 1\right]. \tag{3.66}$$

With $\omega \to 0$, $\coth\frac{\hbar\omega}{2k_BT} \approx \frac{2k_BT}{\hbar\omega}$, we have

$$S_V(0) = 2Re[Z(0)]k_BT. \tag{3.67}$$

Plugging it into Eq 3.65, we arrive at

$$S_f(0) = \frac{\varphi_0^2}{Z_0} k_BT, \tag{3.68}$$

and finally we obtain the pure dephasing rate

$$\Gamma_\varphi = \frac{\Delta^2 - \Delta_s^2}{\Delta^2}\frac{1}{2}|\gamma_{\beta 00} - \gamma_{\beta 11}|^2 \frac{R_Q}{Z_0}\frac{k_BT}{h}, \tag{3.69}$$

where $R_Q = \frac{h}{(2e)^2}$ is the quantum resistance and $\varphi_0 = \frac{\hbar}{2e}$.

Chapter 4

Fast switchable ultrastrong coupling between superconducting artificial atoms and electromagnetic fields

In this chapter, we propose three experiments to explore the spin boson model in the ultrastrong coupling (USC) regime. A system consisting of a novel design of a superconducting flux qubit with tunble coupling to an open transmission line, qubit control circuits, and qubit state readout circuits is presented. The circuit model and the quantization process of the system, as well as the simulations on system properties such as qubit frequencies, estimated coupling strengths between the qubit and other circuit elements, are discussed. The system is proved to be equipped with fast switchable coupling, with the coupling strength reaching the USC regime, and it is shown to be a promising candidate to perform the these experiments.

4.1 Experiment proposal

The goal of the three experiments is to study the interesting dynamics of a two-level system coupled to a an electromagnetic continuum under the USC regime. The experimental device consists of a flux qubit, which is considered as a two-level system, and it is coupled to an open transmission line providing an eletromagnetic continuum. The flux qubit has two loops, a main loop and a coupler loop, with $f_\epsilon = \Phi_\epsilon/\Phi_0$ and $f_\beta = \Phi_\beta/\Phi_0$ the normalized magnetic fluxes threading in them respectively. The qubit flux bias and coupling strength

to the open transmission line can be controlled by tuning the two fluxes independently. The coupling strength can be adjusted from weak coupling to ultrastrong coupling. The two fluxes are controlled by two flux bias lines, which are also used to drive the qubit. Qubit states are measured in the flux basis with a coplanar waveguide resonator, which is grounded via a DC-SQUID at one end and is capacitively coupled to a feed line on the other end. The persistent currents in the qubit main loop corresponding to the two flux states, are different. This difference can be detected by the DC-SQUID and further reflected in the variation of resonant frequencies of the resonator. By sending a pulse with a frequency close to the resonant frequency through the feed line and measuring the transmission, qubit states can be distinguished. The first two experiments aim to measure the qubit coherence including qubit relaxation and dephasing in the USC regime, and the third experiment is designed to study the renormalization of the qubit frequency. Detailed experiment procedures and pulse sequences are discussed in this section.

4.1.1 Relaxation measurement

Qubit relaxation is characterized by measuring the relaxation time T_1, which is the time it takes for qubit to relax from the first excited state to the ground state. When a qubit is ultrastrongly coupled to an electromagnetic continuum, the relaxation rate becomes very large and the ratio of it to the qubit energy gap reaches 0.1 or more, as introduced in Section 3.1.1. In this regime, theories only give estimations on the relaxation rates, so it is interesting to perform the relaxation measurement in a controllable manner, which can be done with superconducting circuits. Besides, such large relaxation rates make T_1 extremely small and T_1 is in the range of nanoseconds as the qubit gap is about several GHz. However, the time required for the measurement of qubit states normally takes hundreds of nanoseconds or more, so it is a challenge to preform relaxation measurement in ultrastrong coupling regime.

In this section, we present an experiment design for the relaxation measurement in the ultrastrong coupling regime. Figure 4.1 shows the stages and the corresponding pulse sequences for two fluxes f_ϵ and f_β, as well as the readout signal.

- Stage 1: The flux biases are set such that the qubit is at the symmetry point (characterized by a symmetric double well potential). The ground state is prepared by waiting for a time longer than the qubit relaxation time. This point should also be a weak coupling point, where the relaxation rate is small. A π pulse is applied through f_ϵ to excite the qubit to the excited state. Preparation of the excited state with high

fidelity relies on the relaxation rate being small, which minimizes relaxation during the pulse.

- Stage 2: The bias fluxes f_β and f_ϵ are changed to a new setting where the qubit remains at the symmetry point, and the coupling strength is increased to a value that can be controlled from the strong to the USC regime. The qubit Hamiltonian changes when tuning fluxes, so this process should be done faster than the evolving time of the qubit Hamiltonian to prevent the qubit state from evolving. Moreover, it should be faster than the relaxation rate.

- Stage 3: The qubit is kept at the same point for a delay time t_d, during which the qubit relaxes towards its ground state in the USC regime.

- Stage 4: The coupling is switched off very fast by moving the qubit to the initial weak coupling point in stage 1. The relaxation rate is suddenly reduced drastically, so the qubit state should be frozen.

- Stage 5: The qubit is adiabatically moved to an off-symmetry point for state readout by tuning f_ϵ only. During this step, the qubit energy eigenstates become flux like states. This process should be done slower than the evolving rate of qubit Hamiltonian, which is the qubit frequency, and it should be done faster than the relaxation rate to keep the information of qubit energy eigenstates.

- Stage 6: Readout pulses are sent to the feed line that is coupled to the readout resonator, and the qubit state is measured in the flux basis.

Stages 1-6 are repeated for variable duration of the delay time until the relaxation at the USC regime is confirmed to finish during the delay time, to obtain the relaxation curve and the relaxation time for each value of the coupling strength.

4.1.2 Dephasing measurement

Qubit dephasing in the USC regime is measured using a Ramsey experiment. Stages of the experiment and pulse sequences are shown in Fig 4.2. Compared to the stages of relaxation measurement, the processes of tuning coupling strengths and state measurements, as well as the requirements on the coupling strengths in these two stages are similar. Actions in each stage are as follows.

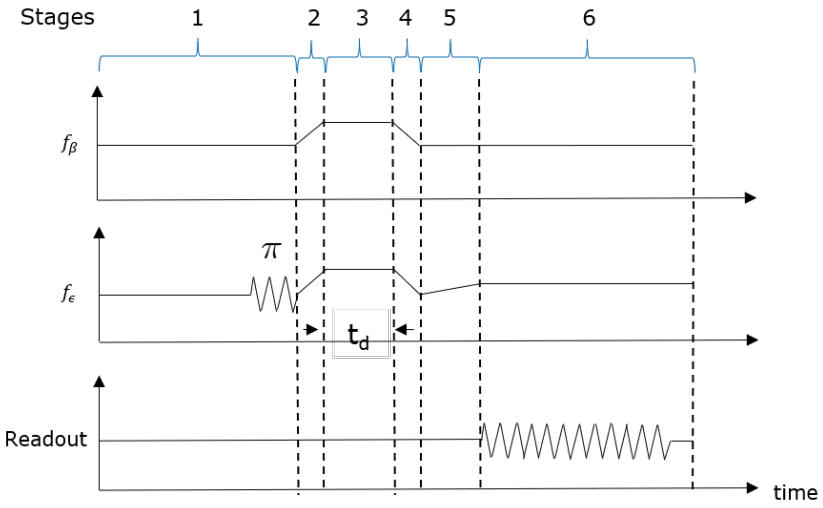

Figure 4.1: Pulse sequences of the flux pulses f_β and f_ϵ, and the readout signal for the relaxation measurement.

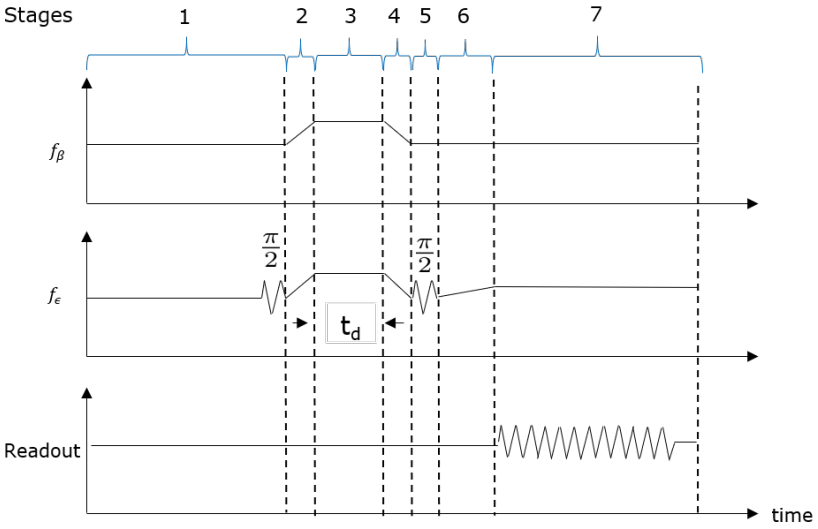

Figure 4.2: Pulse sequences of the flux pulses f_β and f_ϵ, and the readout signal for the dephasing measurement.

- Stage 1: The qubit is prepared in the ground state in the energy basis by waiting long enough at a symmetry point. The coupling to the transmission line is weak

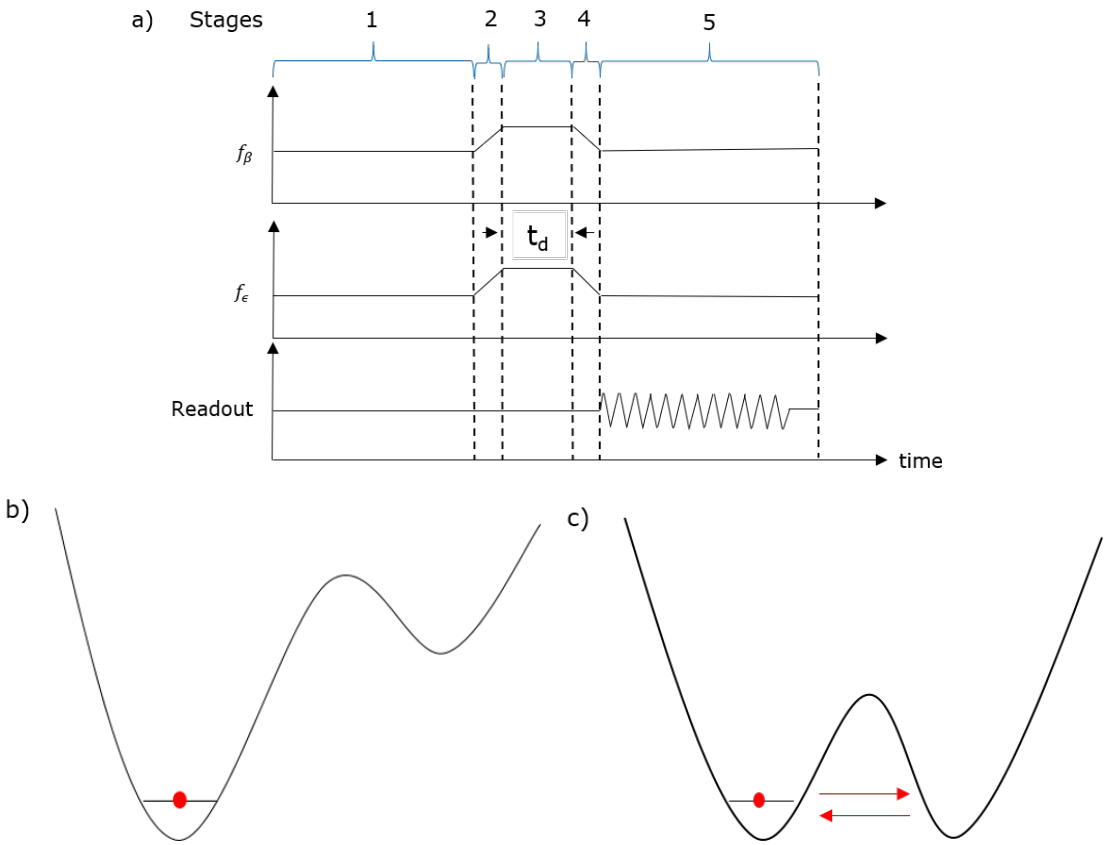

Figure 4.3: a) Pulse sequences of the flux pulses f_β and f_ϵ, and the readout signal for the experiment on the tunneling of flux states. b) The diagram of the double well potential when the qubit is away from the symmetry point and the qubit is in a flux state; c) The double well potential becomes symmetric when the qubit is at the symmetry point and the tunneling between two wells is enabled.

at this point, so the qubit is kept from relaxation. Then, a $\pi/2$ pulse is applied to the qubit main loop through f_ϵ to create a superposition state of the ground and the first excited state in the energy basis. To maintain the superposition state, both relaxation and dephasing rate at this point should be much larger than the length of the $\pi/2$ pulse.

- Stage 2: The f_ϵ and f_β are changed to increased the coupling strength into to the USC regime, while the qubit remains at the symmetry point. This process should be done very fast and non-adiabatically.

- Stage 3: The qubit is kept at the same point to allow it to interact with the environment in the USC regime for a delay time t_d. Dephasing is expected to occur in this process due to the interaction with the environment.
- Stage 4: The qubit is fast moved back to the weak coupling point in stage 1, so that the electromagnetic field in the waveguide is no longer a source of dephasing.
- Stage 5: The second $\pi/2$ pulse is applied to the qubit main loop through f_ϵ.
- Stage 6: The qubit is adiabatically moved to an off-symmetry point by changing f_ϵ only.
- Stage 7: Readout pulses are sent to the feed line, and the qubit state is measured in the flux basis.

Then, stage 1 to 7 are repeated for variable duration of the delay time until the dephasing at the USC regime is confirmed to finish during the delay time, to obtain the dephasing curve and the dephasing time for each value of the coupling strength.

4.1.3 Tunneling of flux states in the USC regime

The qubit frequency Δ, which is equivalent to the tunneling frequency between two flux states in the two potential wells, is renormalized due to strong correlations between qubit and environment. The renormalization causes the qubit frequency to decrease with increasing coupling strength, as introduced in Section 3.1.4. In this experiment, we are going to measure the tunneling frequency of flux states in the USC regime. The pulse sequences are shown in Fig 4.3a. The following is the detailed experimental protocol.

- Stage 1: The qubit is biased away from the symmetry point, where the bias between two wells is large. After waiting long enough time, the qubit settles to an energy eigenstate which is almost a flux state, which is localized in one potential well, as shown in Fig 4.3b. At this off-symmetry point, the qubit is decoupled from the transmission line.
- Stage 2: The qubit is fast and non-adiabatically brought to a point, which is a symmetry point and at which the coupling strength is in the USC regime. This has to be done faster than the evolving rate of the qubit Hamiltonian, and the qubit relaxation rate.

- Stage 3: The qubit is kept at the USC point for a delay time t_d. The potential diagram at this point is shown in Fig 4.3c. The tunneling between two flux states is enabled.
- Stage 4: The qubit is fast and non-adiabatically moved back to the off-symmetry point in stage 1 to quickly stop the tunneling.
- Stage 5: The qubit state is measured in flux basis by sending readout pulses to the readout feed line.

Stage 1 to 5 are repeated for variable duration of the delay time, to obtain the curve of the population of the flux state and extract the tunneling frequency for each value of the coupling strength.

4.2 Device design and modeling

This section introduces a superconducting device formed of an atom and a switchable coupler, which can be used to implement the experiments discussed in the previous section.

4.2.1 The first version of qubit design

In this section, we discuss the design used in [1], where the non-perturbative ultrastroung coupling is first demonstrated in superconducting circuits. The circuit model is shown in Fig 4.4. The qubit main loop contains four Josephson junctions and it is galvanically connected to an open transmission line. As shown in Eq 3.46 of Chapter 3, this type of coupling is via $\varphi_0\gamma_4 I_{rms}$, where $\varphi_0\gamma_4$ represents the flux generated by the shared arm of the qubit, and I_{rms} represents quantum fluctuations of current in the transmission line. The quantity $\varphi_0\gamma_4$ can be approximated as MI_p, where M is the mutual inductance between the qubit and the transmission line, and I_p is the persistent current of the qubit. The mutual inductance is dominated by the Josephson inductance of the shared junction, which is of the following form if the current flowing through the junction is much smaller than its critical current,

$$L_J = \frac{\Phi_0}{2\pi I_c}. \tag{4.1}$$

It can reach as big as 1 nH, so it is much larger than the geometric mutual inductance or the kinetic inductance of the shared piece of wire. Through the qualitative analysis, we can see the large Josephson inductance makes the ultrastrong coupling possible [30].

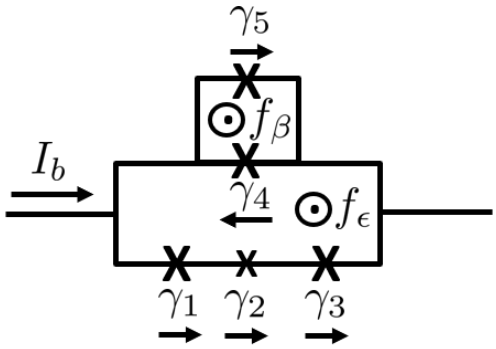

Figure 4.4: The circuit model of the first version of qubit design. The two-loops qubit has 4 junctions in the main loop (ϵ loop) and two junctions in the second loop (β loop). f_ϵ and f_β are fluxes in the corresponding loop. γ_i is the phase across junction i. The qubit is connected to the transmission line by sharing junction 4. I_b is the current in the transmission line.

To allow tunable coupling, Junction 4 is replaced with a SQUID. By tuning the flux in the SQUID, the effective size of junction 4 varies from $|r_4 - r_5|$ to $r_4 + r_5$, where $r4$ and r_5 represent the sizes of junction 4 and 5, so the Josephson inductance is in the range of $\frac{\Phi_0}{2\pi(I_{c4}+I_{c5})}$ to $\frac{\Phi_0}{2\pi|I_{c4}-I_{c5}|}$. The smallest coupling is obtained when $L_J = \frac{\Phi_0}{2\pi(I_{c4}+I_{c5})}$, but this cannot effectively decouple the qubit. During the process of optimizing the qubit design, we find that the junctions with extremely large critical currents are required to decouple the qubit from the transmission line, which is required for the experiments proposed in Section 4.1. In one design, the critical current has to reach 11 μA, but the shadow evaporation technique, as a typical fabrication method for Josephson junctions, fails to make junctions with such large critical currents. The largest coupling can be achieved when the Josephson inductance reaches its maximum value. At this point, since the critical currents are nearly cancelled, the qubit gap decreases drastically, which makes it difficult to optimize the qubit design. Therefore, we found a new design, which is going to be introduced in the next subsection.

4.2.2 Two-qubit coupler model

In this section, we discuss a tunable coupler for two qubits, which is going to be adapted to the coupler between qubit and transmission line. It is an effective method to use a third element to achieve tunable coupling between two qubits [31, 32, 33]. Figure 4.5a shows an example where two flux qubits are coupled via a rf-SQUID. The interaction can be

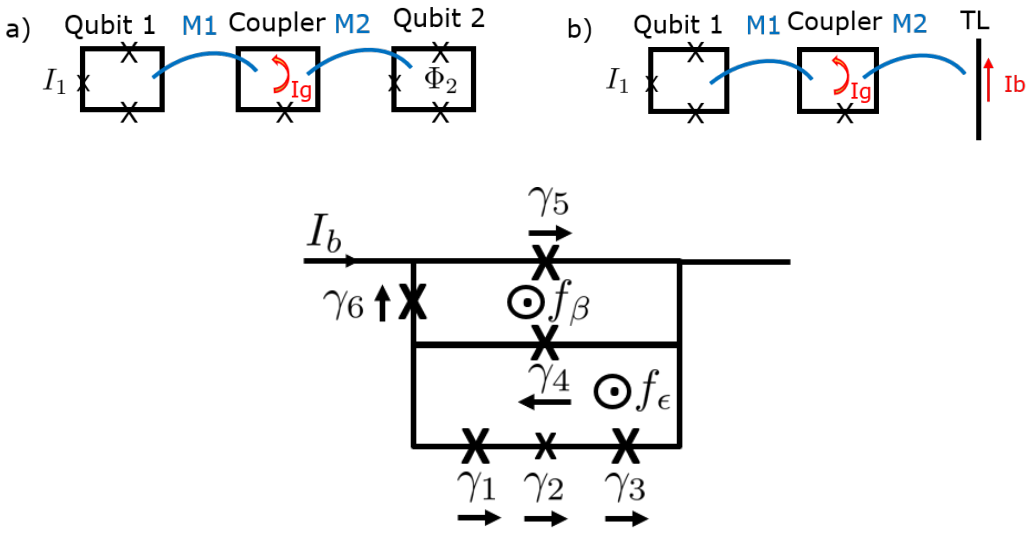

Figure 4.5: a) Circuit model of two qubits coupled by a rf-SQUID, with I_1 the current in qubit 1, I_g the current in the coupler, and Φ_2 the flux in qubit 2. M_1 (M_2) is the mutual inductance between the coupler and the qubit 1 (qubit 2). b) Circuit model of a qubit coupled to an open transmission line via an rf-SQUID, with I_b the current in the open transmission line. c) Circuit model of a two-loop qubit galvanically connected to an open transmission line. f_β and f_ϵ are fluxes in the two loops.

expressed as MI_1I_2, in which M is the effective mutual inductance between two qubits, and I_1 and I_2 are persistent currents in the corresponding qubit. The two-qubit interaction is mediated by the screening current of the coupler. The coupling arises in the following way. Qubit 1 induces a flux I_1M_1 in the coupler, where M_1 is the mutual inductance bewteen them. The rf-SQUID is considered as a non-linear inductance $L_{sq} = \frac{\partial I_g}{\partial \Phi_{ext}}$, where I_g is the ground state current, and Φ_{ext} is the external flux in the SQUID. The induced flux creates a sceening current $I = I_1M_1/L_{sq}$ in the coupler, which further induces a flux $\Phi_2 = \frac{I_1M_1M_2}{L_{sq}}$ in qubit 2. Therefore, the effective mutual inductance $M = \frac{M_1M_2}{L_{sq}}$. The rf-SQUID is treated as a passive element, such that it does not generate entanglement with qubits. Hence the energy gap of the rf-SQUID should be much larger than the qubit gaps to keep it in the ground state.

To implement this model in our tunable coupling system, the second qubit is replaced with an open transmission line, as illustrated in Fig 4.5b. Then, qubit 1 and the transmission line are galvaniacally connected to the coupler and sharing junction 4 and 5 respectively to enlarge the mutual inductance, as shown in Fig 4.5c. The coupler becomes

a persistent current flux qubit with three Josephson juncitons, and it is named as the β qubit. To show the tunability of the system, the qubit gap and the ground state current of the β qubit are simulated. Th goal of the simulation is to find an optimized qubit with a large qubit gap and a large maximum of $\frac{\partial I_g}{\partial \Phi_{ext}}$ by tuning the sizes of the three junctions and the critical current density that is shared by all junctions. For simplicity and as a convention for a persistent current flux qubit, the sizes of junction 4 and 5 are set to be the same. In the final design, the qubit gap is about 23 GHz, much larger than the gap of main qubit that is in the range of 1 to 12 GHz. The ground state current versus the external flux is shown in Fig 4.6, and we can see that the strongest coupling can be achieved at $f_\beta = 0.5$ where $\frac{\partial I_g}{\partial f_\beta}$ reaches its maximum, and the coupling can be switched off at around $f_\beta = 0.4$ or 0.6, where $\frac{\partial I_g}{\partial f_\beta} = 0$.

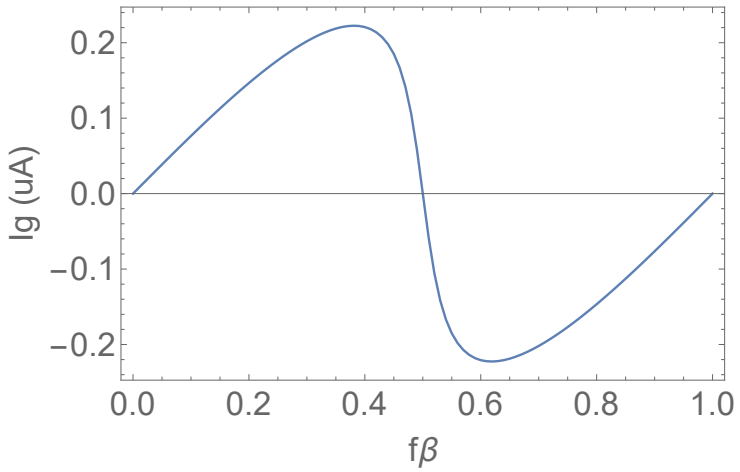

Figure 4.6: The ground state current I_g versus the external flux in the β qubit.

4.2.3 Qubit design and simulation

We need to complement the qualitative arguments from the previous section by complete calculations. In this section, the qubit with two loops is treated as a whole and the quantization of the tunable qubit and the simulations on qubit properties are discussed. The flux quantization relation in the two loops are

$$\gamma_1 + \gamma_2 + \gamma_3 + \gamma_4 + 2\pi f_\epsilon = 0, \tag{4.2}$$

$$\gamma_4 + \gamma_5 + \gamma_6 - 2\pi f_\beta = 0. \tag{4.3}$$

γ_i is the phase across junction i, and $f_\epsilon = \Phi_\epsilon/\Phi_0$ and $f_\beta = \Phi_\beta/\Phi_0$ represents the flux in qubit loops. The kinetic energy of the circuits is composed of energies stored in each junction capacitors. It can be written as

$$T = \frac{\varphi_0^2}{2}\dot{\boldsymbol{\gamma}}^T C \dot{\boldsymbol{\gamma}}, \tag{4.4}$$

in which

$$\dot{\boldsymbol{\gamma}} = \begin{pmatrix} \dot{\gamma}_1 \\ \dot{\gamma}_2 \\ \dot{\gamma}_4 \\ \dot{\gamma}_5 \end{pmatrix}, \tag{4.5}$$

and the capacitance matrix C is

$$C = \begin{pmatrix} C_1 + C_3 & C_3 & C_3 & 0 \\ C_3 & C_2 + C_3 & C_3 & 0 \\ C_3 & C_3 & C_3 + C_4 + C_6 & C_6 \\ 0 & 0 & C_6 & C_5 + C_6 \end{pmatrix}. \tag{4.6}$$

The C_i is the capacitance of junction i. The potential energy of the circuit is stored in each Josephson junctions.

$$\begin{aligned} U = &- \varphi_0[I_{c1}\cos\gamma_1 + I_{c2}\cos\gamma_2 + I_{c3}\cos(\gamma_1 + \gamma_2 + \gamma_4 + 2\pi f_\epsilon) \\ &+ I_{c4}\cos\gamma_4 + I_{c5}\cos\gamma_5 + I_{c6}\cos(\gamma_4 + \gamma_5 - 2\pi f_\beta)]. \end{aligned} \tag{4.7}$$

The I_{ci} in the above equation is the critical current of junction i. The Lagrangian of the system $\mathcal{L} = T - U$ is found to satisfy the Euler-Lagrangian equation

$$\frac{d}{dt}\left(\frac{\partial \mathcal{L}}{\partial \dot{\gamma}_i}\right) = \frac{\partial \mathcal{L}}{\partial \gamma_i}. \tag{4.8}$$

The conjugate momentum p_i is

$$p_i = \nabla_{\dot{\gamma}_i} T = \varphi_0^2 C \dot{\gamma}_i. \tag{4.9}$$

Then, the Hamiltonian can be obtained from the Legendre transformation $\mathcal{H} = \sum_i p_i \dot{\gamma}_i - \mathcal{L}$,

$$\mathcal{H} = \frac{1}{2\varphi_0^2}\boldsymbol{p}^T C^{-1}\boldsymbol{p} + U, \tag{4.10}$$

with

$$\boldsymbol{p} = \begin{pmatrix} p_1 \\ p_2 \\ p_4 \\ p_5 \end{pmatrix}. \tag{4.11}$$

To diagonalize the Hamiltonian, it is represented in the charge basis $|n\rangle$. The momentum vector p and the Josephson terms hence have these simple forms,

$$\boldsymbol{p} = \begin{pmatrix} p_1 \\ p_2 \\ p_4 \\ p_5 \end{pmatrix} = \hbar \begin{pmatrix} n_1 \\ n_2 \\ n_4 \\ n_5 \end{pmatrix}, \tag{4.12}$$

$$\cos\gamma|n\rangle = \frac{e^{i\gamma} + e^{-i\gamma}}{2}|n\rangle = \frac{|n+1\rangle + |n-1\rangle}{2}. \tag{4.13}$$

To restrict the Josephson term in a closed Hilbert subspace, each degree of freedom n_i has a restriction on its number of charges, which should be in the range of $-n_{i,max}$ to $n_{i,max}$. The Hamiltonian is then written in a matrix form by assigning

$$n_i = \begin{pmatrix} -n_{i,max} & & & & \\ & -n_{i,max}+1 & & & \\ & & \dots & & \\ & & & n_{i,max}-1 & \\ & & & & n_{i,max} \end{pmatrix}. \tag{4.14}$$

The Hamiltonian is diagonalized to obtain the qubit transition frequency E_{01}, anharmonicity E_{12}/E_{01}, and qubit eigenstates $|0\rangle$ and $|1\rangle$. The qubit relaxation rate to the open transmission line Γ_1 is estimated with Eq 3.56

$$\frac{\Gamma_1}{E_{01}} = \frac{\Delta^2}{E_{01}^2}\frac{1}{2\pi}\frac{R_Q}{Z_0}|\gamma_{\beta 10}|^2, \tag{4.15}$$

with Δ the transition frequency at the symmetry point, and $\gamma_{\beta 10} = \langle 1|\gamma_\beta|0\rangle$. We assume there is low frequency noise caused by current fluctuations in the transmission line (see Section 3.2), and estimate the pure dephasing rate Γ_φ with Eq 4.16

$$\Gamma_\varphi = \frac{E_{01}^2 - \Delta^2}{E_{01}^2}\frac{1}{2}|\gamma_{\beta 00} - \gamma_{\beta 11}|^2\frac{R_Q}{Z_0}\frac{k_B T}{h}. \tag{4.16}$$

In the charge basis, the phase operator is written as [1]

$$\langle n|\gamma_\beta|m\rangle = \frac{1}{2\pi}\int_{-\pi}^{\pi}\gamma_\beta e^{-i(m-n)\gamma_\beta}d\gamma_\beta = \begin{cases} 0 & \text{if } m=n, \\ -i\frac{(-1)^{(m-n)}}{m-n} & \text{if } m\neq n. \end{cases} \tag{4.17}$$

In simulations, the maximal charge numbers are set as $n_{1,max}=5$, $n_{2,max}=5$, $n_{4,max}=7$ and $n_{5,max}=7$. Under this setting, the qubit gap is confirmed to be convergent. The parameter space for optimizing the qubit design consists of the sizes of 6 junctions and a shared critical current density J_c. Such large parameter space makes the optimization process complicated and time-consuming. To simplify the process, we first optimize the β qubit to ensure its qubit gap and the maximum of $\frac{\partial I_g}{\partial \Phi_{ext}}$ is large, as discussed in Section 4.2.2, so that we can have restrictions on the sizes of junction 4, 5 and 6 as well as the critical current density. The sizes of junction 1 and 3 are set to be the same, as required for a persistent current flux qubit. The requirements for the qubit optimization are listed as follows:

- Qubit gaps should be in the range of 1 to 12 GHz, as limited by the bandwidth of our measurement setup.
- We need to find a point for preparing the initial state in the experiments of relaxation measurement. The point should be a symmetry point, and the relaxation time at the point should be much longer than the time needed for state preparations, which can be controlled within 10 ns. Thus, the relaxation time target is set in a safe range, more than 100 ns.
- We need to find a point for preparing the initial state in the experiments of dephasing measurement. The point should be a symmetry point, and both relaxation and dephasing time should be larger than the time needed to prepare a superposition state, which is in the scale of 10 ns. Therefore, both rates are required to be larger than 100 ns.
- We need to find a point, which is far away from the symmetry point and at which the double well potential is biased as shown in Fig 4.3b, so that the energy eigenstate at this point is almost a flux state, and the qubit can be prepared at a flux state at this point. This is required for the experiment on flux tunneling. Besides, this point can also be used for flux readout in all three experiment, so the relaxation time should be comparable or more than the state readout time, which is around 1 us. Moreover, the persistent current should be large enough to generate strong coupling to the readout SQUID.

- We need to find a list of points, which are symmetry points and at which the qubit is ultrastrongly coupled to the transmission line. This is required for all three experiments.

With these goals, the system properties are explored in the parameter space consisting of four junction sizes and the critical current density. In the final qubit design, $J_c = 4\mu\text{A}/\mu\text{m}^2$, the size of junction 1 and 3 is 0.047 μm^2, and the area ratio of other junctions to junction 1 are $r_2 = 0.7$, $r_4 = r_5 = 3.0$ and $r_6 = 1.32$.

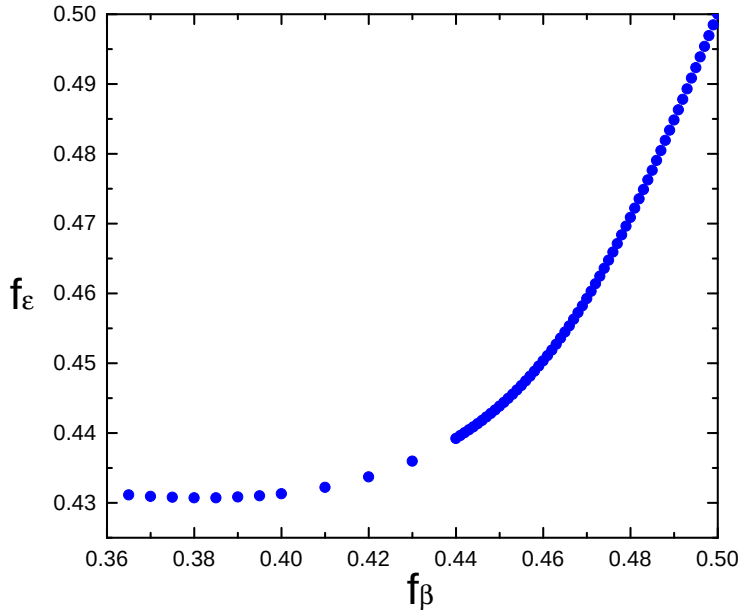

Figure 4.7: Diagram of positions of the symmetry points in the plane of f_β and f_ϵ.

The qubit symmetry point is defined as the flux bias point where qubit transition frequency reaches minimum. A single loop flux qubit is at the symmetry point when the external flux $f = \Phi_{ext}/\Phi_0$ equals to $0.5 + n$, where n is any non-negative integer. For a two-loop qubit, the symmetry point is no longer the point where the flux in the main loop f_ϵ equals to half of the flux quantum, since the flux in the second loop f_β shifts the symmetry point. In our case, for each f_β, we can find a f_ϵ that corresponds to a symmetry point. In simulations, the f_ϵ is swept from 0.4 to 0.6 for a list of f_β to find the points where the qubit gap is minimal, which are considered as the symmetry points. Figure 4.7 shows the positions of the set of symmetry points. Qubit properties and interaction strengths are calculated at this set of symmetry points, as shown in Fig 4.8, the qubit gap E_{01} is

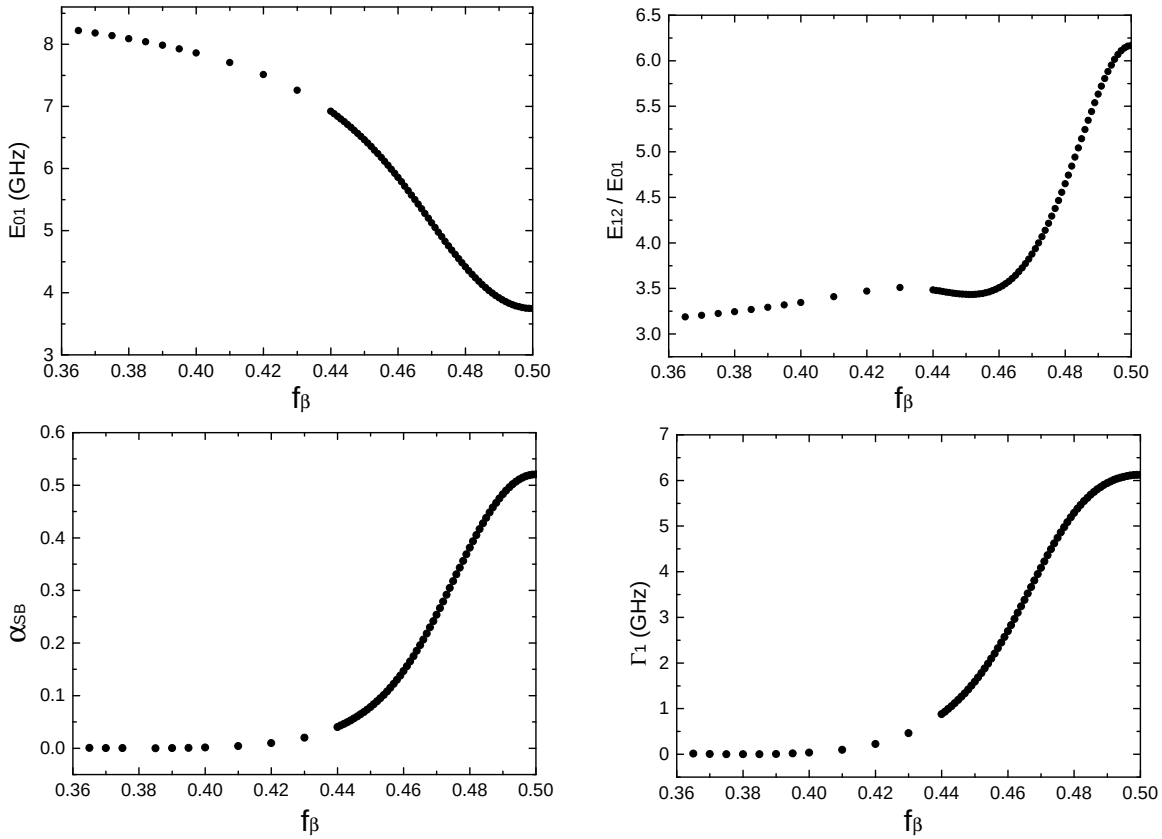

Figure 4.8: Diagram of qubit gap, anharmonicity, α_{SB}, relaxation rates Γ_1 over f_β.

from 3.74 to 8.22 GHz and the anharmonicity E_{12}/E_{01} is from 3.2 to 6.2. The coupling strength α_{SB} is in the range of $3.6 * 10^{-6}$ to 0.52, so the coupling strength can reach the USC regime, and even reaches the nonperturbative USC regime (see Section 3.1.1). The relaxation rate increases from 0.1 MHz to 6.12 GHz, and the dephasing rates vanishes at the symmetry points.

Next, we explain how the three experiments proposed in Section 4.1 can be implemented based on the simulation results. Figure 4.9 shows the positions of the qubit in the flux plane for several experiment stages. The blue points represents the set of symmetry points. When f_β ranges from 0.365 to 0.39, the relaxation rates are smaller than 10 MHz, so these points are considered as the weak coupling region. The point labeled by the green cross corresponds to the point with minimum relaxation rate $\Gamma_1 = 0.1$ MHz, so this point is considered as the decoupling point and is used for preperation of intitial states in the

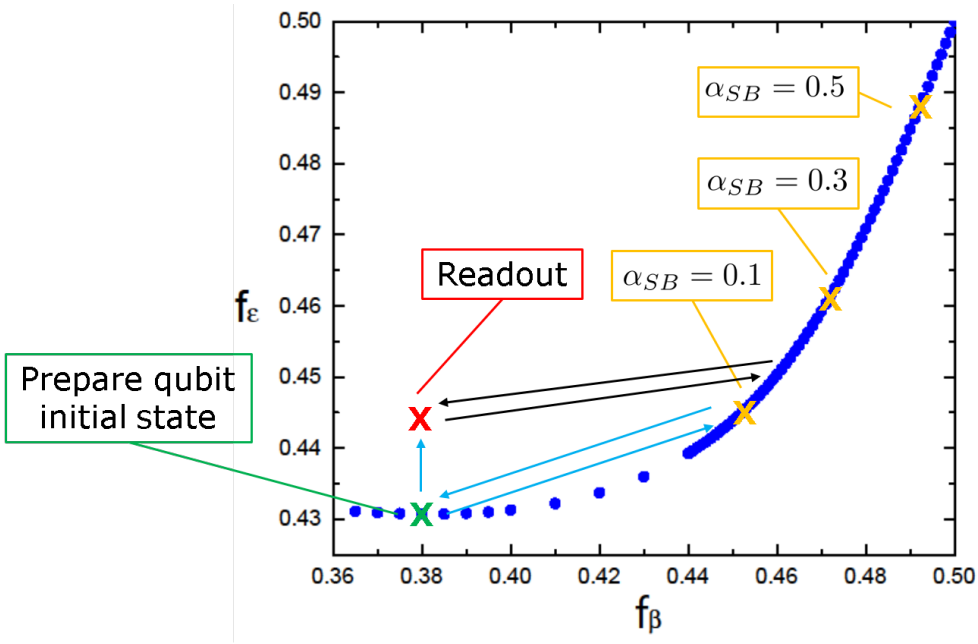

Figure 4.9: Illustration of experiment steps in the plane of f_β and f_ϵ.

relaxation and dephasing experiments. The coupling strengths keep increasing with f_β, and it enters into the USC regime when $f_\beta = 0.44$, where $\alpha_{SB} = 0.04$ and $\Gamma_1/E_{01} = 0.126$. The yellow crosses show the positions of $\alpha_{SB} = 0.1$, 0.3 and 0.5. The red cross represents the point for state readout, which is reached by increasing the f_ϵ by 15 mΦ_0 from the point of green cross, so that the qubit is away from the symmetry point. At this point, $E_{01} = 11.9$ GHz, $E_{12}/E_{01} = 2.0$, the persistent current $I_p = 100$ nA. The dephasing time $\Gamma_\varphi = 25$ μs and the relaxation time $T_1 = 2.5$ μs, as induced by the one-dimensional field, both of which are larger than the readout time $T_{\text{readout}} \approx 1$ μs.

In the experiment of relaxation measurement (see Section 4.1), the experiment steps are indicated by the light blue arrows in Fig 4.9.

- In stage 1, the qubit is prepared in the ground state at the green cross, which is a symmetry point, and the relaxation time at the point is about 2.5 μs, much longer than the relaxation time target 100ns. Then, it is excited to the first excited state by a π pulse.

- In stage 2, The qubit is fast and non-adiabatically moved to another symmetry point, where the coupling strength is in the USC regime. For example, it can be moved to

one of the yellow crosses.

- In stage 3, the qubit is kept at the same point to allow state evolution for a delay time.
- In stage 4, the qubit is fast and non-adiabatically moved back to the green cross to decouple the qubit and frozen the state.
- In stage 5, the qubit is adiabatically moved to the readout point labeled by the red cross. Qubit energy states evolve into flux states.
- In stage 6, at the red cross, qubit states are measured in the flux basis.

Then, all the stages are repeated while increasing the delay time. In the experiment of dephasing measurement, the experiment steps are very similar to the relaxation measurement and there are only two differences. The first is the qubit is applied with a $\pi/2$ pulse instead of a π pulse in stage 1. The second difference is there is one more step between stage 4 and 5. After the qubit is moved back to the green cross in stage 4, it needs to be applied with another $\pi/2$ pulse. Afterwards, it is moved to the red cross for state readout.

The steps of the experiment of the tunneling of flux states is shown by the black arrows.

- In stage 1, the qubit is prepared in a flux state at the red cross, which is far away from the symmetry point.
- Similar to the stage 2 in the relaxation measurement, the qubit is non-adiabatically moved to a symmetry point in the USC regime.
- In stage 3, the qubit is kept at the same position to allow the tunneling of flux states in USC regime for a delay time.
- In stage 4, the qubit is moved back to the red cross non-adiabatically.
- In stage 5, qubit states are measured at the red cross.

In the proposed experiments, we need to make sure that qubit states do not change significantly while we switch on or off the coupling, so the switching should be done faster than the qubit transition frequency and relaxation rates. The precise conditions have to be validated by further theory and experimental work.

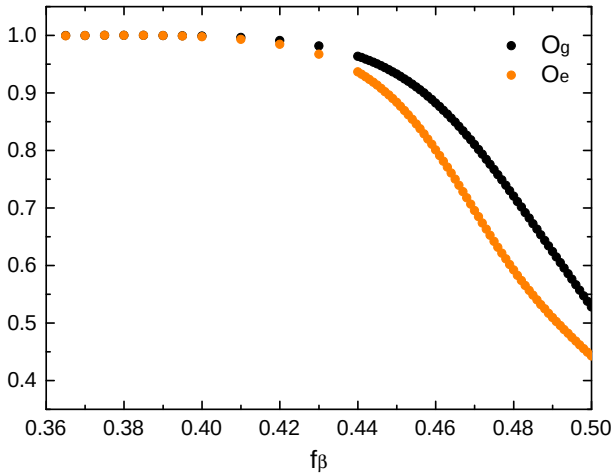

Figure 4.10: The overlap between the state at the weak coupling point and the states at all points.

In all three experiments, the initial qubit states are prepared at the decoupling point, then it is moved to the USC points which allows the evolution of the qubit state. Afterwards, it is moved back for state readout. It is important that the states at the USC points should be in the subspace spanned by the ground and excited states at the decoupling point and do not involve any higher states. The overlaps between the state at the green cross and the states at all the blue points in Fig 4.9 are shown in Fig 4.10. The states overlap O_g and O_e are

$$O_g = |\langle g|g_{wc}\rangle|^2 + |\langle e|g_{wc}\rangle|^2, \tag{4.18}$$

$$O_e = |\langle g|e_{wc}\rangle|^2 + |\langle e|e_{wc}\rangle|^2, \tag{4.19}$$

where g_{wc} and e_{wc} are the ground and the excited state at the weak coupling point, and g and e are states at points with various coupling strengths. The overlaps at several coupling strengths are listed out in table 4.2, which indicates the states overlap is still good when coupling strength is in the USC regime.

α_{SB}	0.04	0.1	0.3	0.5
O_g	0.96	0.92	0.78	0.60
O_e	0.94	0.85	0.65	0.49

Table 4.1: State overlaps between the decoupling point and several points with different coupling strengths.

Γ_1/E_{01}	0.13	0.30	0.52	1.0
O_g	0.96	0.92	0.87	0.77
O_e	0.94	0.86	0.78	0.64

Table 4.2: State overlaps between the decoupling point and several points with different coupling strengths.

4.2.4 Flux biasing and driving

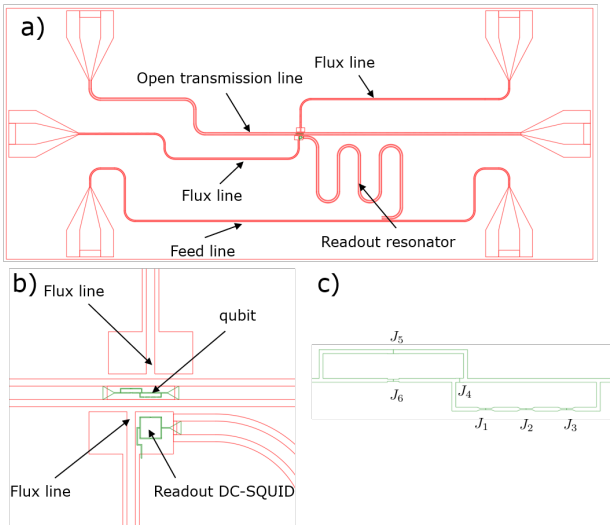

Figure 4.11: a) The full device design drawn in CAD. b) Zoom into the area around the qubit. c) Enlarged picture of the qubit design.

The design of the tunable qubit requires independent control of fluxes in two loops, so in total two flux lines are added to the device. The full device design is drawn in AutoCAD and it is shown in Fig 4.11. The flux line is made with a transmission line, which is divided into two branches at the end and then connect to the ground plane that is located at the two sides of the transmission line. The bottom flux line is inductively coupled to the ϵ loop. The center line of it points to the center of the β loop, such that the mutual inductance between them is close to 0. A similar configuration is used for the other flux line. Both DC signal and fast pulses are sent into the lines to control fluxes, but for different purposes. The DC signal is to induce a flux in the corresponding qubit loop for static bias, while the fast pulses are for qubit driving or fast tuning of flux.

The mutual inductance between qubit loops and the corresponding flux line should be in an optimized range. It should be kept small to prevent it from inducing large decoherence of the qubit, but it can not be too small, otherwise the required currents for flux biasing would be too large. As mentioned in Section 4.2.3, the qubit is designed to be biased around 0.45 Φ_0 for both f_ϵ and f_β. The mutual inductance between the ϵ loop and the bottom flux line is about 1 pH, so the required DC is 0.9 mA. The mutual inductance for the β loop is slightly smaller due to the smaller loop size, and the DC is required to reach 1.3 mA. To fast move the qubit from the weak coupling point to the USC points, the required current amplitude to generate fast pulses is in the range of hundreds of μA. These currents are small enough, so that they do not generate too much heat that increases the environmental noise leading to qubit decoherence.

Besides biasing, the bottom flux line is also used for inductive driving. The driving Hamiltonian is

$$H_d(t) = \frac{\partial H}{\partial \Phi_\epsilon}\Phi_{d0}\cos(\omega_d t + \varphi_d), \tag{4.20}$$

$$\frac{\partial H}{\partial f_\epsilon} = 2\pi\varphi_0 I_{c3}\sin(\gamma_{12} + \gamma_{23} - \gamma_{15} - \gamma_{54} + 2\pi f_\beta + 2\pi f_\epsilon), \tag{4.21}$$

where Φ_{d0} is the amplitude of driving flux and ω_d is the driving frequency. The Rabi frequency for driving the qubit from the ground state to the first excited state is

$$\omega_{R,01} = \Phi_{d0}\left|\langle g|\frac{\partial H}{\partial f_\epsilon}|e\rangle\right|. \tag{4.22}$$

When $\Phi_{d0} = 0.003\Phi_0$, the Rabi strength is calculated to be 900 MHz, so the length of a π pulse is around 1.1 ns, which is much smaller than the relaxation time of qubit at the state preparation point.

Since the flux lines are inductively coupled to the qubit, we are going to estimate the rate of qubit relaxation due to them. The qubit relaxation rate can be written as [34]

$$\Gamma_1 = 2\sin^2\theta\left(\frac{MI_p}{\phi_0}\right)^2\frac{R_Q}{Z_0}f_{qb}, \tag{4.23}$$

where $\tan\theta = \Delta/\epsilon$, and M is the mutual inductance, and I_p is the persistent current of qubit, and R_Q is the quantum resistance. Setting $I_p = 110$ nA, $M = 1$ pH and $f_{qb} = 12$ GHz, the relaxation rate reaches the maximum 87 KHz at the symmetry point. The pure dephasing rate is given by [34]

$$\Gamma_\phi = 2\cos^2\theta\left(\frac{MI_p}{\phi_0}\right)^2\frac{R_Q}{Z_0}\frac{k_B T}{h}. \tag{4.24}$$

The fridge temperature is normally around 30 mK, but in general terms higher noise temperatures are observed in some experiments. Assuming the noise temperature T reaches 100 mK, the largest dephasing time is reached at away from the symmetry point and it is about 65 us. Both relaxation and dephasing time is relatively large, so the decoherence rates due to flux lines do not dominate the rates induced by the open transmission line.

4.2.5 Flux readout

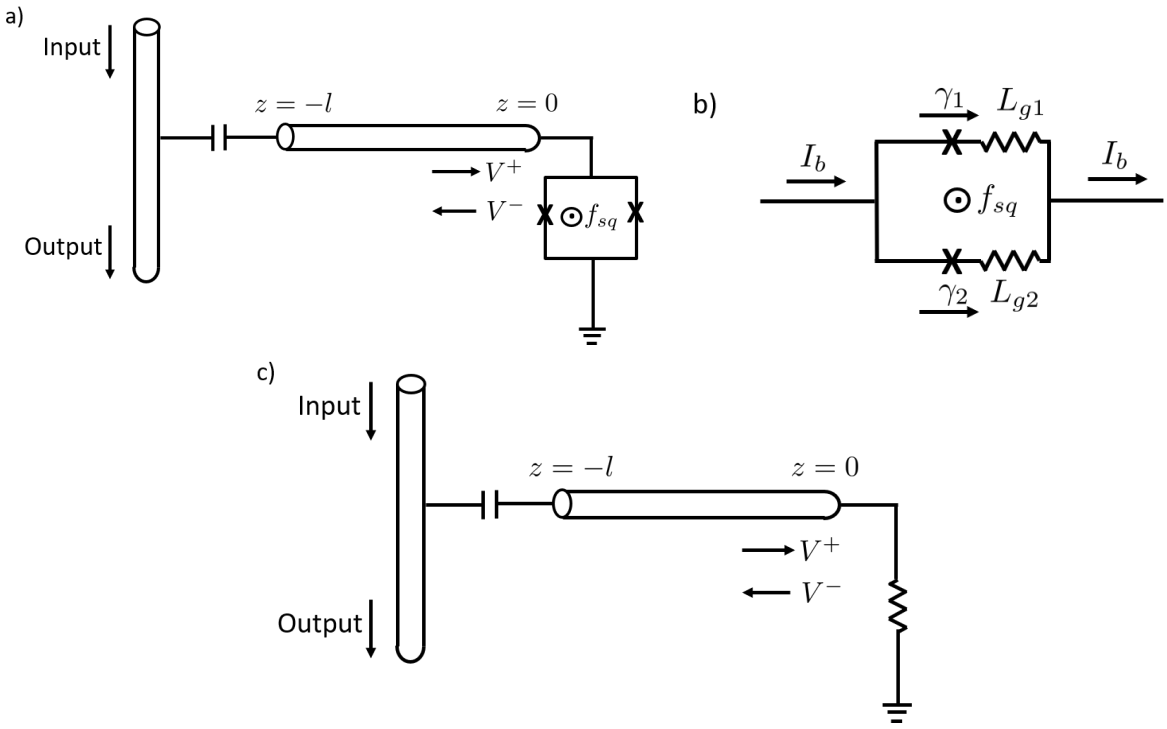

Figure 4.12: a) Circuit model of the readout resonator; b) Circuit model of a DC-SQUID; c) Circuit model of the readout resonator with the SQUID replaced with an ideal inductor.

As mentioned in the Section 4.1, qubit states are measured in the flux basis for all the three experiments. In this section, we are going to discuss the details of the flux readout circuit. The readout circuit is composed of a resonator, which consists of a transmission line that is capacitively coupled to a feed line on one end and is shorted to the ground via a DC-SQUID on the other end, as shown in Fig 4.11.

The DC-SQUID can be considered as an non-linear inductance. Next, we present how to determine the effecive inductance of the squid. The circuit model of a DC-SQUID is shown in Fig 4.12a. If taking the self geometric inductance into account, the phase relation can be written as

$$\gamma_2 - \gamma_1 = -2\pi f_{sq}, \tag{4.25}$$

where γ_1 and γ_2 are phases across junctions, $f_{sq} = \Phi_{sq}/\Phi_0$ represents the external flux. The current relations are

$$I_b = I_{c1} \sin\gamma_1 + I_{c2} \sin\gamma_2, \tag{4.26}$$

where $I_{c1,2}$ are the critical currents of two junctions, so the bias current is the sum of the currents in two branches. For given I_b and f_{sq}, there are multiple combinations of γ_1 and γ_2 that satisfy Eq. 4.25 and Eq. 4.26, but some solutions may not keep the SQUID in a stable state. We then look for solutions which minimize the potential energy of the SQUID,

$$\begin{aligned} U =& \varphi_0(I_{c1}+I_{c2})(-\cos\frac{\gamma_1+\gamma_2}{2}\cos\frac{\gamma_1-\gamma_2}{2}) - i_b\frac{\gamma_1+\gamma_2}{2} + \beta(\frac{\gamma_1-\gamma_2}{2} - \pi f_{sq})^2 \\ & - \alpha\sin\frac{\gamma_1+\gamma_2}{2}\sin\frac{\gamma_1-\gamma_2}{2} - \eta i_b\frac{\gamma_1-\gamma_2}{2}), \end{aligned} \tag{4.27}$$

where

$$\begin{aligned} \beta &= \frac{2\varphi_0}{(L_{g1}+L_{g2}-2M_a-M_q^2/L_q)(I_{c1}I_{c2})} \\ \alpha &= \frac{I_{c1}-I_{c2}}{I_{c1}+I_{c2}} \\ \eta &= \frac{L_{g2}-L_{g1}}{(L_{g1}+L_{g2}-2M_a-M_q^2/L_q)} \\ i_b &= \frac{I_b}{I_{c1}+I_{c2}}. \end{aligned} \tag{4.28}$$

The $L_{g1,2}$ are self inductances of the two branches of the SQUID. The DC-SQUID can be treated as an inductor and I_b is the current passing through it. Its effective inductance equals to the derivative of the induced flux with respect to I_b, which can be estimated as

$$L_{sq} = \varphi_0\frac{\gamma_1(I_b+\delta I_b) - \gamma_1(I_b)}{\delta I_b}. \tag{4.29}$$

$\gamma_1(I_b+\delta I_b)$ and $\gamma_1(I_b)$ are solutions of minimizing the SQUID potential energy with bias current $I_b+\delta I_b$ and I_b.

Next, we present how to determine the modes of the resonator, which will be quantized later. By assuming the DC-SQUID as an ideal inductor with inductance L_{sq}, the circuit

model of the readout resonator is simplified as shown in Fig 4.12b. The relation between the reflection coefficient and the forward and backward voltages at position $z = 0$ is

$$\frac{V^-}{V^+} = \Gamma = \frac{i\omega L_{sq} - Z_0}{i\omega L_{sq} + Z_0}, \tag{4.30}$$

where ω is the frequency of the microwave. Since the resonator is ended with a capacitor on the other end, the current at $z = -l$ is 0 at resonance,

$$I(z = -l) = \frac{1}{Z_0}(V^+_{z=-l} - V^-_{z=-l}) = 0. \tag{4.31}$$

The forward and backward voltages at position z are $V^+_z = V^+ e^{-ikz}$ and $V^-_z = V^- e^{-ik(-z)}$, where k is the wavenumber. By substituting them into Eq 4.31 and use Eq 4.30, we have

$$\frac{V^+}{Z_0}(e^{ikl} - \Gamma e^{-ikl}) = 0. \tag{4.32}$$

The wavenumber equals to the ratio of angular frequency ω to the phase velocity c, $k = \frac{\omega}{c}$, then the above equation becomes

$$\frac{V^+}{Z_0}(e^{i\omega l/c} - \Gamma e^{-i\omega l/c}) = 0, \tag{4.33}$$

where $c = \frac{1}{\sqrt{\tilde{C}\tilde{L}}}$ and $\tilde{C}$ and $\tilde{L}$ are capacitance and inductance per unit length of the transmission line. Substitute Γ with Eq 4.30 and then simplifying it, the above equation can be written as

$$e^{i\omega l/c} - \frac{i\omega L_{sq} - Z_0}{i\omega L_{sq} + Z_0} e^{-i\omega l/c} = 0. \tag{4.34}$$

The resonant frequency can be obtained by solving Eq 4.34.

The resonant frequency depends on the effective inductance of the DC-SQUID, which can be tuned by the external flux. Since the external flux consists of a bias flux and an induced flux from qubit, which depends on the qubit states, the two qubit persistent current states can be distinguished by the resonant frequencies. Fig 4.13 shows the dependence of the resonant frequency on the external flux for one design. Resonance frequency is chosen to be 4 GHz at $f_{sq} = 0.421$. The largest induced flux is

$$f_{\text{induced}} = |I_e - I_g|M, \tag{4.35}$$

where $|I_{g,e}| \approx 110$ nA are the persistent currents when qubit is in the ground and the excited state at the readout point and they have opposite signs. M is the mutual inductance

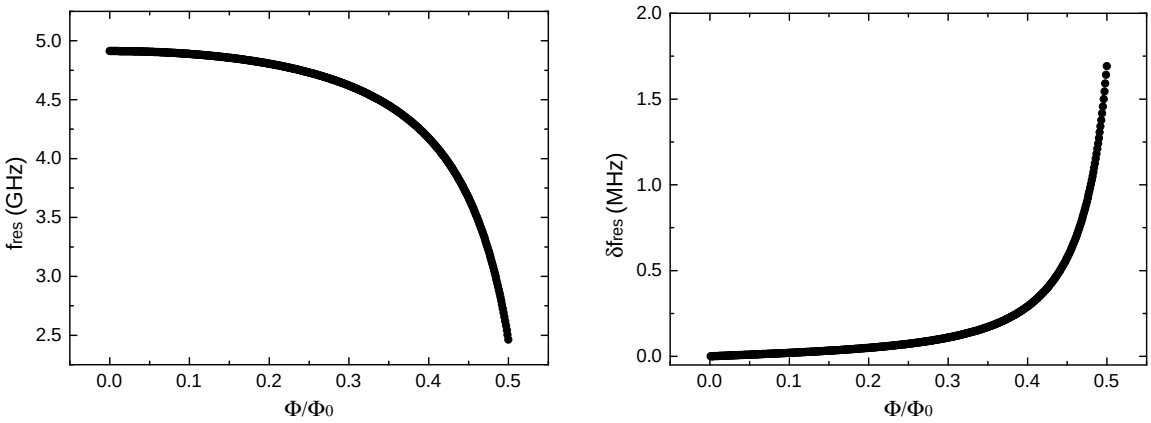

Figure 4.13: The two graphs show the simulated resonant frequencies (left) and the variation of the resonant frequency (right) caused by the change of qubit states versus the external flux in the SQUID.

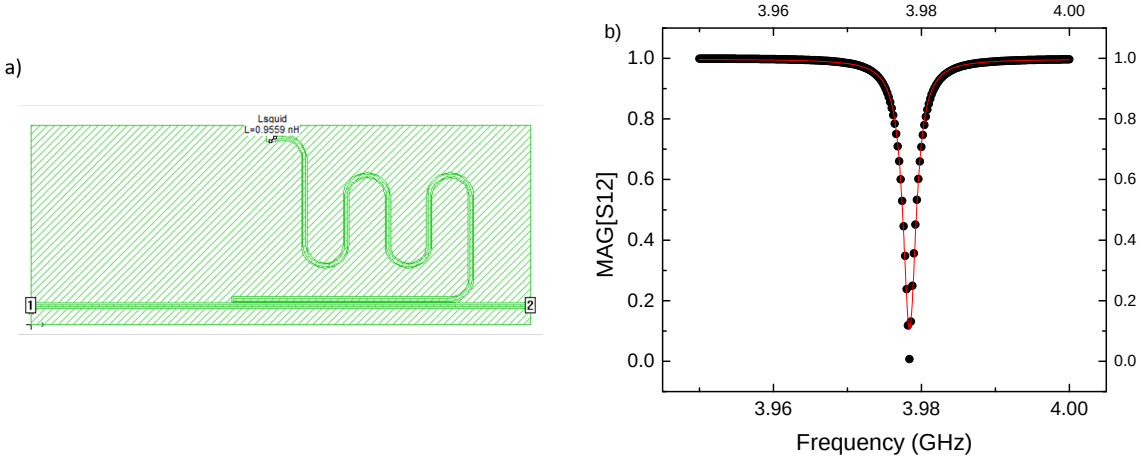

Figure 4.14: a) Circuit model in Sonnet. b) Lorentz fit of simulated S21 from Sonnet.

between qubit main loop and the DC-SQUID. The variations of resonant frequencies over a full range of external flux are evaluated based on Fig 4.13, which is shown in Fig 4.13. When choosing resonant frequency as 4 GHz, the variantion is 0.47 MHz.

Besides the resonant frequency, quality factor Q is another important parameter of a resonator, which describes how underdamped an oscillating system is. It is defined as the ratio of the resonant frequency to the half-power bandwidth i.e. the frequency range at which the vibration power is larger than half of the maximum power. The response time

of a resonator indicates the time it takes to pump photons into the resonator, and it is related to the quality factor,

$$T_{\text{response}} = \frac{Q}{\omega_{\text{res}}}. \tag{4.36}$$

During measurements of qubit states, it is required that the response time is smaller than the relaxation time of the qubit, otherwise the qubit has already relaxed to the ground state before the readout signal being pumped into the resonator. At the readout point, the relaxation time is restricted to be larger than 100 ns, so the quality factor needs to be smaller than 2513 with $\omega_{\text{res}} = 2\pi * 4$ GHz. The readout resonator is capacitively coupled to a feed line by having part of the transmission line parallel and close to the feedline. The transmission of microwaves in the feed line is simulated in the Sonnet suites of high-frequency electromagnetic (EM) Software. Figure 4.14a shows the circuit model in Sonnet, where the DC-SQUID is replaced with an ideal inductor. Port 1 and 2 are placed at two ends of the feed line, and S_{12} is simulated over a range of frequencies. Figure 4.14b shows the diagram of S_{12} over frequencies close to 4 GHz. The curve is fitted with Lorentz function and Q is found to be 2055. The half power bandwidth is 2 MHz, so the variation of resonant frequency is comparable to the bandwidth, which is critical for distinguishing the signals corresponding to the different qubit states.

Since the readout resonator is coupled to the qubit, we need to estimate the coupling strength between them to ensure that the readout circuit is not a significant decoherence source of the qubit. The interaction is expressed as $M_{\text{eff}} I_b I_{qb}$, where M_{eff} denotes the effective mutual inductance between the SQUID and the qubit main loop, I_b is the current going through the SQUID and I_{qb} is the current in the qubit. The M_{eff} equals to the derivative of the induced flux from SQUID to qubit with respect to I_b, which is estimated as

$$M_{\text{eff}} = \frac{\Phi_{sq-qb}(I_b + \delta I_b) - \Phi_{sq-qb}(I_b)}{\delta I_b}\Big|_{I_b=0}. \tag{4.37}$$

Φ_{sq-qb} is the sum of the induced fluxes from the two branches of the SQUID,

$$\Phi_{sq-qb}(I_b) = M_1 I_{c1} \sin\gamma_1(I_b) + M_2 I_{c2} \sin\gamma_2(I_b), \tag{4.38}$$

where M_1 and M_2 are mutual inductances between the qubit main loop and the two SQUID branches respectively, and $\gamma_{1,2}(I_b)$ is the phase of junction 1 or 2, which is found by minimizing the SQUID potential energy. Φ_{sq-qb} is distributed into two parts because M_1 and M_2 are very different in our design. The induced fluxes over a range of I_b is shown in Fig 4.15, and M_{eff} is calculated to be 0.686 pH.

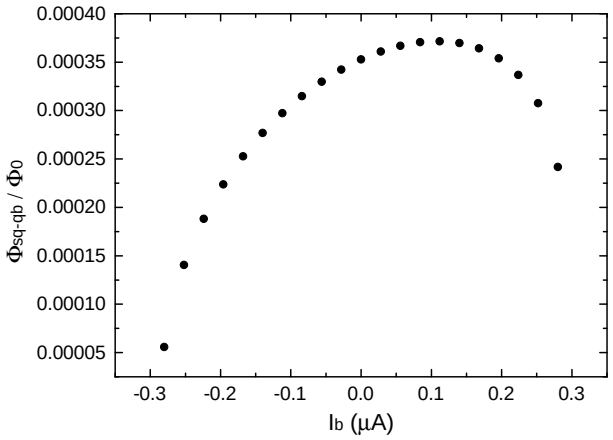

Figure 4.15: Induced fluxes from the DC-SQUID to the qubit versus the bias current.

Next, the process of the quantization of the readout resonator is introduced in order to find the expression of I_b. V^+ and V^- are dynamical variables and can be written as

$$V^+ = \overline{V^+} e^{i\omega t}, \tag{4.39}$$

$$V^{+*} = \overline{V^{+*}} e^{i\omega t}. \tag{4.40}$$

The energy of the system contains the magnetic and electric energy of the transmission line, and the magnetic energy of the effective inductor. The electric energy of transmission line is

$$E_e = \frac{1}{2}\tilde{C}\int_{-l}^{0} \tilde{V}(z)^2 dz. \tag{4.41}$$

$\tilde{V}(z)$ is the real part of the voltage $V(z) = V_z^+ + V_z^-$ in the transmission line,

$$\begin{aligned} \tilde{V}(z) &= \frac{1}{2}(V(z) + V^*(z)) \\ &= \frac{1}{2}[V^+(e^{-ikz} + \Gamma e^{ikz}) + V^{+*}(e^{ikz} + \Gamma^* e^{-ikz})]. \end{aligned} \tag{4.42}$$

The magnetic energy of the transmission line is

$$E_m = \frac{1}{2}\tilde{L}\int_{-l}^{0} \tilde{I}(z)^2 dz. \tag{4.43}$$

$\tilde{I}$ is the real part of the current,

$$\begin{aligned}\tilde{I}(z) &= \frac{1}{2}(I(z) + I^*(z)) \\ &= \frac{1}{2Z_0}[V^+(e^{-ikz} - \Gamma e^{ikz}) + V^{+*}(e^{ikz} - \Gamma^* e^{-ikz})].\end{aligned} \tag{4.44}$$

The energy in the effective inductor is

$$E_L = \frac{1}{2}L\tilde{I}(0)^2. \tag{4.45}$$

Then, the total energy of the system is

$$E_{\text{tot}} = \begin{pmatrix} V^+ & V^{+*} \end{pmatrix} \begin{pmatrix} 0 & \frac{1}{2}(\frac{l}{cZ_0} + \frac{L}{Z_0^2+L^2\omega^2}) \\ \frac{1}{2}(\frac{l}{cZ_0} + \frac{L}{Z_0^2+L^2\omega^2}) & 0 \end{pmatrix} \begin{pmatrix} V^+ \\ V^{+*} \end{pmatrix}. \tag{4.46}$$

In order to build the correspondence between classical variables and quantum operators, we try to find two variables $q = \kappa V^+ + \kappa^* V^{+*}$ and $p = i\omega\kappa V^+ - i\omega\kappa^* V^{+*}$, such that

$$E_{\text{tot}} = \begin{pmatrix} q & p \end{pmatrix} \begin{pmatrix} \frac{1}{2}\omega^2 & 0 \\ 0 & \frac{1}{2} \end{pmatrix} \begin{pmatrix} q \\ p \end{pmatrix}. \tag{4.47}$$

Comparing Eq 4.46 and Eq 4.47, we have

$$E_{\text{tot}} = \begin{pmatrix} q & p \end{pmatrix} \begin{pmatrix} \frac{\frac{l}{cZ_0} + \frac{L}{Z_0^2+L^2\omega^2}}{4\kappa\kappa^*} & 0 \\ 0 & \frac{\frac{l}{cZ_0} + \frac{L}{Z_0^2+L^2\omega^2}}{4\kappa\kappa^*\omega^2} \end{pmatrix} \begin{pmatrix} q \\ p \end{pmatrix}. \tag{4.48}$$

From Eq 4.47 and Eq 4.48, the magnitude of κ can be found. It is shown that p and q can obey the Hamilton's equation,

$$\begin{aligned}\frac{dp}{dt} &= -\omega^2\kappa V^+ - \omega^2\kappa^* V^{+*} \\ &= -\omega^2 q \\ &= -\frac{dH}{dq},\end{aligned} \tag{4.49}$$

$$\begin{aligned}\frac{dq}{dt} &= -i\omega\kappa V^+ - i\omega\kappa^* V^{+*} \\ &= -\omega^2 p \\ &= -\frac{dH}{dp},\end{aligned} \tag{4.50}$$

where Eq 4.39 and Eq 4.40 are used. Then, the system energy can be described by the harmonic oscillator Hamiltonian $H = \hbar\omega(a^\dagger a + 1/2)$ by writing p and q in terms of the ladder operators

$$\hat{p} = i\sqrt{\frac{\hbar\omega}{2}}(a^\dagger - a), \tag{4.51}$$

$$\hat{q} = i\sqrt{\frac{\hbar}{2\omega}}(a^\dagger + a). \tag{4.52}$$

At last, the current I_b going into the effective inductor is

$$I_b = \frac{i(a^\dagger - a)\sqrt{c\hbar\omega Z_0}}{\sqrt{cLZ_0 + l(L^2\omega^2 + Z_0^2)}}, \tag{4.53}$$

by assigning the phase of κ such that $\kappa^\dagger = \kappa/\Gamma$. The Hamiltonian of the system in the persistent current basis can be given as

$$\begin{aligned} H &= H_{\text{qb}} + H_{\text{resonator}} + H_{\text{int}} \\ &= -\frac{1}{2}\epsilon\sigma_z - \frac{1}{2}\Delta\sigma_x + \hbar\omega(a^\dagger a + \frac{1}{2}) + ig\sigma_z(a^\dagger - a), \end{aligned} \tag{4.54}$$

with the coupling strength $g = \frac{\Delta}{\sqrt{\Delta^2+\epsilon^2}}g'$. Since the interaction is via $M_{\text{eff}}I_{qb}I_b$, we find $g' = \frac{M_{\text{eff}}|\langle 0|I_{qb}|1\rangle|I_b}{i(a^\dagger - a)}$, where $|0\rangle$ and $|1\rangle$ are qubit ground and exited state in the eigenenergy basis. The Purcell lifetime of the qubit is related to the coupling strength by

$$T_{\text{purcell}} = \frac{Q}{2\pi f_{\text{res}}}(\frac{\delta}{g})^2, \tag{4.55}$$

where δ is the qubit-resonator detuning. To prevent the readout resonator from becoming a main decoherence source, the Purcell lifetime should be larger than the qubit relaxation time to the open transmission line, which is kept larger than 100 ns. Assuming the qubit is at the symmetry point $\epsilon = 0$ and $\langle 0|I_{qb}|1\rangle$ reaches the maximum value 110 nA, which is the persistent current when qubit is far away from the symmetry point, we find the minimum Purcell lifetime to be around 40 μs with the detuning $\delta = 0.1$ GHz. Therefore, the coupling between qubit and readout resonator is in a safe regime.

4.3 Summary

In this chapter, we present a novel design of the flux qubit with fast-switchable coupling to an open transmission line. The maximum coupling strength can reach the nonperturbative

ultrastrong coupling regime. We present the full device design consisting of the tunable qubit, the open transmission line, qubit flux bias lines, qubit drive lines and the readout copalanar waveguide resonator. It is demonstrated that this device can be used to perform three proposed experiments. The objective of the experiments is to study the interesting dynamics of the spin-boson model in the ultrastrong coupling regime. The three experiments are to measure qubit relaxation, dephasing and renormalized tunneling frequencies in the USC regime. Detailed experiment steps and pulse sequences are presented.

Chapter 5

Capacitively shunted flux qubit

The objective of the project covered in this chapter is to further explore the parameter space of flux qubits and address combined high coherence and large anharmonicity. In our design, we use three capacitive pads to shunt all the three junctions of a flux qubit, so the electric fields on all junctions are redistributed to capacitive pads. Compared to the single-shunt CSFQ, our design uniformly shunts all junctions, so it has smaller dielectric loss in junctions and further reduced charging energies. The flux qubit is capacitively coupled to a $\lambda/2$ coplanar waveguide (CPW) resonator for dispersive readout [9], and the qubit control is done with a capacitively coupled drive line. A global magnetic field is applied to the whole device to provide flux bias to the qubit. The circuits are modeled with a full capacitance matrix model that is introduced in section 5.1. The fabrication of the superconducting circuits is a three-layer process and is introduced in section 5.2. The device is mounted in the dilution refrigerator and operated at the temperature of around 27 mk. The experiment results and data analysis are discussed in section 5.3. The qubit spectroscopy shows an excellent match to the predictions of the capacitive matrix model. The experiment shows that the sample has large anharmonicity at the qubit symmetry point reaching $2\pi \times 3.69$ GHz and the relaxation time reaches $T_1 = 47$ μs. As for dephasing, the spin-echo dephasing time is $T_{2E} = 9.4$ μs, and we performed dynamical decoupling method with the Carr-Purcell-Meiboom-Gill (CPMG) method. The coherence time obtained by applying 100 CPMG pulses reaches 26.5 μs. Benefiting from the large anharmonicity, we are able to perform precise quantum control in the qutrit space consisting of the lowest three levels. The experiments of qutrit state tomography and multilevel coherence are presented. Al last, a summary of the project is given in section 5.4.

This project was mainly conducted by Dr. Muhammet Ali Yurtalan and was supervised

by Prof. Adrian Lupascu. My contribution to the project includes the fabrication of the superconducting device, working on measurement experiments and data analysis with Ali. I specifically worked on the experiments of qutrit tomography and multilevel coherence.

5.1 Circuit design and model

The circuit design and model of the CSFQ device are shown in Fig 5.1. Due to the large-size shunting pads of the qubit, the capacitances between these pads and adjacent circuits are much larger than the junction capacitances. Thus, beside the electric energies stored in the junction capacitances, the circuit model should also takes the energy stored in the capacitances between qubit shunting pads, CPW center line, control line and the ground plane into consideration, which is different from the model for typical flux qubit introduced in section 2.2, where only junction capacitances are considered. Therefore the circuit model is called the full capacitance matrix model. In the model, the resonator and drive line is consider to contribute to the gate voltages and gate capacitances to the qubit. The gate charges are also used to simulate charge fluctuations in the environment.

Next, the quantization of the full capacitance matrix model is presented, which follows the same quantization procedures introduced in section 2.2. The phase relation in the qubit loop is given as

$$\gamma_{32} = \gamma_{21} + \gamma_{13} + 2\pi f \tag{5.1}$$

We first consider only the individual CSFQ, and the electric energy of the qubit is written as

$$T = \frac{\varphi_0^2}{2}\dot{\gamma}^T C \dot{\gamma} + \varphi_0 \dot{\gamma}^T D Q_g, \tag{5.2}$$

where $\varphi_0 = \frac{\hbar}{2e}$ is the reduced flux quantum and

$$\dot{\gamma} = \begin{pmatrix} \dot{\gamma}_{21} \\ \dot{\gamma}_{31} \\ \dot{\gamma}_{10} \end{pmatrix}, \; Q_g = \begin{pmatrix} C_{g1}V_{g1} \\ C_{g2}V_{g2} \\ C_{g3}V_{g3} \end{pmatrix}, \tag{5.3}$$

representing the vector of the time-evolution of phases, and gate charges respectively. The gate voltage is assumed to be time-independent, so the gate charges are constants and Eq 5.2 has neglected the offset energies related to Q_g^2. The capacitance matrix is given as

$$C = \begin{pmatrix} C_{12}+C_{23}+C_{2g}+C_{02} & -C_{23} & C_{2g}+C_{02} \\ -C_{23} & C_{13}+C_{23}+C_{3g}+C_{03} & C_{3g}+C_{03} \\ C_{2g}+C_{02} & C_{3g}+C_{03} & C_{1g}+C_{2g}+C_{3g}+C_{01}+C_{02}+C_{03} \end{pmatrix}, \tag{5.4}$$

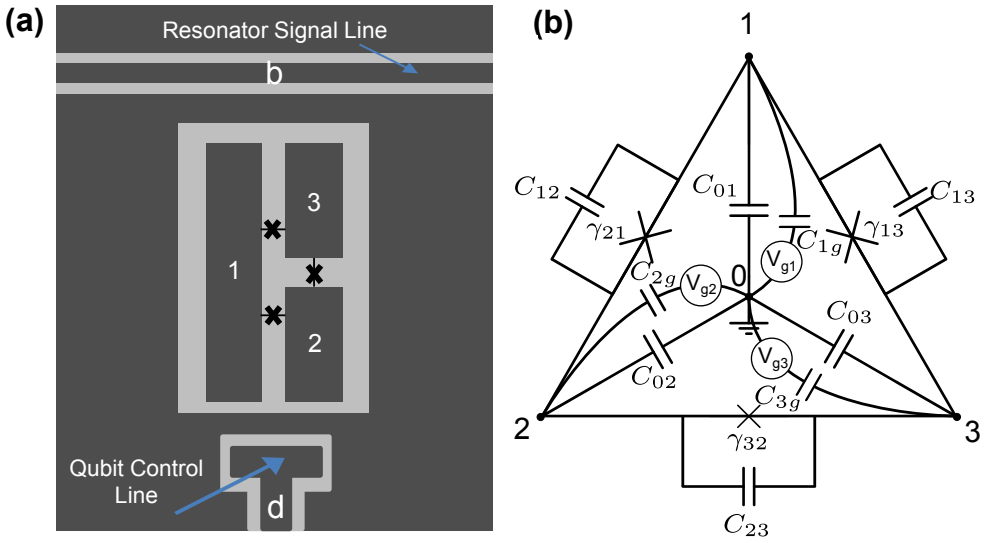

Figure 5.1: Diagram of circuit design and model. a) Device diagram, where the dark area is aluminum and the bright area is the silicon. The Al circuits layer are on top of the silicon substrate. The flux qubit contains three junctions represented by three crosses, which are capacitively shunted by three pads labeled as pad 1, 2 and 3. The qubit is capacitively coupled to a coplanar waveguide resonator and a drive line. The center line of the CPW and the drive pad are labeled as b and d respectively. b) The circuit model of the device. Node 0, 1, 2 and 3 represents the ground plane and the three shunting pads. C_{ij} is the capacitance between node i and j. The junction phases are equivalent to the phases between corresponding nodes and they are represented by γ_{ij}. V_{gi} and C_{ig} represent the gate voltage and gate capacitance with respect to node i.

and the D matrix is given as

$$D = \begin{pmatrix} 0 & -1 & 0 \\ 0 & 0 & -1 \\ -1 & -1 & -1 \end{pmatrix}. \tag{5.5}$$

The potential energy of the qubit is contributed by the Josephson energy of the junctions and is given as

$$U = -\varphi_0 \left[I_{C12} \cos \gamma_{12} + I_{C13} \cos \gamma_{13} + I_{C23} \cos(\gamma_{21} + \gamma_{13} + 2\pi f \right], \tag{5.6}$$

where I_{Cij} is the critical current of the junction located between node i and j. Similar to a typical persistent current qubit introduced in section 2.2, the CSFQ contains two

reference junctions and an α junction and the relation between the critical currents is $I_{C12} = I_{C13} = I_{C23}/\alpha$.

The Lagrangian of the system is given as $\mathcal{L} = T - U$. Then, we are going to check whether the Euler-Lagrange equation $\frac{d}{dt}\frac{\partial \mathcal{L}}{\partial \dot{\gamma}} = \frac{\partial \mathcal{L}}{\partial \gamma}$ holds. Applying the Euler-Lagrange equation on γ_{21}, we have

$$\begin{aligned} \varphi_0^2[C_{12}\ddot{\gamma}_{21}+C_{23}(\ddot{\gamma}_{21}-\ddot{\gamma}_{31})+C_{2g}(\ddot{\gamma}_{21}-\ddot{\gamma}_{10})+C_{02}(\ddot{\gamma}_{21}+\ddot{\gamma}_{10})] \\ = \varphi_0\left[-I_{C12}\sin\gamma_{21} - I_{C23}\sin(\gamma_{21}+\gamma_{13}+2\pi f)\right]. \end{aligned} \tag{5.7}$$

The left hand side of the equation $\frac{d}{dt}\frac{\partial \mathcal{L}}{\partial \dot{\gamma}_{21}}$ equals to φ_0 times all currents leaving node 2 through capacitors, and the right hand side $\frac{\partial \mathcal{L}}{\partial \gamma_{21}}$ equals to φ_0 times all currents flowing into node 2 via Josephson junctions, so the equation is correct. Similar methods also hold for γ_{13}, which refers to the currents flowing into and out of node 3. As for γ_{10}, both sides of the equation equal to 0, which means that the number of charges on the ground plane is a constant. Overall, the Euler-Lagrange equation holds for all three degrees of freedom. The conjugate momentum vector $p = (p_{21}, p_{31}, p_{10})$ of γ is found to be

$$p = \nabla_{\dot{\gamma}} T = \varphi_0^2 C\dot{\gamma} + \varphi_0 D Q_g. \tag{5.8}$$

We find the term $\frac{d}{dt}\frac{\partial \mathcal{L}}{\partial \dot{\gamma}}$ in the Euler-Lagrange equation is related to the currents entering and leaving the corresponding nodes, and $\frac{d}{dt}\frac{\partial \mathcal{L}}{\partial \dot{\gamma}} = \dot{p}$, so p/φ_0 represents the charges on the corresponding nodes.

Following the Legendre transformation $H = p\dot{\gamma} - T$, we find the Hamiltonian

$$H = \frac{1}{2}\left(\frac{p}{\varphi_0} - DQ_g\right)^T C^{-1}\left(\frac{p}{\varphi_0} - DQ_g\right) + U(\gamma). \tag{5.9}$$

Compared to the Hamiltonian of a typical persistent current qubit Eq 2.18, p refers to the charges on qubit islands or ground planes instead of the charges stored in junction capacitance, and there is an additional term of offset charges due to gate charges in the full capacitance matrix model.

When considering the CPW resonator and the drive line, these two elements can be considered as contributions to the gate capacitances and gate voltages. The final Hamiltonian becomes

$$H = \frac{1}{2}\left(\frac{p}{\varphi_0} - DQ_g - DQ_b - DQ_d\right)^T C'^{-1}\left(\frac{p}{\varphi_0} - DQ_g - DQ_b - DQ_d\right) + U(\gamma). \tag{5.10}$$

The Hamiltonian contains two additional offset charges, which are

$$Q_b = \begin{pmatrix} C_{b1}V_{b1} \\ C_{b2}V_{b2} \\ C_{b3}V_{b3} \end{pmatrix}, \; Q_d = \begin{pmatrix} C_{d1}V_{d1} \\ C_{d2}V_{d2} \\ C_{d3}V_{d3} \end{pmatrix}, \tag{5.11}$$

where V_{bi} or V_{di} is the voltage between node i and the resonator or the drive line. The capacitance matrix becomes $C' = C + C_b + C_d$, where

$$C_b = \begin{pmatrix} C_{2b} & 0 & C_{2b} \\ 0 & C_{3b} & C_{3b} \\ C_{2b} & C_{3b} & C_{1b} + C_{2b} + C_{3b} \end{pmatrix}, \; C_d = \begin{pmatrix} C_{2d} & 0 & C_{2d} \\ 0 & C_{3d} & C_{3d} \\ C_{2d} & C_{3d} & C_{1d} + C_{2d} + C_{3d} \end{pmatrix}, \tag{5.12}$$

with C_{ib} the capacitance between node i of the qubit and the resonator center line and C_{id} the capacitance between node i and the drive line.

5.2 Device fabrication

This section describes the fabrication process of the device, consisting of superconducting Al circuits on the Si substrate. The fabrication is a three-layer process, composed of the maker layer, the resonator layer and the qubit layer. The marker layer provides markers for alignment between the circuit layer and the qubit layer, which are essential for lithography. The resonator layer contains the circuits with large features such as CPW resonators, open transmission lines, ground planes, qubit control lines, etc. Both the marker layer and the circuit layer is processed with photolithography with resolution around 1 μm. The qubit layer is fabricated with the electron-beam lithography, whose resolution is at tens of nanometer, so fine features like Josephson junctions and qubit wires are included in this layer.

Before fabricating the CSFQ device, I worked on developing a fabrication recipe for the marker and resonator layer using a new photolithography system, Maskless aligner (MLA) 150 from Heidelberg Instruments. The MLA 150 is an optical direct-writing lithography system with no need of masks and fast writing speed. Its highest resolution is 1 μm, so it is appropriate for fabrication of coarse features, such as markers and resonator circuits. In our original recipe, a mask aligner was used for photolithograph, which requires that the patterns of circuits have to be first fabricated on a mask, and then be transferred to the photon resist that is coated on the sample surface. Compared to the mask aligner, the MLA 150 can directly write patterns onto resist without any mask, so it saves time

and money for fabricating masks, and it has excellent adaptability to new designs or small changes on the patterns. The tests on MLA 150 contained dose and defoc tests for two resists that were used for the two layers. Dose is related to the intensity of light and defoc represents the position of the focus of light with respect to the surface of the resist. The tests showed that the MLA 150 had excellent compatibility to our superconducting devices and the new recipe was used to fabricate the CSFQ device.

Next, the main steps in the fabrication process for each layer is introduced. For the marker layer, the fabrication starts with a chemical cleaning of the substrate, which is a 4" Si wafer, by sonication in acetone, isopropyl alcohol (IPA) and de-ionized (DI) water. Then, the substrate is coated with a layer of positive resist Shipley s1811, followed by the photolithography with MLA 150 and developing in MF 319. The exposed Si after the developing is etched to form Si etched markers with depth of 2 μm. Afterwards, the resist is removed by sonication in a hot bath of remover PG and then cleaned in acetone and IPA baths. This finishes the process of the marker layer.

As for the resonator layer, the sample is first coated with a layer of negative resist ma-N 1410 followed by doing photolithography with MLA 150 and developing in ma-D 533/S. Then, 100 nm Al is deposited on the sample with high-vacuum electron-beam evaporation. After evaporation, the part of Al layer on the resist is lifted-off in a hot bath of Remover PG followed by acetone and IPA cleaning. Up to this step, the fabrication of the main features of circuits including ground planes, resonators, qubit drive lines and large-shunting pads of the CSFQ are finished.

At last, the fabrication moves on to the qubit layer containing the qubit Al wires and Josephson junctions between the shunting pads. The sample is first coated with two layers of electron-beam resist polymethylglutarimide (PMGI) and polymethylmethacrylate (PMMA), followed by doing 100 kV electron-beam lithography and developing in MIBK:IPA (1:3). The sample is then processed with oxygen descum to remove any resist residue on the substrate. Afterwards, an argon milling process at two angles 20° and $-20°$ is carried out to remove the Al oxide layer from the areas where the shunting pads are designed to contact with qubit wires. The purpose of doing argon milling at two angles is to create a taper profile at the edge of shunting pads to provide better contact to qubit Al wires. Next, the sample is deposited with a 45nm Al layer at the angle of 20° followed by an in-situ oxidation process to create the junction barrier, then a second layer of Al with 65 nm is deposited at 20° to form junctions. After deposition, the sample is lifted-off in a hot bath of Remover PG and then cleaned with acetone and IPA baths. Up to this step, the fabrication of superconducting circuits are completed. The sample is then diced into 3 mm $\times$ 7 mm small devices, which are wirebonded to microwave packages and mounted inside the dilution fridge for low temperature measurements. Fig 5.2 shows the images of

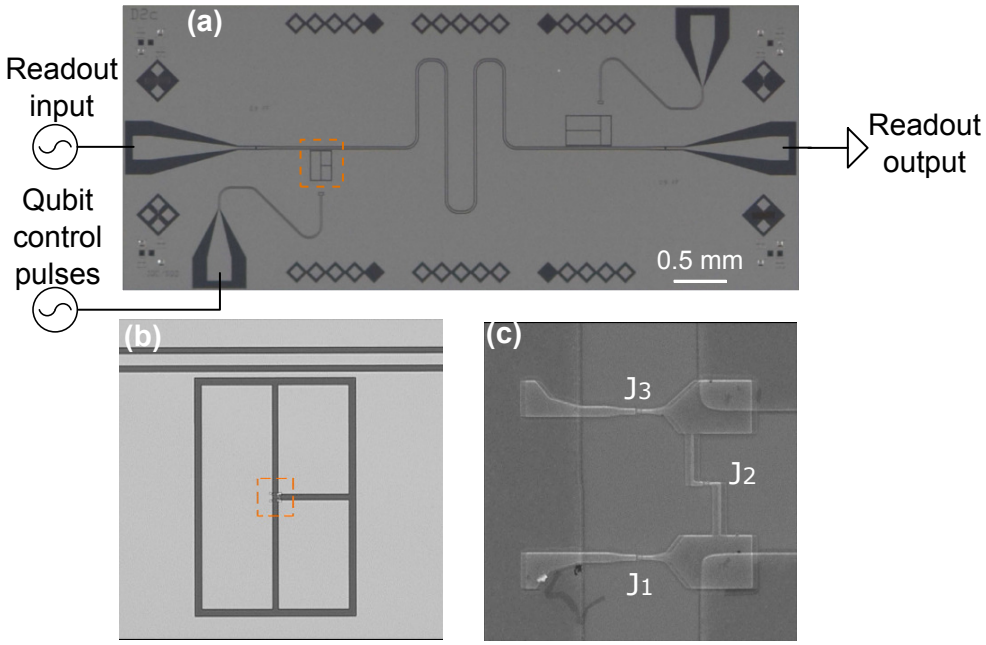

Figure 5.2: Images of the fabricated CSFQ device. a) Photograph of a 3 mm × 7mm device. The bright area is Al and the dark area is Si. A $\lambda/2$ CPW resonator located in the center of the device and it is coupled to two CSFQs with different designs. Each CSFQ is coupled to a drive line. The qubit in the dashed rectangle is the one measured in the experiment. b) The microscope image of the CSFQ labeled in a. It has three shunting pads and the qubit loop is in the center area and is circled by the dashed rectangle. c) The scanning electron microscope image of the qubit loop. The three junctions are located in between the shunting pads.

the device and qubits measured in the experiment.

5.3 Experiment results

In this section, we present the experiment procedures and measurement results of the qubit spectroscopy and the qubit coherence. We further investigates the qutrit constituted by the lowest three level. The qutrit state tomography and multilevel relaxation analysis are presented.

5.3.1 Qubit spectroscopy

The preliminary step of the experiment is conducting qubit spectroscopy measurements, which is to find the lowest several energy levels of the qubit and their dependencies on the flux bias. The $\lambda/2$ resonator is used to weakly drive the qubit and measure the qubit state by sending pulses to the resonator and measure the homodyne voltages of the transmitted signals. The homodyne voltage is the average of the voltages that are measured during the length of each pulse, which is 10 μs. The pulse frequencies are swept over a large range to identify the transition frequencies between the lowest three energy levels.

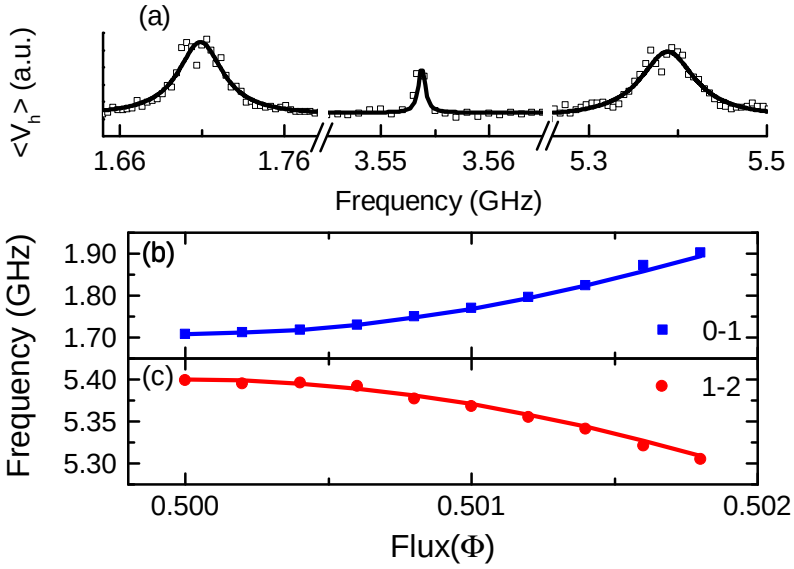

Figure 5.3: Qubit spectroscopy. a) Diagram of the homodyne voltages represented by squares versus the frequencies of driving pulses when qubit is at the symmetry point $f = 0.5$. The solid line is Lorentz fitting to locate the peaks; Frequencies of b) 0-1 transitions and c) 1-2 transitions versus the external flux in the qubit. The flux is in the unit of a flux quantum Φ_0. The measured transition frequencies are represented by the blue and red points, while the solid line shows the fitting by the full capacitance matrix model.

Fig 5.3 a shows the measured homodyne voltages over a range of pulse frequencies. We find that the first peak from the left is caused by the 0-1 transition with the transition frequency $\omega_{01} = 2\pi \times 1.708$ GHz. The second peak corresponds to a two-photon process

with frequency at $\omega_{02}^{2p} = 2\pi \times 3.533$ GHz, in which the qubit is first excited by a photon with frequency ω_{02}^{2p} and then it is excited again by a photon with the same frequency. The two-photon process moves the qubit from state 0 to state 2. The third peak refers to 1-2 transitions at frequency $\omega_{12} = 2\pi \times 5.4$ GHz. Thus, the qubit anharmonicity $\mathcal{A} = \omega_{12} - \omega_{01}$ at the symmetry point reaches $2\pi \times 3.628$ GHz.

We also measure the qubit spectroscopy while tuning the flux bias to see the dependencies of qubit transitions on the external flux. The results for the 0-1 and 1-2 transitions are shown in Fig 5.3 b and c. We use the full capacitance matrix model introduced in section 5.1 to fit the spectroscopy data. The capacitance matrix in the model is extracted from circuit simulations, and the fitting parameters includes only the junction critical current density J_c and the size of the α junction α. The model fits the spectroscopy well with the fitting parameters $J_c = 4\mu\text{A}/\mu\text{m}^2$ and $\alpha = 0.61$, which are very close to the nominal values from fabrication.

5.3.2 Qubit coherence

In this section, qubit coherence at the symmetry point is presented. In the relaxation measurement, the qubit is first prepared at state 0 and then excited to state 1 by applying a π^{01} pulse through the drive line. Then, the qubit relaxation starts. After a delay time, the readout pulse with a frequency near the qubit transition frequency is sent into the resonator, and the homodyne voltage is measured. This process is then repeated with increasing delay times. Fig 5.4 a shows the measured homodyne voltage versus delay time in a relaxation measurement. The values of homodyne voltages reflect the qubit states, i.e, the voltages at $t = 0$ and at the end of the delay time correspond to the qubit at state 1, and state 0 respectively. The relaxation time T_1 is obtained from exponential fitting of the homodyne voltages. Fluctuations of T_1 is observed during the experiment, as reported in other experiments [35] [36] [37]. The T_1 is in the range 40 ± 5 μs with the highest $T_1 = 47.1 \pm 2.$ μs, which is comparable to the highest T_1 ever measured for the CSFQ [2].

We also measured the total dephasing time T_2, which is defined as $\frac{1}{T_2} = \frac{1}{2T_1} + \frac{1}{T_\varphi}$, where T_1 is the relaxation time and T_φ is the pure dephasing time introduced in section 3.1.3. The coherence time measured from Ramsey and Spin-echo [38] experiments are $T_{2\text{R}} = 4.7$ μs and $T_{2\text{E}} = 9.4$ μs. We perform dynamical decoupling with the CPMG pulse protocol [39], where the pulse sequence consists of two $\pi/2$ pulses spaced with time τ and N equally spaces π pulses in between, so the total free precision time of the state is increased. With $N = 1$, the CPMG has the same pulse sequence as the spin-echo process. While varying the number of π pulses, we are able to analyze the correlation of the noise and extract the

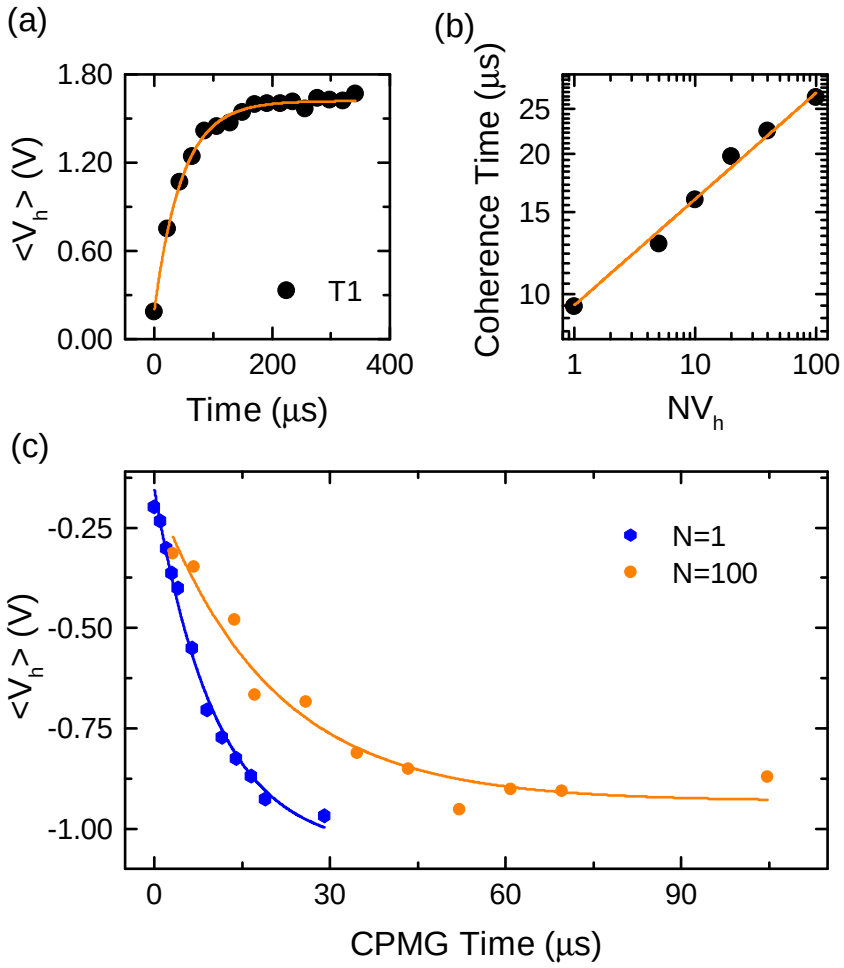

Figure 5.4: Qubit coherence at the symmetry point. a) Diagram of homodyne voltage versus delay time in the relaxation measurement. The solid line is an exponential fitting. b) Diagram of the coherence time versus the number of CPMG pulses N. c) Diagram of homodyne voltage versus delay time in the CPMG measurement for $N = 1$ and $N = 100$. The solid line is exponential fitting.

noise spectrum. Fig 5.4 b shows the CPMG coherence time versus the number of pulses, with $T_{\mathrm{CPMG}} = 26.5$ μs for $N = 100$ which is extracted from Fig 5.4 c.

5.3.3 Qutrit tomography

The large anharmonicity of our qubit enables precise quantum control inside the multilevel energy structure. We consider the qutrit constituted by the lowest three states, and perform the qutrit state tomography to reconstruct its full density matrix and evaluate the the tomography fidelities for a set of states.

The qubit density matrix can be written as a linear combination of the identity matrix and the special unitary group of degree 2, denoted SU(2), which are the Pauli matrices. Similarly, the density matrix of a qutrit can be written in the form of

$$\rho = \frac{1}{3}\sum_{j=0}^{8} r_j \lambda_j, \tag{5.13}$$

where λ_j is the SU(3) generator and is given by [40]

$$\begin{aligned}
\lambda_1 &= \begin{pmatrix} 0 & 1 & 0 \\ 1 & 0 & 0 \\ 0 & 0 & 0 \end{pmatrix}, \ \lambda_2 = \begin{pmatrix} 0 & -i & 0 \\ i & 0 & 0 \\ 0 & 0 & 0 \end{pmatrix}, \ \lambda_3 = \begin{pmatrix} 1 & 0 & 0 \\ 0 & -1 & 0 \\ 0 & 0 & 0 \end{pmatrix} \\
\lambda_4 &= \begin{pmatrix} 0 & 0 & 1 \\ 0 & 0 & 0 \\ 1 & 0 & 0 \end{pmatrix}, \ \lambda_5 = \begin{pmatrix} 0 & 0 & -i \\ 0 & 0 & 0 \\ i & 0 & 0 \end{pmatrix}, \ \lambda_6 = \begin{pmatrix} 0 & 0 & 0 \\ 0 & 0 & 1 \\ 0 & 1 & 0 \end{pmatrix} \\
\lambda_7 &= \begin{pmatrix} 0 & 0 & 0 \\ 0 & 0 & -i \\ 0 & i & 0 \end{pmatrix}, \ \lambda_8 = \frac{1}{\sqrt{3}} \begin{pmatrix} 1 & 0 & 0 \\ 0 & 1 & 0 \\ 0 & 0 & -2 \end{pmatrix}.
\end{aligned} \tag{5.14}$$

The density matrix can be reconstructed by measuring the expectation values of the generators $\langle \lambda_j \rangle = r_j$, or performing measurements on another complete set of basis states. Following the experiment procedures in [41], we first prepare the qutrit at a given state, then apply one of nine unitary rotations U_k that construct a complete basis, followed by state readout. These steps are repeated until nine independent measurements corresponding to the nine unitary rotations are done. The unitary rotations are composed of a single or multiple rotations around the x or y axes of the Bloch sphere of 0-1 space or 1-2 space. They are in the form of $R_a^b(\theta)$, where $a = x$ or y, $b = 01$ or 12 and θ is the rotation angle, and the nine rotations are listed in table 5.1. The observable in our experiment is the operator of the homodyne voltage given as

$$V_h = V_{h0}|0\rangle\langle 0| + V_{h1}|1\rangle\langle 1| + V_{h2}|2\rangle\langle 2|, \tag{5.15}$$

State Prep.	Rotations	Tomog. Pulses	Rotations
P_0	I	u_0	$R_x^{01}(\pi)$
P_1	$R_x^{01}(\pi)$	u_1	$R_x^{01}(\pi/2)$
P_2	$R_x^{12}(\pi)R_x^{01}(\pi)$	u_2	$R_y^{01}(\pi/2)$
P_3	$R_x^{01}(\pi/2)$	u_3	I
P_4	$R_y^{01}(\pi/2)$	u_4	$R_x^{01}(\pi)R_x^{12}(\pi/2)$
P_5	$R_x^{12}(\pi/2)R_x^{01}(\pi)$	u_5	$R_x^{01}(\pi)R_y^{12}(\pi/2)$
P_6	$R_y^{12}(\pi/2)R_x^{01}(\pi)$	u_6	$R_x^{01}(\pi)R_x^{12}(\pi/2)R_x^{01}(\pi)$
P_7	$R_x^{12}(\pi)R_x^{01}(\pi/2)$	u_7	$R_x^{01}(\pi)R_y^{12}(\pi/2)R_x^{01}(\pi)$
P_8	$R_x^{12}(\pi)R_y^{01}(\pi/2)$	u_8	$R_x^{01}(\pi)R_x^{12}(\pi)R_x^{01}(\pi)$

Table 5.1: Sets of rotation pulses for state preparation and qutrit tomography.

where V_{hi} represents the homodyne voltage corresponding to state i. In the new basis, the observable becomes $U_k V_h U_k^\dagger$, and the measured average voltage is given as

$$V_k = \mathrm{Tr}\left[\rho U_k V_h U_k^\dagger\right]. \tag{5.16}$$

Substituting the expression of the density matrix Eq 5.13, we have

$$\begin{aligned} V_k &= \frac{1}{3}\mathrm{Tr}\left[\sum_{j=0}^{8} r_j \lambda_j U_k V_h U_k^\dagger\right] \\ &= \sum_{j=0}^{8} \frac{1}{3}\mathrm{Tr}\left[\lambda_j U_k V_h U_k^\dagger\right] r_j. \end{aligned} \tag{5.17}$$

Since λ_j, U_k and V_h are known and V_k is the measured average voltage, we are able to find r_j, with which the density matrix can be reconstructed using Eq 5.13.

We performed qutrit tomography to a set of given states P_0 to P_8, which are prepared by applying the corresponding rotation pulses as shown in table 5.1. Fig 5.5 shows the density matrixes reconstrcted by the qutrit tomography for two initial states. The fidelity between the density matrix of the expected state and the reconstructed one for both processes is 99.2%. The high fidelity shows we able to perform precise quantum control in the qutrit space.

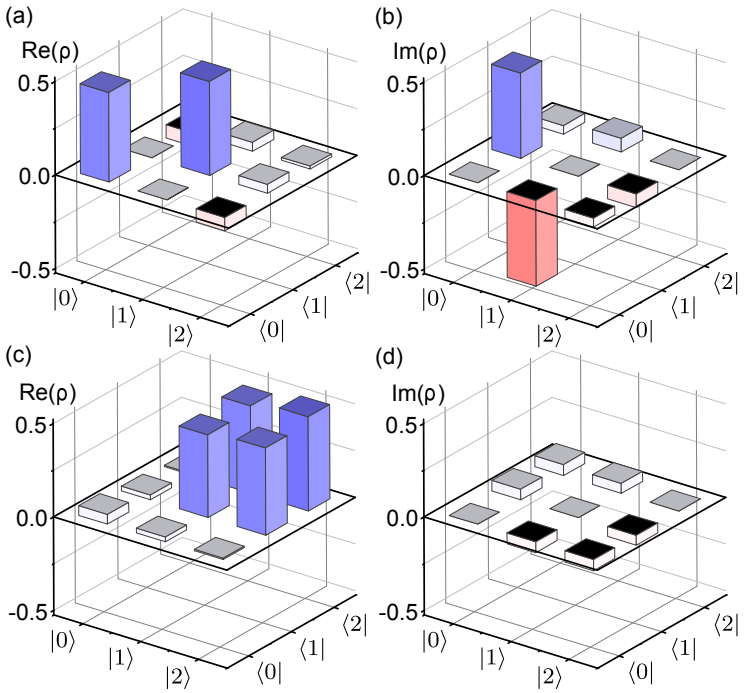

Figure 5.5: Diagram of matrix elements of the reconstructed density matrix from qutrit tomography. a) and b) shows the real and imaginary part of the matrix elements for the initial state prepared with $R_x^{01}(\pi/2)$ pulse. c) and d) shows the real and imaginary part of the matrix elements for the initial state prepared with $R_y^{12}(\pi/2)R_x^{01}(\pi)$ pulses.

5.3.4 Multilevel relaxation analysis

In this section, we first introduce the experiment steps of the multilevel relaxation measurement and present how state populations are extracted. Then, the multilevel relaxation model is presented, which shows an excellent fitting to the measurement results. The fitting conditions are discussed.

We consider a qutrit consisting the lowest three levels of the qubit. When we read the qutrit state, the measured homodyne voltage is given as

$$V_{\text{avg}} = \text{Tr}\left[\rho V_h\right], \tag{5.18}$$

where V_h is the operator of the homodyne voltage. Plugging the expression of V_h Eq 5.15, we have

$$\begin{aligned} V_{\text{avg}} &= \text{Tr}\left[\rho(V_{h0}|0\rangle\langle 0| + V_{h1}|1\rangle\langle 1| + V_{h2}|2\rangle\langle 2|)\right] \\ &= V_{h0}p_0 + V_{h1}p_1 + V_{h2}p_2, \end{aligned} \tag{5.19}$$

with p_0, p_1 and p_2 the populations at state 0, 1 and 2. In the experiment of characterizing the multilevel coherence at the flux symmetry point, the qutrit is first prepared at its steady state by waiting long enough time, then it is excited by applying π_x^{01} and π_x^{12} pulses. We did not use π_x^{02} pulse to excite the qutrit is because the 0-2 transition is forbidden at the flux symmetry point. The qutrit state is measured after a certain delay time t. Then, a π_x^{01} pulse is applied to swap the populations of state 0 and 1, followed by the second state readout. These steps are repeated with increasing delay times. The two readout results are given as

$$V_{\text{avg}}(t) = V_{h0}p_0(t) + V_{h1}p_1(t) + V_{h2}p_2(t) \tag{5.20}$$

$$V'_{\text{avg}}(t) = V_{h0}p_1(t) + V_{h1}p_0(t) + V_{h2}p_2(t). \tag{5.21}$$

We assume there is no populations at any state higher than state 3, so the sum of the populations at the first three states equals to 1

$$p_0 + p_1 + p_2 = 1. \tag{5.22}$$

In these three equations, V_{avg} and V'_{avg} are measured voltages, and V_{h0}, V_{h1} and V_{h2} are characterized homodyne voltages for the three states, so we able to extract the time-dependent state populations. Fig 5.6 shows the evolution of state populations during the relaxation process. The solid lines are fittings using the three-level relaxation model proposed in [42].

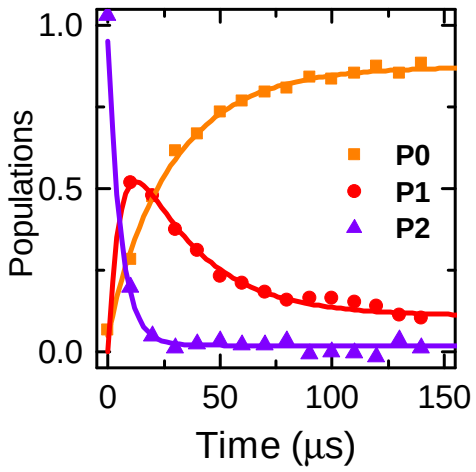

Figure 5.6: Populations of three states versus the delay time of the relaxation experiment with the qubit at the flux symmetry point.

The derivation of the model starts from the rate equations

$$\begin{aligned}
\frac{dn_0^\star}{dt} &= -n_0^\star(R_{01}+R_{02}) + n_1^\star R_{10} + n_2^\star R_{20},\\
\frac{dn_1^\star}{dt} &= n_0^\star R_{01} - n_1^\star(R_{10}+R_{12}) + n_2^\star R_{21},\\
\frac{dn_2^\star}{dt} &= n_0^\star R_{02} + n_1^\star R_{12} - n_2^\star(R_{20}+R_{21}),
\end{aligned} \tag{5.23}$$

where $n_i^\star$ represents the population of level i and R_{ij} is the transition rate from level i to level j. By normalizing the population with respect to the total population,

$$n_1 = \frac{n_1^\star}{n_t};\ n_2 = \frac{n_2^\star}{n_t}, \tag{5.24}$$

we arrive at

$$\begin{aligned}
1 &= n_0 + n_1 + n_2\\
\frac{dn_1}{dt} &= R_{01} - n_1(R_{10}+R_{12}+R_{01}) + n_2(R_{21}-R_{01}),\\
\frac{dn_2}{dt} &= R_{02} - n_1(R_{12}-R_{02}) - n_2(R_{20}+R_{21}+R_{02}).
\end{aligned} \tag{5.25}$$

The final solutions of the time dependent populations are given by

$$\begin{aligned}
n_0(t) &= 1 - n_1(t) - n_2(t)\\
n_1(t) &= C_0\exp(-\xi_0 t) + C_1\exp(-\xi_1 t) + \frac{Q_1}{B},\\
n_2(t) &= C_0\frac{R_1-\xi_0}{R_{21}^\star}\exp(-\xi_0 t) + C_1\frac{R_1-\xi_1}{R_{21}^\star}\exp(-\xi_1 t) + \frac{Q_2}{B}.
\end{aligned} \tag{5.26}$$

The definitions of parameters can be found in table I of [42]. Eventually, the time dependent populations $n_1(t)$ and $n_2(t)$ are written in expressions only composed of transition rates R_{ij} and initial populations at level 1 and 2, $n_1(t=0)$ and $n_2(t=0)$.

Next, we introduce how to find the initial populations of n_1 and n_2. In the multilevel relaxation experiment at the flux symmetry point, the qutrit is first prepared at its steady state, so the populations at three states are the steady state populations $n_0 = p_{ss0}$, $n_1 = p_{ss1}$ and $n_2 = p_{ss2}$. Then, the qutrit is excited by two pulses π_x^{01} and π_x^{12}, so the populations at state 0, 1 and 2 becomes $n_0 = p_{ss1}$, $n_1 = p_{ss2}$ and $n_2 = p_{ss0}$. Afterwards, the qutrit starts relaxing, so the populations at state 1 and 2 when $t = 0$ are $n_1(t=0) = p_{ss2}$ and $n_2(t=0) = p_{ss0}$. Due to thermal excitations, the qutrit steady state is not its ground

state, so $p_{ss0} < 1$. For simplicity, we assume $p_{ss2} = 0$, which is also reasonable due to the large gap between state 0 and 2. To characterize the steady state populations we perform two rabi experiments. In the first one, the qutrit is prepared at the steady state, then the populations at state 1 and 2 are swapped by a π_x^{01} pulse, as shown in Fig 5.7 b. Afterwards, 0-1 rabi experiment is performed, where the amplitude of rabi oscillation A_0 is proportional to p_{ss0}. In the second one, π_x^{01} and π_x^{12} pulses are applied to the qutrit steady state. The state populations are shown in Fig 5.7 c. Then, 0-1 rabi experiment is performed, from which we obtain the amplitude of the rabi oscillation A_1, which is proportional to p_{ss1}. Therefore, we obtain the relation $\frac{A_0}{A_1} = \frac{p_{ss0}}{p_{ss1}}$. With the assumption $p_{ss0}+p_{ss1} = 1$, we are able find the steady state populations of the qutrit. In experiments, we find $p_{ss0} = 0.95 \pm 0.02$. Assuming the qutrit reaches the thermal equilibrium when it is at the steady state, so the ratio p_{ss0} to p_{ss1} equals to the Boltzman factor $p_{ss0}/p_{ss1} = \exp(-\hbar\omega_{01}/K_B T)$, yielding the effective temperature T in the range $27 - 32$ mK, which shows a good match to the cryostat temperature 27 mK. In other experiments on superconducting qubits [43, 44], large differences between the effective temperature and the cryostat temperature are observed for qubits with long coherence times.

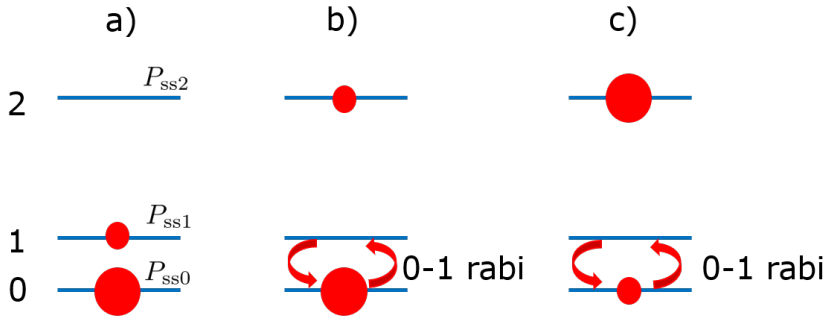

Figure 5.7: Diagram of populations at state 0, 1 and 2 for characterization of steady state populations. a) The qutrit is at the steady state, b) A π_x^{01} pulse is applied to the qutrit steady state to swap the populations at state 0 and 1, and c) π_x^{01} and π_x^{12} pulses are applied to the qutrit steady state to swap the populations at state 0 and 1 followed by swap between state 1 and 2. The steady state populations are represented by red disks with different sizes.

Plugging the steady state populations to Eq 5.26, the time dependent populations are only determined by the transition rates R_{ij}, and the population equations are used to fit the populations extracted from qutrit relaxation measurement. In the experiment of qubit coherence introduced in section 5.3.2, we find the relaxation rate of the qubit given as $\Gamma_1 = \frac{1}{T_1}$. It is related to the up and downward transition rates by $\Gamma_1 = R_{10} + R_{01}$. The

Rate	at 0.5 Φ_0	at 0.501 Φ_0
R_{01}	1.4 kHz	1.2kHz
R_{10}	29.5 kHz	63.4kHz
R_{12}	8.8 kHz	0.4kHz
R_{21}	124.3 kHz	78.1kHz
R_{02}	0.1 kHz	0.01kHz
R_{20}	27.8 kHz	61.1kHz

Table 5.2: Qutrit transition rates obtained from measurements of multilevel coherence.

transition rates are also related to the steady state populations as $R_{10}/R_{01} = p_{ss0}/p_{ss1}$. With these two equations, R_{10} and R_{01} can be found. In the fit, we assume the effective temperatures for 0-2 and 1-2 transitions are the same to that of the 0-1 transition, so we have restrictions on the ratios of R_{21}/R_{12} and R_{20}/R_{02}. Therefore, there are only two fitting parameters R_{21} and R_{20} in the fitting. The multilevel relaxation model fits the relaxation data well as shown in Fig 5.6. The transition rates are listed in table 5.2. We also performed multilevel coherence measurements at an off-symmetry point where $\Phi_{\text{ext}} = 0.501\Phi_0$, the transition rates are found comparable to those at the symmetry point as shown in table 5.2. Although flux noise can not cause 2-0 transitions at the symmetry point due to the selection rule, the extracted transition rate R_{20} is not 0. We think the transition may be caused by charge noise or coupling to the resonator.

5.4 Summary

We have presented a new design of capacitive shunted flux qubit and the full capacitance matrix circuit model. We test a new photolithography system MLA 150, and utilize it in the fabrication of the CSFQ device. The qubit lowest three energy levels are characterized with qubit spectroscopy measurement, and the energy levels at different flux biases is the great agreement to the capcitance matrix model. We observe large qubit anharmonicity $\mathcal{A} = \omega_{12} - \omega_{01} = 2\pi \times 3.69$ GHz and large relaxation time reaching as high as 47 μs. We perform qutrit tomography to reconstruct the full density matrix, and the tomography fidelity reaches 99.2%. We measure the multilevel relaxation, and use the multilevel relaxation model to extract the transition rates.

Chapter 6

Conclusion

In this thesis, we have presented results on two topics, which are the design of a new experiment on the fast switchable ultrastrong coupling between superconducting artifical atoms and electromagnetic fields, and the development of the capacitively shunted flux qubit.

The project of ultrastrong coupling is concerned with the study the spin-boson model when the coupling strength between the two-level system and the bosonic bath reaches the ultrastrong coupling regime. We propose three experiments to directly measure the coherence of the two-level system including the relaxation and dephasing, and the the renormalized tunnling frequencies in the ultrastrong coupling regime and in a controllable manner. We present a novel design of a fast-switchable coupling system based on superconducting circuits, which consists of a two-loop flux qubit galvanically coupled to an open transmission line, qubit bias lines, qubit drive lines and state readout circuits. By controlling the two fluxes in the two qubit loops, we can fast switch off the coupling and quickly tune the coupling strength into the ultrastrong coupling regime, which results in the capability of measuring the system dynamics in the ultrastrong coupling regime with a controllable manner. Detailed experiment steps and pulse sequences of two bias fluxes and readout signals are presented for each experiment.

The core of the USC experiment is the design and circuit model of the flux qubit, which is composed of a main loop and a coupler loop. The qubit design is inspired by two-qubit couplers. Compared to the tunable qubit in [1], this qubit can be effectively decoupled from the open transmission line. Simulations of qubit properties such as qubit transition frequencies, anharmonicities and persistent currents are presented. We estimate the coupling strengths that are characterized by α_{SB}, the qubit relaxation rates, as well

as the pure dephasing rates that are caused by low frequency current noises in the open transmission line. The overlaps between the states at the ultrastrong coupling points and the subspace spanned by the ground and the excited states at the decoupling point are simulated. The results shows that there are still large overlaps for points in the ultrastrong coupling regime. We demonstrate that the three proposed experiments can be well implemented based on the simulation results.

Qubit bias, driving and readout circuits are important parts of the device. The qubit is biased and drived with two inductively coupled flux lines. We send DC signals to provide static flux bias, and fast pulses to drive the qubit and tune the flux bias. The high-frequency pulses enables fast-tuning of flux bias, resulting in the fast-switchable coupling. Qubit states are measured in the flux basis with a coplanar waveguide (CPW) resonator with one end grounded by a DC-SQUID and the other end capacitively coupled to a feedline. The circuit model is presented, and the resonance frequencies is simulated. Finally, we simulate the coupling strengths between the qubit and flux lines or the readout resonator and we find that compared to the open transmission line, these two circuits are not main decoherence sources of the qubit.

In the second part of the thesis, we propose a new design of CSFQ, which contains three Josephson junctions and three shunting pads. Shuning all three Josephson junctions redistributes the electric field from the area of lossy junction barrier to large shunting pads uniformly, which effectively reduce the participation of the lossy materials and leads to better qubit coherence. Besides, since the capacitive pads, which dominate the junction capacitances, have much larger sizes than junction areas, the reproducibility of CSFQ device in fabrication has been greatly improved. In experiments, the qubit energy levels at different flux biases matches well with the full capacitance matrix model, which takes into account all the capacitances between the qubit and other circuits. The qubit is found to have both large anharmonicity $\mathcal{A} = 2\pi \times 3.69$ GHz, and high coherence with $T_1 = 40 \pm 5$ μs. Compared to the qubits in [2], which has the best coherence time ever reported for CSFQ, our qubit has comparable relaxation times, but much larger anharmonicity at the symmetry point.

Taking the advantage of large anharmonicity, we conduct experiments on multilevel quantum control and multilevel relaxation measurement. We perform qutrit state tomography to reconstruct the full density matrix with the tomography fidelity reaching 99.2%. We are able to extract the time-dependent state populations for the relaxation process of a qutrit, and extract the exact transition rates between the three levels with the multlevel relaxation model [42]. The multilevel relaxation time shows similar results to the qubit. The ability to perform full quantum control and having good multilevel coherence make our CSFQ applicable to quantum computations based on qutrits.

6.1 Outlook

We have presented a full device design for implementing the first experiments on directly measuring the dynamics of the spin-boson model in the ultrastrong coupling regime. The next step is proceeding to fabricate the device and perform the qubit measurement experiments. The near term goal of these experiments is the observation of the USC regime in the time domain. In the longer term, we hope that this platform can provide the basis for measurement of two-qubit entanglement and other potential applications in the field of relativistic quantum information.

We developed, implemented, and characterized a new type of qubit design — a capacitively shunted flux qubit with three capacitor pads. Unlike transmons, the CSFQ still keeps large anharmonicity while improving the coherence, which makes it a good candidate to build fast quantum gates. A good starting point for implementing CSFQ in gate-based quantum computing is to biuld fast and high-fidelity two qubit gates. Another interesting research direction is investigating the potential of utilizing CSFQ in quantum computations involving multilevel structures.

Bibliography

[1] P. Forn-Daz, J. J. Garca-Ripoll, B. Peropadre, J.-L. Orgiazzi, M. A. Yurtalan, R. Belyansky, C. M. Wilson, and A. Lupascu. Ultrastrong coupling of a single artificial atom to an electromagnetic continuum in the nonperturbative regime. *Nature Physics*, 13(1):3943, 2016.

[2] Fei Yan, Simon Gustavsson, Archana Kamal, Jeffrey Birenbaum, Adam P Sears, David Hover, Ted J. Gudmundsen, Danna Rosenberg, Gabriel Samach, S Weber, and et al. The flux qubit revisited to enhance coherence and reproducibility. *Nature Communications*, 7(1), 2016.

[3] E.t. Jaynes and F.w. Cummings. Comparison of quantum and semiclassical radiation theories with application to the beam maser. *Proceedings of the IEEE*, 51(1):89109, 1963.

[4] J. M. Raimond, M. Brune, and S. Haroche. Manipulating quantum entanglement with atoms and photons in a cavity. *Reviews of Modern Physics*, 73(3):565582, 2001.

[5] Y. Kaluzny, P. Goy, M. Gross, J. M. Raimond, and S. Haroche. Observation of self-induced rabi oscillations in two-level atoms excited inside a resonant cavity: The ringing regime of superradiance. *Physical Review Letters*, 51(13):11751178, 1983.

[6] Marlan Orvil. Scully and Muhammad Suhail. Zubairy. *Quantum optics*. Cambridge University Press, 2008.

[7] A. Wallraff, D. I. Schuster, A. Blais, L. Frunzio, R.-S. Huang, J. Majer, S. Kumar, S. M. Girvin, and R. J. Schoelkopf. Strong coupling of a single photon to a superconducting qubit using circuit quantum electrodynamics. *Nature*, 431(7005):162167, 2004.

[8] P. Forn-Daz, J. Lisenfeld, D. Marcos, J. J. Garca-Ripoll, E. Solano, C. J. P. M. Harmans, and J. E. Mooij. Observation of the bloch-siegert shift in a qubit-oscillator system in the ultrastrong coupling regime. *Physical Review Letters*, 105(23), 2010.

[9] A. Wallraff, D. I. Schuster, A. Blais, L. Frunzio, J. Majer, M. H. Devoret, S. M. Girvin, and R. J. Schoelkopf. Approaching unit visibility for control of a superconducting qubit with dispersive readout. *Physical Review Letters*, 95(6), 2005.

[10] T. Niemczyk, F. Deppe, H. Huebl, E. P. Menzel, F. Hocke, M. J. Schwarz, J. J. Garcia-Ripoll, D. Zueco, T. Hmmer, E. Solano, and et al. Circuit quantum electrodynamics in the ultrastrong-coupling regime. *Nature Physics*, 6(10):772776, 2010.

[11] Fumiki Yoshihara, Tomoko Fuse, Sahel Ashhab, Kosuke Kakuyanagi, Shiro Saito, and Kouichi Semba. Superconducting qubitoscillator circuit beyond the ultrastrong-coupling regime. *Nature Physics*, 13(1):4447, 2016.

[12] A. J. Leggett, S. Chakravarty, A. T. Dorsey, Matthew P. A. Fisher, Anupam Garg, and W. Zwerger. Dynamics of the dissipative two-state system. *Reviews of Modern Physics*, 59(1):185, 1987.

[13] O. Astafiev, A. M. Zagoskin, A. A. Abdumalikov, Yu. A. Pashkin, T. Yamamoto, K. Inomata, Y. Nakamura, and J. S. Tsai. Resonance fluorescence of a single artificial atom. *Science*, 327(5967):840843, 2010.

[14] Nancy Makri. Real time path integrals with quasi-adiabatic propagators: Quantum dynamics of a system coupled to a harmonic bath. *Nato ASI Series Time-Dependent Quantum Molecular Dynamics*, page 209218, 1992.

[15] B. Peropadre, D. Zueco, D. Porras, and J. J. Garca-Ripoll. Nonequilibrium and non-perturbative dynamics of ultrastrong coupling in open lines. *Physical Review Letters*, 111(24), 2013.

[16] Guillermo Daz-Camacho, Alejandro Bermudez, and Juan Jos Garca-Ripoll. Dynamical polaronansatz: A theoretical tool for the ultrastrong-coupling regime of circuit qed. *Physical Review A*, 93(4), 2016.

[17] C. Sabn, J. J. Garca-Ripoll, E. Solano, and J. Len. Dynamics of entanglement via propagating microwave photons. *Physical Review B*, 81(18), 2010.

[18] M. Stern, G. Catelani, Y. Kubo, C. Grezes, A. Bienfait, D. Vion, D. Esteve, and P. Bertet. Flux qubits with long coherence times for hybrid quantum circuits. *Physical Review Letters*, 113(12), 2014.

[19] J.-L. Orgiazzi, C. Deng, D. Layden, R. Marchildon, F. Kitapli, F. Shen, M. Bal, F. R. Ong, and A. Lupascu. Flux qubits in a planar circuit quantum electrodynamics architecture: Quantum control and decoherence. *Physical Review B*, 93(10), 2016.

[20] B.d. Josephson. Possible new effects in superconductive tunnelling. *Physics Letters*, 1(7):251253, 1962.

[21] P. W. Anderson and J. M. Rowell. Probable observation of the josephson superconducting tunneling effect. *Physical Review Letters*, 10(6):230232, 1963.

[22] J. Bardeen, L. N. Cooper, and J. R. Schrieffer. Microscopic theory of superconductivity. *Physical Review*, 106(1):162164, 1957.

[23] Y. Yu. Coherent temporal oscillations of macroscopic quantum states in a josephson junction. *Science*, 296(5569):889892, 2002.

[24] V. Bouchiat, D. Vion, P. Joyez, D. Esteve, and M. H. Devoret. Quantum coherence with a single cooper pair. *Physica Scripta*, T76(1):165, 1998.

[25] T. P. Orlando, J. E. Mooij, Lin Tian, Caspar H. Van Der Wal, L. S. Levitov, Seth Lloyd, and J. J. Mazo. Superconducting persistent-current qubit. *Physical Review B*, 60(22):1539815413, 1999.

[26] Jens Koch, Terri M. Yu, Jay Gambetta, A. A. Houck, D. I. Schuster, J. Majer, Alexandre Blais, M. H. Devoret, S. M. Girvin, R. J. Schoelkopf, and et al. Charge-insensitive qubit design derived from the cooper pair box. *Physical Review A*, 76(4), 2007.

[27] U. Weiss. *Quantum Dissipative Systems (Series in modern condensed matter physics ; v. 13)*. World Scientific, 2008.

[28] Emma Mckay. Shape cutoff in superconducting qubits,work fluctuations in correlation creation, critical commentary. Master's thesis, University of Waterloo, 2018.

[29] Zinn-Justin J Devoret, M.H. *Quantum fluctuations in electrical circuits*. 1997.

[30] P. Forn-Daz. *Superconducting qubits and quantum resonators*. PhD thesis, Delft University of Technology, 2010.

[31] Alec Maassen Van Den Brink, A J Berkley, and M Yalowsky. Mediated tunable coupling of flux qubits. *New Journal of Physics*, 7:230230, 2005.

[32] Austin G. Fowler, William F. Thompson, Zhizhong Yan, Ashley M. Stephens, B. L. T. Plourde, and Frank K. Wilhelm. Long-range coupling and scalable architecture for superconducting flux qubits. *Physical Review B*, 76(17), 2007.

[33] V. Zakosarenko, N. Bondarenko, S. H. W. Van Der Ploeg, A. Izmalkov, S. Linzen, J. Kunert, M. Grajcar, E. IlIchev, and H.-G. Meyer. Realization of a classical counterpart of a scalable design for adiabatic quantum computation. *Applied Physics Letters*, 90(2):022501, 2007.

[34] A. Lupascu. Lecture 17: Sources of decoherence in superconducting qubits. Lecture notes, Nanoelectronics for Quantum Information Processing QIC880, University of Waterloo, delievered 13 July 2017.

[35] P.V. Klimov, J. Kelly, Z. Chen, M. Neeley, A. Megrant, B. Burkett, R. Barends, K. Arya, B. Chiaro, Yu Chen, and et al. Fluctuations of energy-relaxation times in superconducting qubits. *Physical Review Letters*, 121(9), 2018.

[36] R. Barends, J. Kelly, A. Megrant, D. Sank, E. Jeffrey, Y. Chen, Y. Yin, B. Chiaro, J. Mutus, C. Neill, and et al. Coherent josephson qubit suitable for scalable quantum integrated circuits. *Physical Review Letters*, 111(8), 2013.

[37] Clemens Mller, Jrgen Lisenfeld, Alexander Shnirman, and Stefano Poletto. Interacting two-level defects as sources of fluctuating high-frequency noise in superconducting circuits. *Physical Review B*, 92(3), 2015.

[38] E. L. Hahn. Spin echoes. *Physical Review*, 80(4):580594, 1950.

[39] S. Meiboom and D. Gill. Modified spinecho method for measuring nuclear relaxation times. *Review of Scientific Instruments*, 29(8):688691, 1958.

[40] R. T. Thew, K. Nemoto, A. G. White, and W. J. Munro. Qudit quantum-state tomography. *Physical Review A*, 66(1), 2002.

[41] R. Bianchetti, S. Filipp, M. Baur, J. M. Fink, C. Lang, L. Steffen, M. Boissonneault, A. Blais, and A. Wallraff. Control and tomography of a three level superconducting artificial atom. *Physical Review Letters*, 105(22), 2010.

[42] G. Zizak, J. D. Bradshaw, and J. D. Winefordner. Rate equation solution for the temporal behavior of a three-level system. *Applied Optics*, 19(21):3631, 1980.

[43] Matthew Reagor, Wolfgang Pfaff, Christopher Axline, Reinier W. Heeres, Nissim Ofek, Katrina Sliwa, Eric Holland, Chen Wang, Jacob Blumoff, Kevin Chou, and et al. Quantum memory with millisecond coherence in circuit qed. *Physical Review B*, 94(1), 2016.

[44] Simon Gustavsson, Fei Yan, Gianluigi Catelani, Jonas Bylander, Archana Kamal, Jeffrey Birenbaum, David Hover, Danna Rosenberg, Gabriel Samach, Adam P. Sears, and et al. Suppressing relaxation in superconducting qubits by quasiparticle pumping. *Science*, 354(6319):15731577, 2016.